

Nanocrystal quantum dot electronics and nanofabrication by electron beam ablation

Fischbein, Michael D.

ProQuest Dissertations and Theses; 2009; ProQuest

**NANOCRYSTAL QUANTUM DOT ELECTRONICS AND
NANO FABRICATION BY ELECTRON BEAM ABLATION**

Michael D. Fischbein

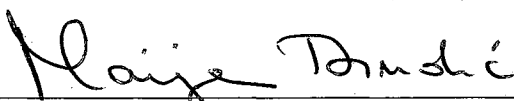
A DISSERTATION

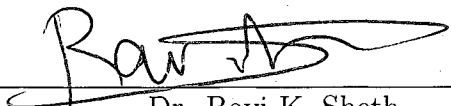
in

Physics and Astronomy

Presented to the Faculties of the University of Pennsylvania in Partial
Fulfillment of the Requirements for the Degree of Doctor of Philosophy

2009


Marija Drndić
Dr. Marija Drndić
Supervisor of Dissertation


Ravi K. Sheth
Dr. Ravi K. Sheth
Graduate Group Chairperson

UMI Number: 3363294

INFORMATION TO USERS

The quality of this reproduction is dependent upon the quality of the copy submitted. Broken or indistinct print, colored or poor quality illustrations and photographs, print bleed-through, substandard margins, and improper alignment can adversely affect reproduction.

In the unlikely event that the author did not send a complete manuscript and there are missing pages, these will be noted. Also, if unauthorized copyright material had to be removed, a note will indicate the deletion.



UMI Microform 3363294
Copyright 2009 by ProQuest LLC
All rights reserved. This microform edition is protected against
unauthorized copying under Title 17, United States Code.

ProQuest LLC
789 East Eisenhower Parkway
P.O. Box 1346
Ann Arbor, MI 48106-1346

Acknowledgements

There are many people who have contributed to making my graduate school experience a rich and exciting process of learning about physics and beyond. I could not have come this far without the continuing support and guidance that I received from my advisor, Dr. Marija Drndić. She has always made it a point to stay interactive with the lab research and the discussions in the Condensed Matter Physics community at large, no matter how many demanding activities she was already pursuing. From her I have learned a great deal about the nature of science and scientists.

Though the lab group remained relatively small until recently, I had the pleasure of working with several talented people in good ‘ol room 1N19. In particular it has been fun to share the grad life and talk shop with my fellow Ph.D.’s to be: Siying Wang, Lauren Willis, Jessamyn Fairfield, and the recently arrived Matt Puster. I have learned a lot from several postdocs who decided to pass through DRL on their way to greatness. First, I’ve been waiting to formally thank Scott Paulson (now Professor Paulson) for several years now, because he is the one who taught me how to make SiN_x membranes and, moreover, through some mini adventures with him and some other Johnson group members at an APS meeting in Montréal, he helped me to see that an easy-going and fun-loving attitude is not mutually exclusive with having a passion for physics and a thirst to work hard. Dr. Claudia Querner taught me most of what I know about how to make nanocrystals before leaving to pursue her industrial career in Germany (and there is probably no better person to go for lunch with when labwork gets stressful and a break is badly needed). Dr. Ken Healy

has inspired me to believe that a computer can be used to do just about anything, that is, as long as Ken is the one doing the programming. I am greatly indebted to him for teaching me many great tricks with computers and electronics. Though Dr. Tali Dadosh has only been here a few months, I have really enjoyed discussing research projects as well as recipes for stews and cookies (who knew Israeli flour is different than American flour?) and I am looking forward to continuing pursuing some of our research ideas in the near future.

I am also grateful to the Professors Charlie Johnson, Gene Melé, Jay Kikkawa, Charlie Kane for always being willing to make time to enthusiastically engage in whatever topic I brought to their offices.

And to those students in my year who managed to get out before me, it sure was fun talking physics and drinking the occasional late-night beer at Intermezzo and White Dog. I speak of course of Dr. Dan Milkie, Dr. Brian Edwards, Dr. Danvers Johnston, and Dr. Dutch Ratliff. Dr. Sam Khamis gets his own dedicated sentence: this place wouldn't have been the same without you (I think no one could argue with that!).

Naturally, I owe my parents a huge debt of gratitude for supporting me at every stage of this process and onward to the future. I am of course proud that soon I will officially be a Ph.D. in Physics (and Astronomy??), but it gives me great pleasure to know that you are there to share in the joy of this achievement. This thesis is dedicated to the two of you.

If I forgot to acknowledge someone, or if there is something here that I would have been better off for forgetting to mention, please, oh reader, forgive me, for I have not slept in 30 hours.

Lastly, I'd like to acknowledge Benjamin Franklin, because without him, there wouldn't be any Penn to speak of (and there would be a huge deficit in names for buildings and places in Philadelphia). I will always treasure the time I spent pursuing Physics research at Penn.

ABSTRACT

NANOCRYSTAL QUANTUM DOT ELECTRONICS AND NANOFABRICATION BY ELECTRON BEAM ABLATION

Michael D. Fischbein

Dr. Marija Drndić

Nanocrystal quantum dots are nanometer-scale structures with size-dependent electronic and optical properties that make them interesting for novel technological applications and for fundamental physics research. In this thesis, electronic properties of several types of semi-conductor nanocrystals are studied by integrating arrays of them into electrode-gap devices and measuring their conductivities with current-voltage characterization and charge-imaging. Additionally, novel nano-fabrication techniques were developed to assist in the studies of nanocrystals and nanostructures in general. Central to all of this work has been the compatibility of electronic measurements and high-resolution imaging. This has allowed for greater insight into the nature of electron motion in nanocrystal arrays and also has been the enabling factor for realizing the nano-fabrication techniques.

Contents

Acknowledgements	ii
1 Introduction	1
1.1 Nanocrystals	1
1.1.1 Single Nanocrystals	1
1.1.2 Nanocrystal Arrays	5
1.2 Overview of Nanocrystal Transport	6
1.3 Transport models for NC arrays	7
1.3.1 Dark-current	7
1.3.2 Photo-current	11
1.4 Motivation for the present work and overview of results	13
2 Device Design, Function, and Fabrication	19
2.1 Design and Function	19
2.2 Fabrication	21
3 Measurement Setup	25
4 Sample Preparation	29
5 Nanocrystal Transport Measurement and Correlated Imaging by Transmission Electron Microscopy	32
5.1 Introduction	32

5.2	CdSe NCs	33
5.3	CdSe + Au NC mixtures	39
5.3.1	35:1 (CdSe:Au) Number Ratio	40
5.3.2	3:2 (CdSe:Au) Number Ratio	45
5.4	CdSe NRs	50
5.5	PbSe NCs	58
6	Local Charge Transport in PbSe Nanocrystal Assemblies Studied by Correlated Electrostatic Force Microscopy and Transmission Electron Microscopy	67
6.1	Introduction	67
6.2	Electrostatic Force Microscopy: Theoretical Description	68
6.3	Experimental Details	72
6.4	Background measurements	74
6.5	Results	74
6.6	Annealed 6.8 nm diameter PbSe superlattice networks	83
6.7	Voltage Dependence	83
6.8	Conclusion	92
7	Electronic Memory Effects in Large Assemblies of CdSe Nanocrystals	95
7.1	Introduction	95
7.2	Results and Discussion	97
8	Nanogaps by direct lithography for high-resolution imaging and electronic characterization of nanostructures	106
8.1	Introduction	106
8.2	Results and Discussion	108

9 Sub-10nm device fabrication using a transmission electron microscope	113
9.1 Introduction	113
9.2 Example Nanostructures	114
9.3 Methods	115
9.3.1 Preparation	115
9.3.2 Nanosculpting	118
9.4 More Examples	119
9.5 Effect on Lattice Structure	121
9.6 Crystallization of Au	122
9.7 Precision of the Technique	126
9.8 Device Measurement	126
9.9 Potential Application in Superconductivity Research	128
9.10 Application to DNA analysis	133
9.11 Automation	136
9.12 Conclusions	136
10 Electron beam nanosculpting of suspended graphene sheets	138
10.1 Introduction	138
10.2 Methods	139
10.3 Results and Discussion	140
10.4 Conclusion	146
11 Conclusions	147

List of Figures

1.1	TEM images of nanoparticles	2
2.1	Schematics and electron micrographs of a measurement device	20
2.2	SiN _x suspended membrane fabrication	22
3.1	Measurement Cryostat	26
5.1	CdSe I-V characteristics	34
5.2	TEM images of a CdSe NC electrode gap	35
5.3	Dark and photo I-V's for CdSe at 78 K	37
5.4	Photo I-V's for CdSe from 90 to 200 K	38
5.5	Dark and photo I-V's for the 35:1 CdSe to Au NC mixture at 295 K .	41
5.6	Dark and photo I-V's for the 35:1 CdSe to Au NC mixture at 78 K .	42
5.7	Temperature dependence of photo I-V's for the 35:1 CdSe to Au NC mixture .	44
5.8	Dark and photo I-V's for the 3:2 CdSe to Au NC mixture at 295 K .	46
5.9	Comparison of photo I-V's for the 3:2 CdSe to Au NC mixture at 78 and 295 K	47
5.10	Comparison of dark and photo I-Vs from the CdSe + Au NC mixtures with CdSe-only	48
5.11	TEM image of CdSe NRs in an electrode gap	51
5.12	Dark I-V and transient behavior of CdSe NRs at 295 K	52
5.13	TEM image of CdSe NRs in an electrode gap	54

5.14	Dark I-V temperature dependence of CdSe NRs	55
5.15	Photo I-V temperature dependence of CdSe NRs	57
5.16	TEM images of PbSe NCs in and electrode gap	59
5.17	TEM images of PbSe NCs assembled into superlattices inside different electrode gaps.	61
5.18	TEM images of PbSe NCs treated with butane-dithiol and their assembled in an electrode gap.	63
5.19	TEM images of several PbSe NCs measured in a nanogap and corresponding I-V data.	64
6.1	Schematic of charge imaging (EFM)	70
6.2	TEM images of nanoparticles	73
6.3	Background EFM signals	75
6.4	EFM images of 3.5 nm PbSe NCs	77
6.5	EFM images of an annealed 3.5 nm PbSe NC film	78
6.6	Correlation of EFM and TEM images	81
6.7	EFM images of an annealed PbSe NC film at various magnifications .	82
6.8	EFM and Height images of a charged PbSe NC superlattice network .	84
6.9	TEM images of PbSe NC superlattice network structure	85
6.10	Example of correlated EFM signal with network structure	86
6.11	EFM images showing network charging as a function of electrode voltage	88
6.12	Comparison: tip versus electrode voltage	89
6.13	TEM/EFM correlation showing significant charging differences between single and few NC layers	91
6.14	TEM images showing reduced spacing between annealed 6.8 nm diameter PbSe NCs	93
7.1	Dark and photo I-V characterization of a CdSe NC memory device .	98
7.2	CdSe NC memory cycle measurement	99

7.3	Electrical versus optical erasing	101
7.4	Tuning the CdSe NC array conductivity with laser erasing	104
8.1	Examples of nanogaps	109
8.2	Reduction of EBL proximity effect	111
9.1	Example structures made by electron beam ablation	116
9.2	Apparatus for nanosculpting	117
9.3	Nanostructure example gallery	120
9.4	Ablating atomic planes from Ag	123
9.5	Crystallization of amorphous Au into a faceted nanocrystal	124
9.6	Formation of a nanogap with crystalline contacts	125
9.7	Precision nanosculpting of Ag	127
9.8	Nanowire and nanogap device characterization	129
9.9	Making a 4-terminal nanogap field effect transistor	131
9.10	8-terminal device fabricated from Ni/Cr	132
9.11	Devices for molecular detection and analysis	134
9.12	Nanopore-nanogap device fabrication	135
10.1	Spot ablation of a suspended graphene sheet	141
10.2	Formation of a nanobridge	144
10.3	Zig-zag line nanosculpted in a graphene sheet	145

Chapter 1

Introduction

1.1 Nanocrystals

1.1.1 Single Nanocrystals

Nanocrystals (NCs), also called “artificial atoms” or “colloidal quantum dots”, are nanometer-scale crystalline volumes (c.f., Figure 1.1). Typical NCs consist of only ~ 100 ’s to 1000 ’s of atoms, giving them unusually high surface area to volume ratio. As a consequence of their extremely small size, they can exhibit rich physical properties that differ significantly from that of their bulk counterparts.^[1-4] As an example, NCs made of II-VI semiconductor material (e.g., CdSe, CdTe, CdS, ZnS) emit visible light with wavelength dependent on the NC size.^[2,5,6] This behavior is a direct effect of excitonic quantum confinement and is readily observed at room temperature.^[7-9]

Modern synthetic chemistry techniques make it possible to vary the size of a NC with atomic-layer precision, thereby allowing for impressive control over their size-dependent properties.^[5,10] Such property control makes NCs promising building blocks for functional materials and integrated devices. In fact, NC arrays have

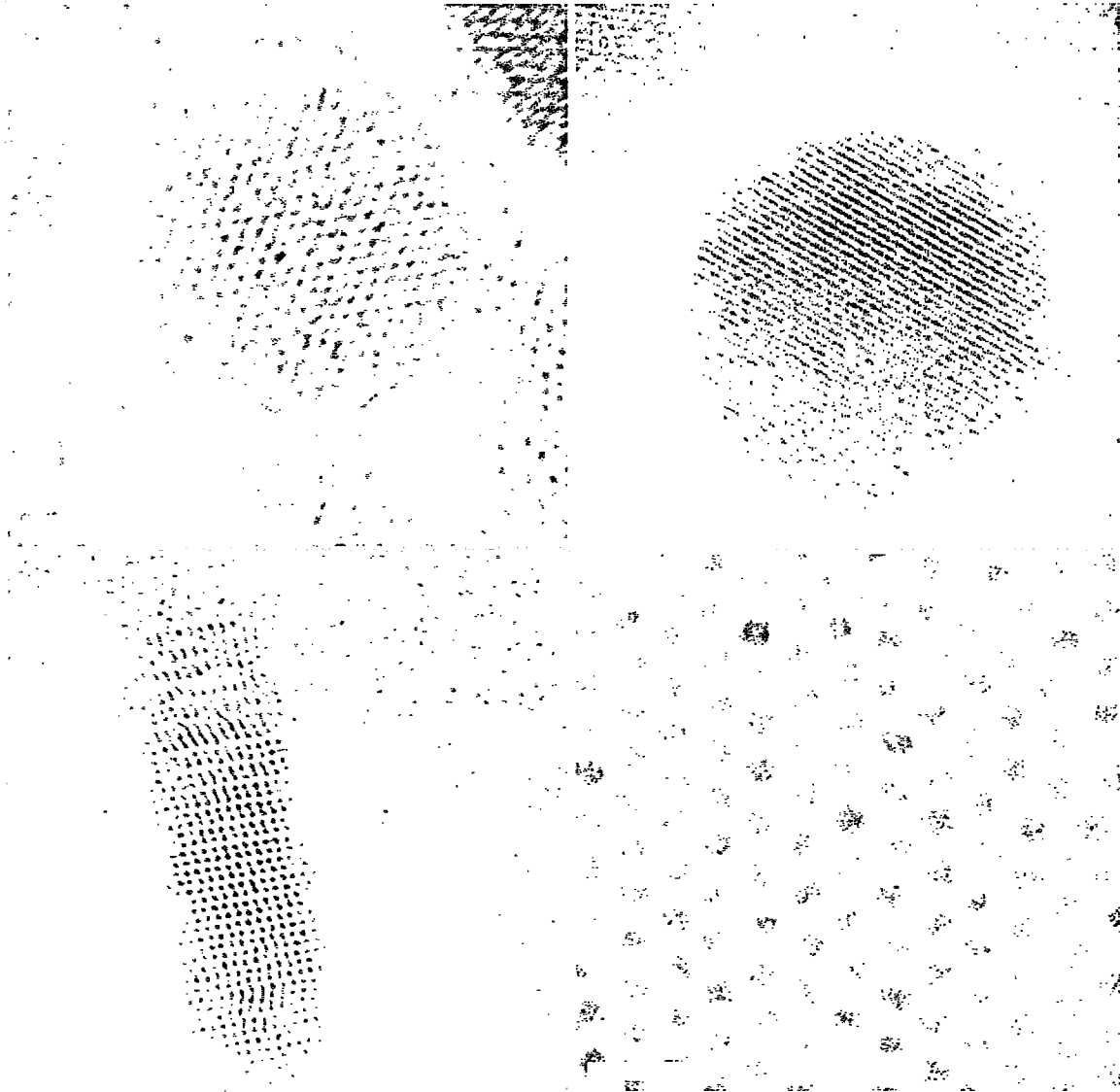


Figure 1.1: (a) High-resolution TEM image of a spherical PbSe NC. The atomic crystal structure can be seen as the fine lattice structure. PbSe NCs are capped with a mono-layer of organic ligand, oleic acid, roughly 2 nm thick, that is invisible to TEM imaging. (b) High-resolution TEM image of a faceted Au NC. This NC was prepared by evaporating a thin film of Au. It therefore does not have any ligand cap. (c) High-resolution TEM image of a rod-like CdSe NC. As with all CdSe NCs, it is capped with a mono-layer of organic ligand, trioctylphosphine oxide (TOPO), roughly 1nm thick, that is invisible to TEM imaging (d) Lower magnification TEM image showing PbSe NCs assembled in a 2-D triangular array, separated by the oleic acid ligands. Scale bars are 2, 2, 5, 20 nm.

emerged as a new class of materials with a variety of potential applications including light-emitting devices,^[11,12] tunnel diodes,^[13] photovoltaic cells,^[14,15] thermoelectrics,^[16] photo-detectors,^[17] biosensors,^[18,19] information storage,^[20] and quantum information processing.^[21,22]

In a simple picture, a NC is thought of as a quantum well in which a charge carrier (electron or hole) behaves like a *particle-in-a-box* with an effective mass, m_c .^[8,23–25] In general, m_c is material dependent and is used to describe conduction-band carriers (electrons) or valence-band carriers (holes). Given the approximately spherical shape of NCs, carriers inside a NC are confined by a radial boundary condition, [$V = 0$ ($r < R$), $V = \infty$ ($r \geq R$)]. The carriers are therefore characterized by *particle-in-a-sphere* wavefunctions:

$$\Psi_{n,l,m}(r, \theta, \phi) = C \frac{j_l(k_{n,l}r)Y_l^m(\theta, \phi)}{r} \quad (1.1)$$

where C is a normalization constant, $Y_l^m(\theta, \phi)$ is a spherical harmonic, $j_l(k_{n,l}r)$ is the l th-order spherical Bessel function. The boundary condition at $r = R$ translates to $j_l(k_{n,l}R) = 0$, so that $k_{n,l}R = \lambda_{n,l}$ where $\lambda_{n,l}$ is the n th zero of j_l . The corresponding energies directly reveal the strong influence of NC size:

$$E_{n,l} = \frac{\hbar^2 k_{n,l}^2}{2m_c} = \frac{\hbar^2 \lambda_{n,l}^2}{2m_c R^2} \quad (1.2)$$

As is evident in Eq.(1.1) the approximate spherical symmetry of a NC gives rise to atomic orbital-like wavefunctions. An interesting distinction from actual atoms, however, is that due to the boundary condition, both the orbitals and the energy spectrum of these “artificial atoms” can be tuned without needing to change the material (i.e., without needing to change m_c).

It is important to note that there are two significantly different mechanisms by which carriers are created in a neutral NC: i)a photon is absorbed by the NC and excites an electron into the conduction-band (and therefore creates a hole in the valence-band), in which case the NC is left neutral, ii)an electron or hole is directly injected into the NC, in which case the NC is left charged.

For the first case, the energy cost of generating an electron-hole pair is the bulk band-gap energy plus the confinement energies for each carrier. In bulk materials, the pair will typically relax into an excitonic bound state due to the Coulomb interaction, which reduces the total energy cost. The total cost of photo-generating an electron-hole pair is therefore:

$$E_{n_e, l_e, n_h, l_h} = E_{gap} + \frac{\hbar^2}{2R^2} \left(\frac{\lambda_{n_e, l_e}^2}{m_e} + \frac{\lambda_{n_h, l_h}^2}{m_h} \right) - \frac{1.8e^2}{\epsilon R} \quad (1.3)$$

where ϵ is the material dielectric constant. In this expression, the Coulomb term is NC size-dependent, which is based on the assumption that the NC is smaller than the volume occupied by an exciton in the bulk material.^[26,27] This characteristic excitonic length scale is called the “Bohr-radius”, a_B , and it gives the approximate distance between the electron and hole. a_B is defined for bulk materials as

$$a_B = \epsilon \frac{m}{m_c} a_0, \quad (1.4)$$

where m is the electron rest, m_c is taken to be the reduced exciton mass, and a_0 is the Bohr radius of hydrogen. Comparison of a_B with the size of the NC determines the “strength” of quantum confinement. For CdSe $a_B \sim 6$ nm and the emission spectra indeed begin to blue-shift once the NC diameter is reduced below 6 nm.^[5,6] The effect of confinement in the IV-VI class of NCs (e.g., PbSe, PbTe, PbS) is even more dramatic because a_B can be 10’s of nanometers, many times larger than typical NC diameters.^[28-31]

In the case of direct injection of carriers a_B is not a meaningful quantity (unless electrons and holes are being injected together) and the thermal de Broglie wavelength, $\Lambda = \sqrt{\frac{\hbar^2}{m_c k_B T}}$, should be used for comparison with the NC size. The energy of adding a single carrier consists of the confinement energy (Eq.(1.1)) plus an additional term due to the classical electrostatic self-capacitance, $C_{sphere} = 4\pi\epsilon R$, of the NC:

$$E_{n, l} = \frac{\hbar^2 \lambda_{n, l}^2}{2m_c R^2} + \frac{e^2}{4\pi\epsilon R} \quad (1.5)$$

From the different dependence on NC size, there will always be a unique value for R where the two contributions are equal, and below which the confinement energy will dominate. For CdSe NCs, with $\epsilon \sim 8\epsilon_0$,^[32] this crossing point occurs for NC diameters ~ 10 nm. For a 4.5 nm diameter CdSe NC the charging energy is ~ 150 meV while the ground state confinement energy is ~ 300 meV. Importantly, these values are well above the thermal energy at room temperature (~ 26 meV). PbSe NCs have a significantly higher dielectric constant (~ 250)^[28,33] and therefore have a much lower contribution from classical charging. Additional energy considerations are required in systems of coupled NCs and this will be discussed in the next section.

1.1.2 Nanocrystal Arrays

NCs readily self-assemble into ordered arrays when they are drop-cast from solution which is then allowed to dry.^[34–36] An example of PbSe NCs assembled in a 2-dimensional triangular array is shown in Figure 1.1(d). Like individual NCs, arrays of NCs, also called “artificial solids”, also exhibit rich physics.^[34] For instance, a reversible metal-insulator transition was observed in arrays of Ag NCs by tuning the inter-NC coupling.^[37–39] NC arrays are particularly interesting for probing charge correlation effects. Specifically, electrons in arrays of semiconductor NCs are expected to experience long-range Coulomb interactions due to reduced screening compared to metallic NCs,^[40] allowing the possibility of observing effects of highly correlated motion. The size and shape of NCs can be well controlled by varying chemical synthesis parameters and therefore the physical properties of NCs can be tuned. The ability to tune both the electronic energy level structure of individual NCs (by adjusting their size) as well as the electronic coupling between NCs in arrays (by adjusting the molecular barriers between them) makes NC arrays a promising model system for investigating many-body physics.^[34] Current research on the opto-electric behavior of NC arrays is particularly important because of the

potential realization of a new generation of efficient solar cells.^[41–43] Moreover, solution processing allows for large-scale production of NCs and makes them compatible with curved and flexible surface applications, in contrast to standard Si wafer based technology.

1.2 Overview of Nanocrystal Transport

Over the past decade, impressive developments in synthetic chemistry have yielded techniques for producing NC with well-controlled particle size and shape have made the systematic study of their properties possible.^[2,5] Many studies have focused on understanding their optical properties, at the level of individual NCs and NC ensembles.^[3,44,45]

Electrical transport measurements offer another approach for probing the basic charge dynamics in these systems. Electronic properties of individual semiconducting NCs have been revealed in scanning tunneling microscopy (STM) measurements^[46–48] and results agreed well with theories based on quantum confinement. Progress has been made toward identifying the electronic properties of arrays of metallic and semiconducting NCs. However, obtaining unambiguous data has been made difficult by their generally resistive nature, particularly for semiconducting NCs. In particular, traditional characterization using a field-effect-transistor (FET) device geometry, where NC arrays constitute the channel region between source and drain electrodes, have not yielded significant signals. In fact, for channel lengths as small as $1\text{ }\mu\text{m}$ it has not been possible to detect clear current signals for applied fields up to 10^8 V/m , corresponding to $\sim 500\text{ mV}$ across each NC.^[49,50] Current-voltage (I - V) characterization of arrays of 3.4 nm diameter CdSe NCs using a layered device structure, where the NCs were sandwiched between two large ($\sim 3\text{ mm}^2$) Au planes, did yield measurable current. However, the measured values corresponded to a resistivity of $\sim 10^{11}\text{ }\Omega\cdot\text{m}$, roughly nine orders of magnitude more resistive than undoped silicon;

comparable to glass.

Methods for increasing conductivity in arrays of semiconducting NCs have actively been pursued and early techniques such as electrochemical doping were effective.^[51-55] Annealing was also shown to improve the conductivity of CdSe NC arrays,^[50] Co arrays^[56] and PbSe arrays^[57] by reducing the inter-NC separation, which narrows tunneling barriers and increases exchange coupling.^[58] For arrays of II-VI semiconductor NCs, charge ionization by photo-excitation has been demonstrated as a valuable method of increasing the number of carriers available for transport.^[59] More recently, it was shown that post-synthesis chemical treatments of NC films can dramatically increase the dark-current in PbSe NCs^[60] photo-conductivity in CdSe^[61] and CdTe^[62] NC arrays.⁴⁴ The effect is largely attributed to reducing the spacing between the NCs, but the new ligands introduced by the treatment actively contribute to the transport via hole doping in the PbSe case.^[60] Annealing CdSe NCs coated with a protective layer of ZnS, so called “core-shell” NCs, was effective at increasing photo-ionization efficiency and substantially improved array photo-conductivity.^[62,63]

Though NC array conductivity was often increased significantly with these treatments, a variety of specific behaviors have been observed. Models of the transport mechanisms responsible for conduction in NC arrays have evolved significantly, but a complete picture is still unavailable. Several important models for DC transport in NC arrays with and without photo-excitation are briefly summarized in the following section.

1.3 Transport models for NC arrays

1.3.1 Dark-current

Treating a NC film between two electrodes as a close packed array of conducting islands separated from their nearest neighbors by a tunneling barrier through which

electrons localized on the NCs can tunnel with resistance R leads to a power law prediction for current dependence on voltage. Specifically, for an array of width W ,

$$I \sim W \left(\frac{V_0}{R} \right) \left[\frac{V}{V_T} - 1 \right]^\lambda \quad (1.6)$$

where below a threshold voltage, V_T , current is suppressed by the Coulomb energy to add or remove an electron from an initially neutral island. This energy is $eV_0 = e^2/C_0$, where C_0 is the self-capacitance of an island. Modeling an NC as a sphere gives $C_0 = 4\pi\epsilon R$, where R is the radius and ϵ is the dielectric constant of its environment (usually taken to be the dielectric of the ligand). For a 2-dimensional (2-D) $M \times N$ array of NCs (N being the number of NCs in a row between the electrodes), the threshold V_T scales linearly with array length as

$$V_T = \frac{\alpha Ne}{C_0} \quad (1.7)$$

where alpha depends primarily on the ratio of inter-NC capacitance to self-capacitance (C_{nn}/C_0), decreasing from an estimated value of 0.338 (corresponding to $C_{nn}/C_0 \rightarrow 0$) as inter-NC coupling increases ($C_{nn}/C_0 > 0$).^[64] Above V_T , 1-D current paths begin to form in the film, leading to measurable current. These so-called “percolation paths” are separated from each other with average spacing $\xi \sim \left(\frac{V}{V_T} - 1 \right)^{-2/3}$ and increase in number with increasing voltage.^[64] Correspondingly, the current scales with power-law dependence on voltage (Eq.(1.6)) where the exponent is predicted to be $\lambda = 1$ for a 1-D array and $\lambda = 5/3$ in 2-D. These prediction were obtained analytically for an infinite array. Simulations of finite arrays have yielded $\lambda = 2$ in 2-D, while scaling of current in a 1-D channel is always linear. Power-law scaling behavior with a voltage threshold was observed for well ordered 2-D arrays of Au NCs coupled via dodecanethiol linker molecules, where exponents resulting from the measurements were between 1.6 - 2.1.^[65,66] No prediction for λ exists for the 3-D case, but experiments have also revealed power-law scaling behavior and a voltage threshold, with λ ranging from 2 to 3.5.^[56,67]

This model assumed zero-temperature conditions. Although the predictions

matched experiments well, temperature is of course never zero. Incorporating local energy fluctuations that are expected at finite temperature, which act to effectively reduce local tunneling barriers has been shown to reduce V_T . Furthermore, this model naturally allows one to include the spread in local island energies that occur due to finite NC diameter dispersion and array disorder.^[68] Specifically, the reduced threshold voltage is estimated to behave as:

$$V_T(T) = V_T(0) \left(1 - \frac{P(T)}{P(T^*)} \right), \quad (1.8)$$

where $V_T(0)$ is the zero-temperature value and $P(T) \sim 2\beta k_B T / \alpha$ is the fraction of NC-NC junctions that are effectively Ohmic due to the corresponding barrier energy being comparable to $k_B T$; T^* is the effective temperature at which enough Ohmic barriers exist to form one complete Ohmic path between the electrodes; β is a measure of the extent of thermal broadening of energy levels in individual NCs and is independent of the topology, dimensionality and inter-NC coupling of the NC array; α is an effective charging energy incorporating disorder. This model was shown to characterize the shift in V_T as a function of temperature in the 2-D dodecanethiol-linked Au NC array systems mentioned above.

Conduction above V_T is sensitive to temperature, as charge carriers are thermally activated over potential barriers and the population of energy levels above the Fermi energy in individual NCs increases. Conductivity in Au NC arrays has been observed to scale exponentially with inverse temperature^[69,70] i.e.,

$$\ln(G) \sim T^{-1} \quad (1.9)$$

This behavior has been accounted for by modeling thermal population of states in individual islands using Fermi-Dirac statistics.^[71]

Arrays of semiconducting NCs that have been either chemically treated or annealed to achieve measurable currents have been shown to have conductivities that deviate from the trends observed for metallic NC arrays. This may not seem all that surprising, considering that semiconductors and metals already have very different

behavior in the bulk. However, NC array conduction is based on electrons moving across significant barriers between localized regions (the NCs) and motion within individual NCs does not directly contribute to the measured current. That arrays of metallic NCs are themselves not metallic is evident from their temperature dependence (Eq.(1.9)). Temperature dependence differing from the activated behavior observed for metallic NCs by significantly increasing the inter-NC coupling.^[37,39]

An important model that predicts deviations from thermally activated behavior but still retains general exponential dependence on inverse temperature is the variable range hopping model proposed by Mott to describe transport in disordered materials. The model is based on the idea that at low temperature, charges hopping between localized sites will more often hop to a distant site instead of a nearest neighbor site in pursuit of occupying a lower energy state because of the irregular potential landscape that exists in disordered materials.^[72] Thermal contributions to the transport dynamics disrupt the wave function coherence required for long range hopping and the competition between the two contributions is captured in the probability for hopping a distance D :

$$P \sim \exp \left[-\left(\frac{2D}{L} + \frac{E_a}{k_B T} \right) \right], \quad (1.10)$$

where L is the localization length (e.g., NC diameter in the case of NC arrays) and E_a is the characteristic energy for contributions from activated hopping. The optimum hopping distance for a given system is found by choosing an appropriate dependence of E_a on the hopping distance and maximizing this expression. The model predicts the conductivity to behave as

$$\ln(G) \sim T^{-\nu}, \quad (1.11)$$

where $\nu = 1/3$ for 2-D systems and $\nu = 1/4$ in 3-D. The signature of VRH is therefore found by extracting the scaling exponent from temperature dependence measurements of conductivity.

Efros and Shklovskii pointed out that accounting for Coulomb interactions between mobile carriers introduces a gap in the density of states for the temperature

regime where $k_B T \ll e^2/4\pi\epsilon r$ and that this changes the scaling exponent in both the 2-D and 3-D cases to $\nu = 1/2$. VRH in the presence of a Coulomb gap is called Efros-Shklovskii VRH (ES-VRH).

The VRH picture has been used to explain the behavior of strongly coupled Ag NCs^[73] in 2-D and ES-VRH has been observed for quasi-2-D annealed Co NCs.^[56] 3-D CdSe^[53-55] and PbSe^[52]NC arrays that were electrochemically doped were also modeled with the ES-VRH picture, which estimated hopping distances of more than 6 NC diameters at 4.3 K.⁵⁶ However, PbSe NCs treated with hydrazine to achieve very small inter-NC separation displayed VRH, but without a Coulomb gap.^[60] Moreover, recently reported measurements on annealed PbSe NC arrays revealed no clear evidence of VRH and the transport behavior was readily modeled with a simple picture of thermally activated hopping between nearest neighbor NCs.^[57] Further investigation into the nature of PbSe NC arrays is necessary for these differing pictures to converge.

1.3.2 Photo-current

In addition to being an effective way to increasing the conductivity in NC arrays, photo-excitation is a valuable probe of carrier dynamics and general charge structure in NC arrays. Interpreting photo-conductivity results can be complicated by contributions from dark-current and electrode contacts in devices designed for measuring photo-conductivities fall into two major classes. The first kind of electrode contact is called “blocking”, where no dark-current is measurable and all measured current is due to carriers generated in the NC array - called “primary photo-current”. The second kind of contact is called “non-blocking”, where charge can be injected into the NC array when a voltage bias is applied. This corresponds to dark-current contributing to the photo-current signal, which in this case is labeled “secondary photo-current”. Models of photo-conductivity in NC arrays have assumed blocking

contacts and therefore that the physics of photo-excited carriers can be treated independently from dark-current models. For untreated CdSe NC arrays, this is a valid approximation, since dark current was difficult to detect anyway. The carrier dynamics involved in photo-activated devices are generally thought to be governed by the efficiency of photon to exciton conversion, ionization of the excitons, and competition between electron and hole mobilities and their rates of non-radiative recombination. *I-V* characteristics for CdSe NCs measured under bad-gap illumination conditions in micron-scale electrode gaps are non-linear, indicating that photo-conductivity is field dependent. The approximate energy cost for separating photo-excited carriers is the difference between the exciton binding energy in an individual NC and the Coulomb interaction between separated carriers in two neighboring NCs. Experimental studies have demonstrated that the primary role of the field is to lower this energy barrier. Comparison with a model based on tunneling of field-ionized carriers through the ligand barriers qualitatively explains the non-linearity. This model has also had success in qualitatively explaining the photo-activated currents observed in disordered arrays of non-spherical, rod-like CdSe NCs (called “nanorods”).^[74] However, quantitative analysis using this model results in physical parameters that contradict known values, such as the barrier transparency. Detailed calculations that more realistically reflect charge and quantum interactions at the NC-NC interface are needed for a more thorough understanding of the dynamics.^[59]

Efforts to increase the photo-conductivity have focused on chemical treatments, namely ligand exchange from TOPO molecules to shorter ligands with better surface trap passivation properties.^[61–63] Increasing the inter-NC coupling and reducing the presence of surface traps states improved the photo-conductivity of NC arrays by orders of magnitude, to the point where previously unattainable limiting cases were observed, such as photo-current saturation.^[61] This enabled additional theoretical understanding and further demonstrated the potential for NC-based opto-electronic

applications. Importantly, the ligand-exchange process left the contacts still blocking because the large work-function offset between the Au electrodes and the NC array was not effected. The physical insights into primary photo-conductivity in NC arrays that were established for untreated CdSe NC arrays, such as the increase of ionization efficiency from applied fields, could therefore be applied.

A consequence of blocking contacts is that charge develops in the regions close to the electrodes because only one of the two carriers created by exciton ionization leaves the film and this charge cannot be compensated by injection from the electrode. This effect causes a significant portion of the applied bias to drop in the proximity of the electrodes. Extending a model developed for bulk photo-conductors with blocking contacts^[75] to include the effect of field-assisted exciton ionization observed in the earlier CdSe NC studies allowed the behavior of ligand-exchanged CdSe NC arrays to be captured relatively well.^[61] In particular, this model matched the low-bias linear response, square-root dependence for intermediate voltages, and saturation at high bias. Saturation of the photo-current indicated that it was possible to extract all photo-generated carriers, a measure of the significant improvements achieved with ligand exchange techniques.

1.4 Motivation for the present work and overview of results

The results described in the above review were obtained by introducing NC samples into the gap between source and drain electrodes and measuring the amount of current that flowed through the array as a function of applied voltage bias. In these measurements, it was typical to assume that the NCs were, overall, assembled into very well ordered arrays in the electrode gaps. The substrates used for these devices were thick (~ 100 nm SiO₂ on ~ 0.5 mm thick Si) and therefore not compatible with transmission electron microscopy (TEM), which is the primary imaging technique used to characterize nanostructures. It was therefore not possible to determine the

degree of NC ordering in the arrays that were measured. Alternative imaging methods that are compatible with thick substrates, such as scanning electron microscopy (SEM) and atomic force microscopy (AFM) do not have sufficient resolution for identifying detailed NC array structure. Scanning tunneling microscopy (STM) achieves atomic resolution, but requires samples to sit on a conductive surface, which is not compatible with transport measurement by electrode gap devices. As a consequence, in addition to the uncertainty regarding the assembly order in un-treated NC films, the validity of assuming that treated films were also well ordered could not be verified in these studies. Moreover, important factors like array contact to the measurement electrodes and gap integrity (e.g., absence/presence of unwanted debris) were difficult to assess without compatible high-resolution imaging. By using extremely thin (~ 100 nm) devices substrates, Jaeger *et al.* demonstrated that TEM can be made compatible with *I-V* characterization of NC arrays.^[65] Applying this technique to Au NC arrays resulted in direct demonstrations of the influence of order on transport behavior.^[65,76]

The studies on semiconductor NCs conducted for this thesis applied the techniques for making measurement devices compatible with TEM imaging. Using this approach, the actual NC arrangement inside measurement electrode gaps were identified with high resolution by TEM, in contrast to *all* previous measurements made on semiconductor NCs. This information was used to gain valuable insight into the results of measurements of NC array electronic properties, studied using *I-V* characterization and charge imaging. In general, semiconducting NCs were focused on for this thesis, as opposed to metallic NCs, because their quantized energy level separation is much larger and screening is reduced. Furthermore, semiconducting NCs have more potential for opto-electronic device applications because of their tunable band gaps.

In most previous cases, the devices used for measurement had electrodes with dimensions and separation orders of magnitude larger than the size of individual NCs.

This was intended to allow array irregularities, such as local disorder in an otherwise ordered NC assembly, to be averaged out. The electrode dimensions used in most of the measurements discussed in this thesis were between one and two orders of magnitude smaller than in previous studies, making the scale on which the sample were probed significantly closer to intrinsic length scales such as charge carrier diffusion lengths.

Measurements on single semiconductor NCs in devices by so-called “nanogaps”, where the source and drain electrodes were separated by only several nanometers, have been reported^[77] but such results have never been unequivocally verified as accurate representations of NC properties. In fact, results from nanogap measurements are notoriously difficult to verify and system artifacts can easily be mistaken for meaningful sample properties.^[78,79] The potential for insight into nanostructures using nanogaps is significant, though it is necessary to distinguish spurious results from actual sample properties. This is very difficult without the ability to inspect the nanogap contents. Techniques for fabricating nanogaps that are compatible with TEM imaging are therefore highly valuable. In the process of pursuing NC transport research I developed two techniques for making nanogaps that are compatible with TEM imaging. One of the techniques is particularly versatile and many other interesting structures and device components that are TEM compatible can be made that were previously impossible to achieve. Although the generality of this technique goes beyond applications to NC research, it is discussed at length toward the end of the thesis because of its value to nanoscience and nanotechnology research in general.

Although treatments of NC arrays intended to improve their conductivity have been fruitful, it would be preferable if such treatments were not necessary because of the possibility of altering the structure of the as-synthesized NCs or obscuring the interpretation of results due to the treatments adding electronically active substances to the sample arrays. For this reason, none of the samples that were used to study transport in 100 nm-scale electrode gaps were subjected to any current-enhancing

treatments. The only cases of treated samples were mild (150 C) annealing of PbSe NC arrays for a charge imaging based study and moderate annealing (300 C) of CdSe NCs in micron-scale gaps for electronic memory measurements.

Chapter 5 summarizes the results of conductivity measurements of several types of NC arrays studied with \sim 100 nm electrode gap devices. Temperature dependence of current-voltage (*I-V*) behavior under dark and photo-excited conditions are described. Device detail, such as NC assembly structure in the electrode gaps, was imaged by transmission electron microscopy (TEM) and the results were used together with the *I-V* behavior to gain unique insight into their electronic properties. CdSe NC were highly resistive in the dark, but yielded significant currents under photo-excitation at low temperature. Mixing a small fraction of Au NCs into the CdSe NC arrays only had a small effect on the dark-current but increased the room-temperature photo-response dramatically. There was, however, little change for the low-temperature photo-conductivity. Increasing the Au NC concentration further by two orders of magnitude enhanced the room-temperature dark-current only slightly, but the photo-currents were reduced almost completely for all temperatures. History-effects made obtaining quantitative temperature dependence data difficult, but an overall trend of increasing photo-current with decreasing temperature was identified. CdSe nanorods displayed significant dark-currents, even in mono-layer films, but did not show increased current during photo-excitation. Finally, PbSe NCs did not yield any current, even with photo-excitation, despite TEM imaging showing a high degree of array order and good contact to the electrodes. Measurements made with nanogaps on a small PbSe NC array, however, did result in measurable current. TEM correlation revealed valuable structural information that was used to interpret some key features of the *I-V* curves obtained from the small array.

Electrostatic Force Microscopy (EFM) measurements of charge injection by electrodes into PbSe NC arrays and correlated imaging with TEM is discussed in Chapter

6. As deposited PbSe NC arrays were highly resistive, consistent with the *I-V* results discussed in Chapter 5. However, EFM imaging did reveal that the arrays do charge, albeit very slowly. Mild annealing increased the charging rate in the PbSe NC arrays significantly. Complementary TEM imaging of these devices proved to be extremely valuable and significant insight in to the charging behavior of the arrays was revealed by correlating array structure with EFM signals. In particular, it was found that highly ordered NC mono-layers were still resistive after annealing, even though charging rates in multi-layers, consisting of as little as two layers, increased significantly.

Detailed measurements of the electronic memory effects in annealed CdSe NC arrays measured in micron-scale gaps using a FET device geometry are summarized in Chapter 7. It is shown that conduction through a NC array can be reduced with a negative voltage and then restored with a positive voltage. It is also shown that light can be used to restore or even increase the NC array conduction. Conduction switching in CdSe NC arrays was found to be highly sensitive to the value and duration of the laser and voltage pulses and it was demonstrated that controlled exposure to these parameters can be used to make NC devices function as robust non-volatile memory elements.

The remaining chapters describe novel nanofabrication techniques that were developed in parallel with the nanocrystal transport research, as well as some of their applications. Chapter 8 describes a method for fabricating nanogaps directly with electron beam lithography (EBL). The primary resolution-limiting factors in EBL, electron back-scattering and secondary electron generation, are reduced dramatically by using an insulating thin-film (the SiN_x window) as a substrate. The result is a \sim 10-fold enhancement of EBL resolution. This chapter focuses on using this method to fabricate metal electrodes with separation from arbitrarily large to under one nanometer. Furthermore, because these nanogaps are on a thin film, they can be imaged with high-resolution transmission electron microscopy (HRTEM). Nanogaps

made with this technique were used to measure charge transport through several coupled PbSe NCs and correlate the data with detailed structural information obtained by performing HRTEM on the same device. This measurement is discussed in the context of general NC transport results in Chapter 5.

Chapter 9 discusses using the imaging beam of the HRTEM to fabricate metal nanostructures and devices, with ultra-high resolution and accuracy, on the SiN_x windows by nanosculpting metal films. Fabricated devices include nanogaps, nanodisks, nanorings, nanochannels, and nanowires with tailored curvatures and multi-terminal nanogap devices with nanoislands or nanoholes between the terminals. Several potential applications of devices made with nanosculpting, such as a novel device for use in DNA sequencing research, are also discussed.

The nanosculpting technique was also used to achieve high-resolution modification of suspended multilayer graphene sheets. Chapter 10 discusses the application of nanosculpting to realize, on time scales of a few seconds, a variety of features in the graphene sheets, including nanometer-scale pores, slits, and gaps that are stable and do not evolve over time.

Chapter 2

Device Design, Function, and Fabrication

2.1 Design and Function

Figure 2 shows a typical device used to study nanocrystal (NC) electronic properties. It consists of a lithographically defined metal pattern of wires on a silicon nitride (SiN_x) substrate. Large square contact pads are connected via intermediate size wires to measurement electrodes. These electrodes are situated over a small region of the surface which is freely suspended as a thin membrane, whereas the remainder of the substrate is not freely suspended. This region is often referred to as the window. Figure 2.1(c) is an image taken with a scanning electron microscope (SEM). Here the metallic contact pads and wires can be seen clearly as bright features because metal emits electrons when irradiated with electron beam; a response which is required for detection with an SEM. Figure 2.1(d) shows the device at a higher magnification, where the suspended region can be seen in the middle as a black square because its nominal thickness allows the imaging electron beam to pass through it without appreciable scattering. Figure 2.1(e) shows a higher magnification image of the device obtained with a transmission electron microscope (TEM), where now the window appears bright while the area away from the window and the metal wires on the window appear dark because these regions scatter the imaging beam

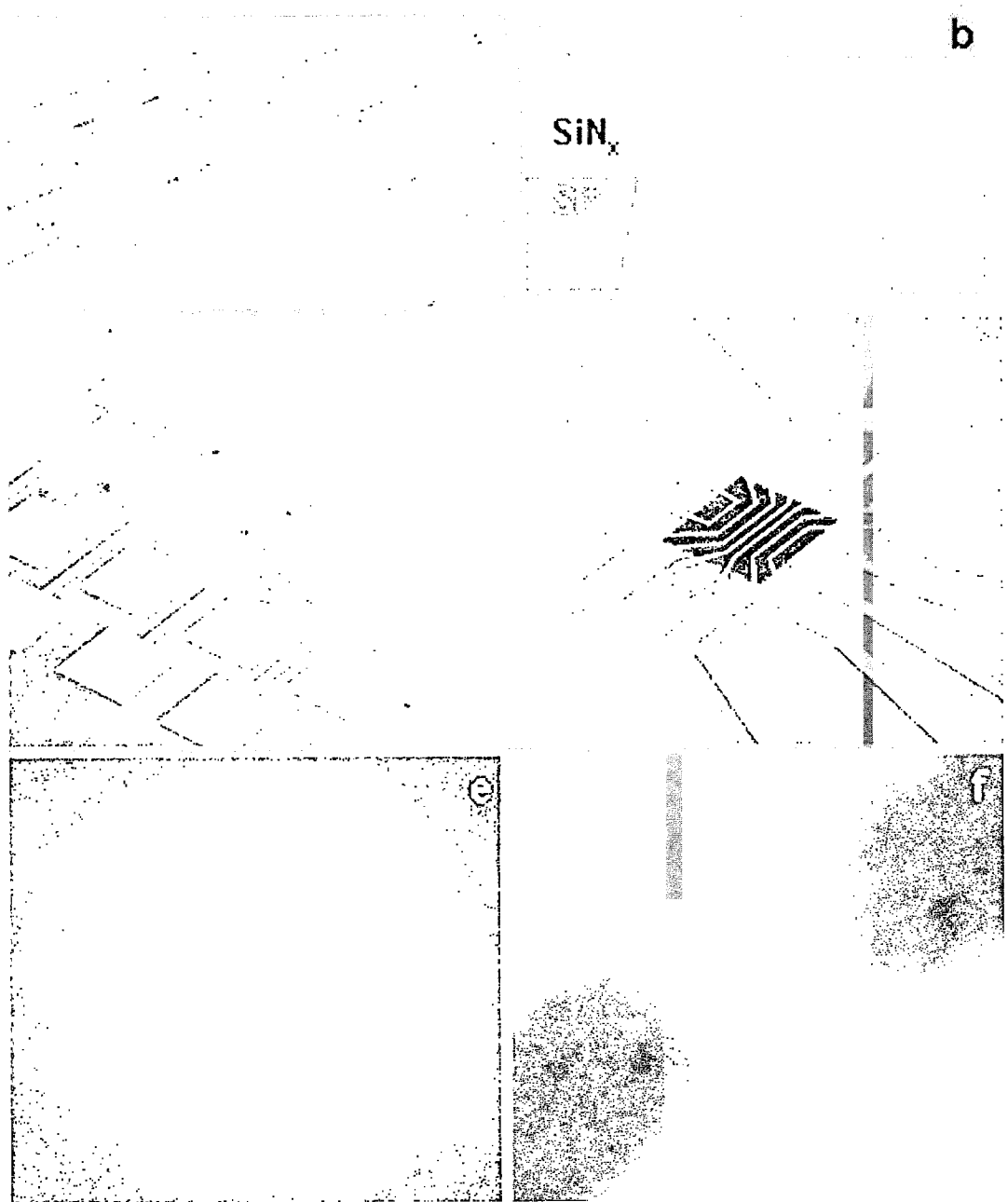


Figure 2.1: (a) schematic of a SiN_x window device with electrodes patterned onto the surface. (B) schematic cross-section of the device showing the Si removed from beneath the middle region under the SiN_x . Au electrodes are separated by a gap where samples can be measured and imaged with TEM (c) SEM image of a sample device use in the measurements on nanocrystals (d) SEM image of the same device taken at higher magnification. (e) TEM image of the device. (f) TEM zoom-in of an electrode pair where PbSe NCs are seen self-assembled into the gap.

significantly. Figure 2.1(f) shows a higher magnification TEM image where gaps between the electrodes are seen clearly. NCs were studied by introducing them into similar electrode gaps and measuring the amount of current passing from one electrode to the other electrode, through the NCs, as a function of the electrochemical voltage difference between them, generated by external power sources.

As shown in the cross-sectional schematic in Figure 2.1(b), the device substrate consists of silicon nitride (SiN_x) on doped Si, where Si was removed from beneath the SiN_x in a limited region to achieve a window. Electrode gaps were lithographically fabricated on top of the window, making them and their content compatible with TEM imaging. In addition to being compatible with TEM imaging, SiN_x membranes are an excellent platform for device manufacturing; they have a dielectric constant of $\sim 6.5 - 7.2$ and a breakdown voltage of $\sim 10^7 \text{ V/m}$, making them an attractive alternative to SiO_2 ^[80]

2.2 Fabrication

The fabrication of substrates containing windows is well documented in existing literature and it is straightforward to fabricate many of them in parallel^[81]. The process is illustrated in Figure 2.2. 500 μm thick ($\pm 50 \mu\text{m}$) doped $<100>$ silicon Si+ wafers with highly polished, 100 nm thick SiN_x layers grown on both sides are first coated with photoresist. Photolithography is then used to remove a square region of the photoresist, thereby revealing the SiN_x underneath. This side of the wafer is then exposed to a SF_6 plasma etch (400 mTorr environment, 50 W exposure for roughly 120 s), which removes a square of SiN_x , revealing the Si+ underneath. Finally, the wafer is exposed to a KOH wet etch (250 g of KOH pellets dissolved in 500 mL of deionized ultra-pure water, heated to 130 C). The KOH etches anisotropically through the Si+ along lattice planes until the SiN_x on the other side of the wafer is revealed. The time required for the wet etch to complete can range from 9 to

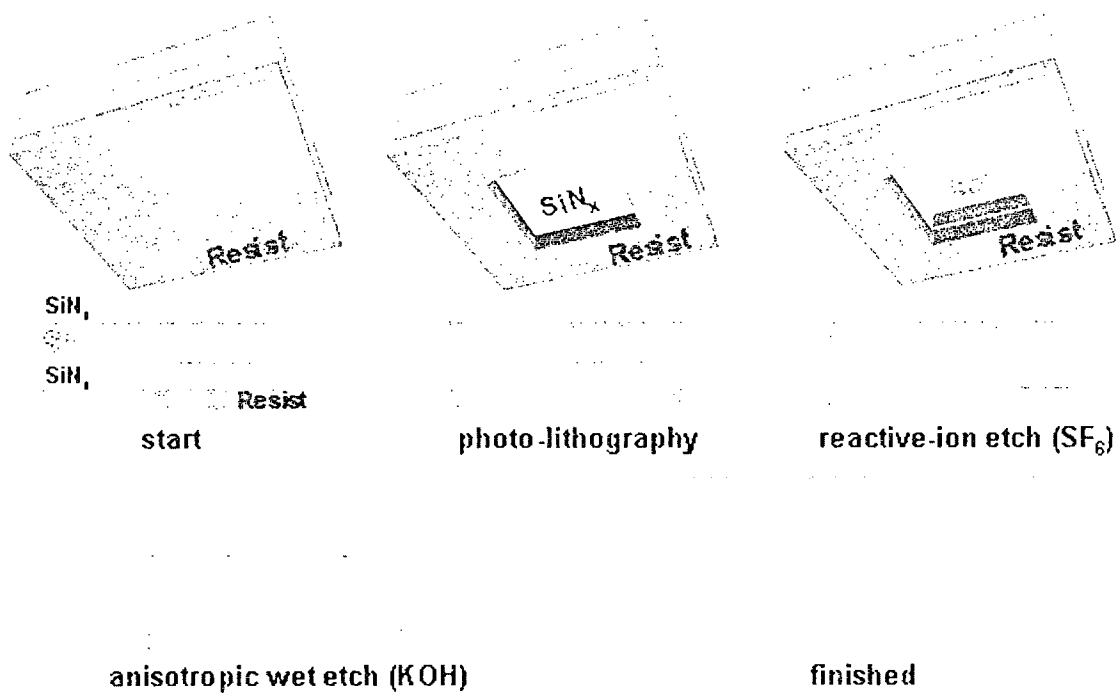


Figure 2.2: Stages of making SiN_x suspended membrane window devices.

over 24 hours. This variability is attributed to the varying Si thickness between different wafers and possibly varying amounts of SiO_2 at the Si- SiN_x interface. Once the etching is complete, a free standing membrane window of 100 nm thick SiN_x is therefore defined. Window dimensions were designed to be approximately $50 \times 50 \mu\text{m}^2$, though variations of order 10 μm are sometimes observed, most likely because of non-uniform wafer thickness. Typically, the free standing area is then etched with SF_6 down to 20 - 40 nm to improve TEM imaging and to slightly reduce proximity effects during electron beam lithography (EBL).

Electrodes were patterned onto the window with EBL. EBL was performed using a thermal-emission JEOL 6400 scanning electron microscope SEM operating at its maximum accelerating voltage of 30 kV, with writing capability controlled by Raith software (Elphy). Electrode gaps were written using parameters optimized for achieving high-resolution on this EBL system. A layer of EBL resist (950 molecular weight PMMA, 2% in chlorobenzene) was spin-cast onto the SiN_x window substrates at 5000 rpm to achieve a resist layer of 100 nm and then baked on a hotplate at 180 C for 10 minutes. Gaps were written onto the window region using a 10 pA electron beam in the EBL chamber with pressure below 10^{-6} Torr. The resist was exposed at a magnification of 2000, corresponding to a write field of $40 \times 40 \mu\text{m}^2$, to beam doses of approximately 750 C/cm². This dose, used only for the suspended region, is higher than in typical EBL cases and was needed to compensate for the substantial reduction in secondary electrons and backscattering due to the absence of the Si layer in this region. Larger features were then written into the resist to connect the electrodes to contact pads with EBL parameters in the ranges 1-20 nA beam current, 25-850 magnification, and 400-600 C/cm². The PMMA was then developed in a MIBK:IPA solution (1:3 volume ratio) for 60 seconds at room temperature. After drying with N₂ gas and confirming the pattern integrity with a light microscope, devices were loaded into the low pressure (of order 10^{-6} Torr) environment of a thermal evaporator. For metallization, several nanometers of either nickel or chromium

were evaporated first to act as an adhesion layer between the gold and the substrate, followed by 30 to 60 nm of gold. Nickel was found to be preferable because it resulted in substantially less metal debris forming along the edges of the lithographic features. The wafers were put into either acetone or dichloroethane at room temperature for several hours to dissolve the resist and then lift-off was achieved by using a dropper to encourage aggressive solvent flow across the device surface. With both the large and small features written into the same thin resist, lift-off would often be problematic in the region of the small features. High efficiency lift-off was achieved by separating the small electrode fabrication from the larger features, though this required two full rounds of fabrication and an alignment procedure. In this approach, the small electrodes were fabricated as described above, and after lift-off the device was rinsed with IPA, dried with N₂ gas, and the large feature fabrication was performed. One successful resist profiles used a lower molecular weight (495) PMMA spin cast at 3000 rpm to achieve a 400 nm layer. Better still was the use of a double layer resist consisting of a 950 molecular weight layer on top of a 495 molecular weight layer, in which case each layer was spin-cast and baked separately. An additional advantage of separating the small and large feature fabrications was the ability to achieve 100 nm thick contact pads, which could withstand wirebonding with a mechanical wedge bonder, whereas bonding to the 30 nm pads were more delicate and required the use of conductive paste and fine wire manipulated by handheld tweezers.

Chapter 3

Measurement Setup

Figure 4 shows several images of the system used to perform variable temperature transport measurements of NCs at low pressure. Measurements were conducted inside of a modified Janis ST-100H cryostat capable of achieving temperatures from 1.5 to 800 K. An Alcatel turbo-pump was used to achieve vacuum pressures ranging from 5×10^{-7} Torr at room temperature to 1×10^{-7} Torr at 77 K down to 6×10^{-8} Torr at 4 K. A Lakeshore Temperature Controller unit was used to monitor the sample stage temperature via either a thermocouple for temperatures between 40 - 800 K or a silicon diode for accurate measurements below 40 K. The Lakeshore was also used to control resistive heating of the stage when needed.

Temperatures down to 4 K were achieved by flowing LHe from a dewar kept at several psi through a thermally insulated transfer line directly coupled to a copper cold finger inside the cryostat. The cryostat base temperature could be reduced to 1.5 K for several minutes at a time by stopping the LHe flow and connecting a roughing pump to the exhaust valve. After several minutes the temperature will begin to rise as the LHe vaporizes completely. LHe flow is then resumed until a stable temperature of 4 K is reached, at which point the process of reducing to 1.5 K can be repeated. In cases where such low temperatures are not necessary, a LN₂ dewar

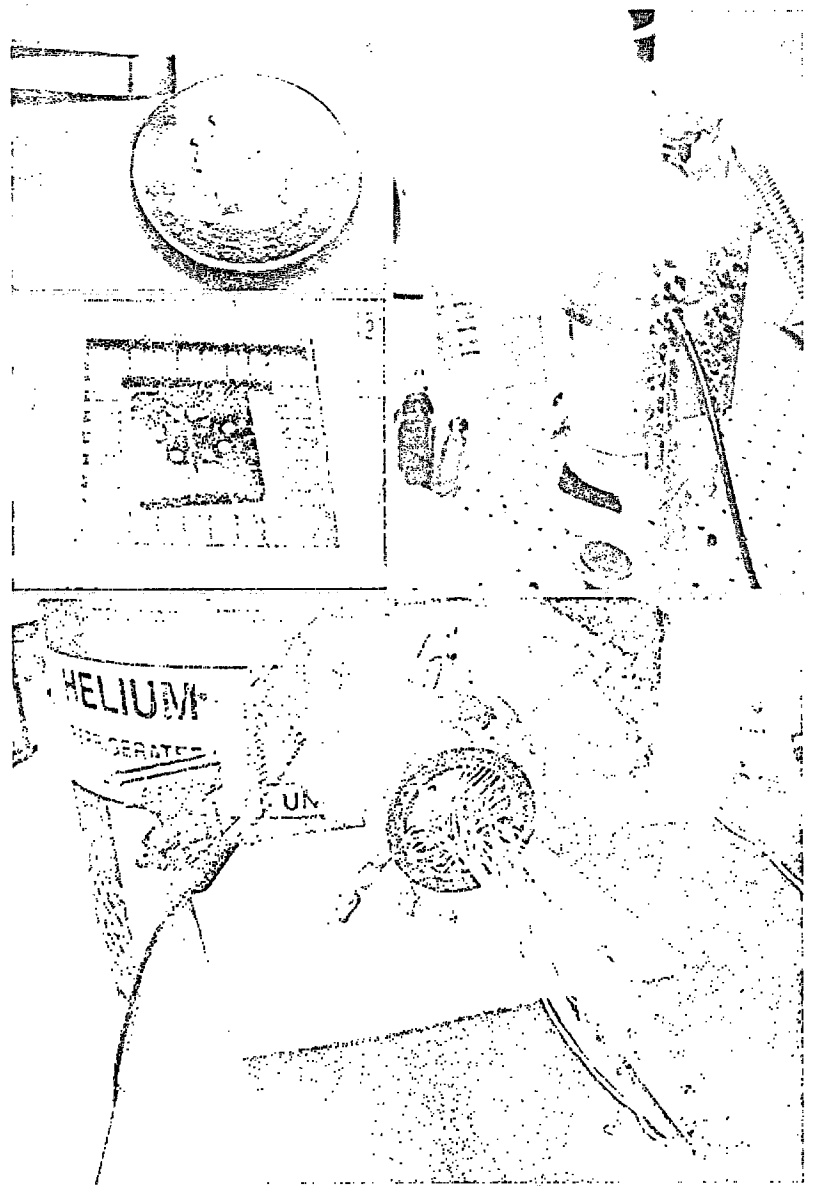


Figure 3.1: (a) Typical SiN_x device used for NC measurements. (b) SiN_x device wired to a chip carrier. (c) Chip carrier plugged into the cold finger socket. (d) Cryostat at 4.2 K.

can be attached to the cryostat in place of the transfer line. In this configuration, 77 K is easily achieved by filling the dewar with LN₂. The temperature can then be tuned from 77 K to room temperature with resistive heating.

Measurement devices were affixed to a ceramic chip carrier with silver paste and its contact pads were electrically connected by Au or Ag wire to the chip carrier's pins by using either a mechanical wedge bonder or silver paste and then plugged into a socket at end of the copper cold finger. The socket was designed to allow good thermal coupling between the ceramic and copper while keeping the socket pins thermally isolated with macor insulation. Device electrodes were addressed by wires, silver-soldered to the socket pins, that electrically coupled the chip carrier to two independent BNC breakout boxes, each used for either a source or drain connection. Keeping the source and drain BNC connections separate helped to reduce parasitic capacitance and leakage current. Voltages were applied with a Yokogawa 7651 programmable dc source, and current signals were amplified and filtered by a Keithley 428 current amplifier and then measured with an Agilent 34401A 6 1/2 digital multimeter (DMM). The current amplifier was typically set to 100 ms rise-time with a gain between 7 and 11 V/A, depending on the conductivity of the sample. Instrument control and data acquisition was achieved with LabVIEW software. With the DMM set to its highest accuracy, the time to acquire each data point was ~ 300 ms. For current-voltage characterization, typical voltage sweep rates were in the range of 1 to 100 mV/s, depending on the desired measurement resolution and presence of hysteresis. Measurements of bare chip carriers under vacuum revealed the system measurement sensitivity to be in the range ~10 fA at room temperature and even lower at cryogenic temperatures. Prior to use in NC measurement, all devices were pre-screened for leakage current. After wiring a device to the chip-carrier, the measured background current usually increased only slightly, compared to the blank chip-carrier. Devices that resulted in a background current increase of more than several tenths of a pico-ampere were discarded.

Photo-current measurements were performed with a 532 nm laser source aimed through a window panel on the side of the cryostat.

TEM images of measured devices were taken with either a JEOL 2010 or JEOL 2010F electron microscope, both operating at 200 kV.

Chapter 4

Sample Preparation

CdSe and PbSe NC spheres, dissolved in either hexane or toluene solvents were provided by Evident Technologies (since acquired by Invitrogen) and stored until use in the dark in a refrigerator. Au NC spheres dissolved in hexane were provided by Applied NanoWorks. CdSe NC nanorods (NRs) were synthesized by Dr. Claudia Querner, a synthetic chemist conducting research as a postdoc in Dr. Drndic's lab. The NRs were prepared using a standard hot injection method. In detail, the Cd precursor was prepared by heating cadmium oxide (61.7mg, Aldrich, 99%), decylphosphonic acid (227.3 mg, Alfa Aesar, 99%), and tri-n-octylphosphine oxide (2.998 g, Aldrich, 90%) at 300 C under inert atmosphere. Then, selenium powder (74.1 mg, Aldrich, 99.99%) dissolved in tri-n-octylphosphine (2.00 g, Aldrich, 90%) was injected rapidly at 290 C. After 15 min, the heat source was removed to stop the reaction. The NRs were precipitated and purified by washing several times with methanol. Finally, CdSe NRs were redispersed in hexane or hexane/octane mixtures for further characterization. NRs were characterized in solution by absorption and emission spectroscopy using USB2000 and USB4000-FL (excitation: 518 nm LED, 35 mW) spectrometers, respectively, from Ocean Optics.

For the purpose of achieving ordered NC self-assembly in the solid state, it was

found to be effective to drop-cast the NCs from a solvent mixture of hexane and octane (9:1 volume ratio). To transfer NCs from toluene, the initial solution is poured into a vial and an equal volume of a non-solvent, such as methanol, is added and mixed briefly to encourage the NCs to precipitate out of the toluene. The solution is then centrifuged at 14,000 rpm for 10 minutes to separate the NCs from the solution and encourage them to aggregate on the walls of the vial. After centrifugation, the toluene and methanol mixture is poured out and replaced with the hexane/octane solution, in an amount chosen to achieve a desired NC concentration, and the solution is then shaken briefly to dissolve the NCs. Typical concentrations that resulted in NC mono-layers after drop-casting and evaporation of 50 μL of NC solution on a surface with area of order 10 mm^2 were $\sim 10^{-8}$ mol/L, which corresponded to the liquid appearing *almost* clear under typical room light. In general, solutions with readily noticeable color resulted in many NC layers. In the case of drop-casting onto a highly structured surface, as in the case of a measurement device, solvent evaporation is non-uniform and NC self-assembly can vary significantly over micron distances.

Due to the ability of CdSe and PbSe NCs to oxidize in air, particular care was taken to minimize their exposure during the time between drop-casting onto a measurement device and loading the device into the cryostat chamber. Before drop-casting NCs from solution onto a device, the device would be first cleaned by exposure to O₂ plasma in a reactive ion etcher (RIE) for up to 20 minutes, with gas flow regulated to achieve a 400 mTorr chamber pressure and power set to 40 W. The freshly cleaned device was then wired to a chip carrier, plugged into the cryostat socket and the pin connections were checked with an ohmmeter before retrieving a prepared NC solution from storage. At this point, all of the BNC sockets were plugged with grounding caps so that the device electrodes were at a common potential. With the chip carrier kept level, a single drop of NC solution, approximately 50 μL , would then be dropped onto the device surface and allowed to evaporate for

roughly one minute until the droplet surface appeared to be flat against the device surface. This criterion was intended to allow for substantial NC self-assembly before tilting the device to insert it into the chamber and rapidly reducing the environmental pressure. The cold finger was then quickly loaded into the chamber, the vacuum bellows attached, and the turbo-pump activated to evacuate the chamber, which after several minutes would be in the 10^{-5} Torr range. Devices were typically pumped on overnight to allow the chamber pressure to settle to its base value and the device to dry completely before beginning measurements.

Chapter 5

Nanocrystal Transport Measurement and Correlated Imaging by Transmission Electron Microscopy

5.1 Introduction

The electronic properties of various nanocrystal (NC) assemblies were studied by drop-casting from solutions of various NC concentration onto TEM compatible SiN_x substrates with lithographically patterned source and drain electrodes, allowing them to self-assemble in the electrode gaps, and then measuring lateral conduction in the dark and with exposure to 532 nm (green) laser light. NC assembly was not interfered with during or after droplet evaporation and, in particular, no annealing or chemical treatment was performed on any of the devices discussed in this chapter. Following measurement, devices were removed from the cryostat stage and imaged with TEM to determine assembly structure and inspect general device features. The NC types studied were PbSe spheres, CdSe spheres, mixtures of CdSe and Au spheres, and CdSe rods. Following convention, NC spheres will be referred to as NCs and NC rods will be referred to as NRs. Typical electrode gap sizes were of order 100 nm in separation and 500 nm to 1 μm wide, with electrode heights between 35 and 80 nm.

Gaps with several nanometer separation were also used to study small clusters (10 or fewer) of PbSe NCs.

5.2 CdSe NCs

Current-voltage (*I-V*) characterization of CdSe NCs measured in the dark were observed to be highly resistive, with dark-current indistinguishable from measurement noise for applied source-drain voltage sweeps from -5 V to 5 V. Dark-current was occasionally observed with higher applied voltage magnitudes, typically appearing between 8 and 15 V. However, the signals frequently became noisy at these higher voltages and the corresponding signal structure was often not consistent between sequential voltage sweeps. An example of this is shown in Figure 5.1, where three sequential dark-current measurements of a CdSe NC device are plotted. Furthermore, background measurements performed on bare devices (i.e., before drop-casting NCs) with applied voltage magnitudes swept to the 10 V range and higher were more likely to damage the device (e.g., cause breakdown of the SiN_x or blow up an electrode) than for voltages limited to ± 5 V. The majority of measurements on CdSe NCs were therefore kept in the ± 5 V sweep range. Figure 5.1 also shows that hysteresis is present in the measurements. The hysteresis is always dependent on the rate of the voltage sweep, growing for faster sweeps and are mainly due to system capacitance. Forward and reverse voltage sweeps are typically very similar and separated by gap in the current due to displacement current, $I = C \left(\frac{dV}{dt} \right)$. For clarity, the reverse bias portion of the *I-V* sweeps are not shown in the data shown below.

Figure 5.2 shows TEM images of a $100 \text{ nm} \times 1\mu\text{m}$ Au electrode gap device containing 3.4 nm CdSe NCs. As seen in the zoom-in images, the gap is completely filled with the NCs and the electrodes appear to make direct contact to the NC film. The CdSe NC film is disordered, in contrast to the triangular lattice arrangement which they often assemble into when drop-cast onto smooth substrates (c.f., Figure

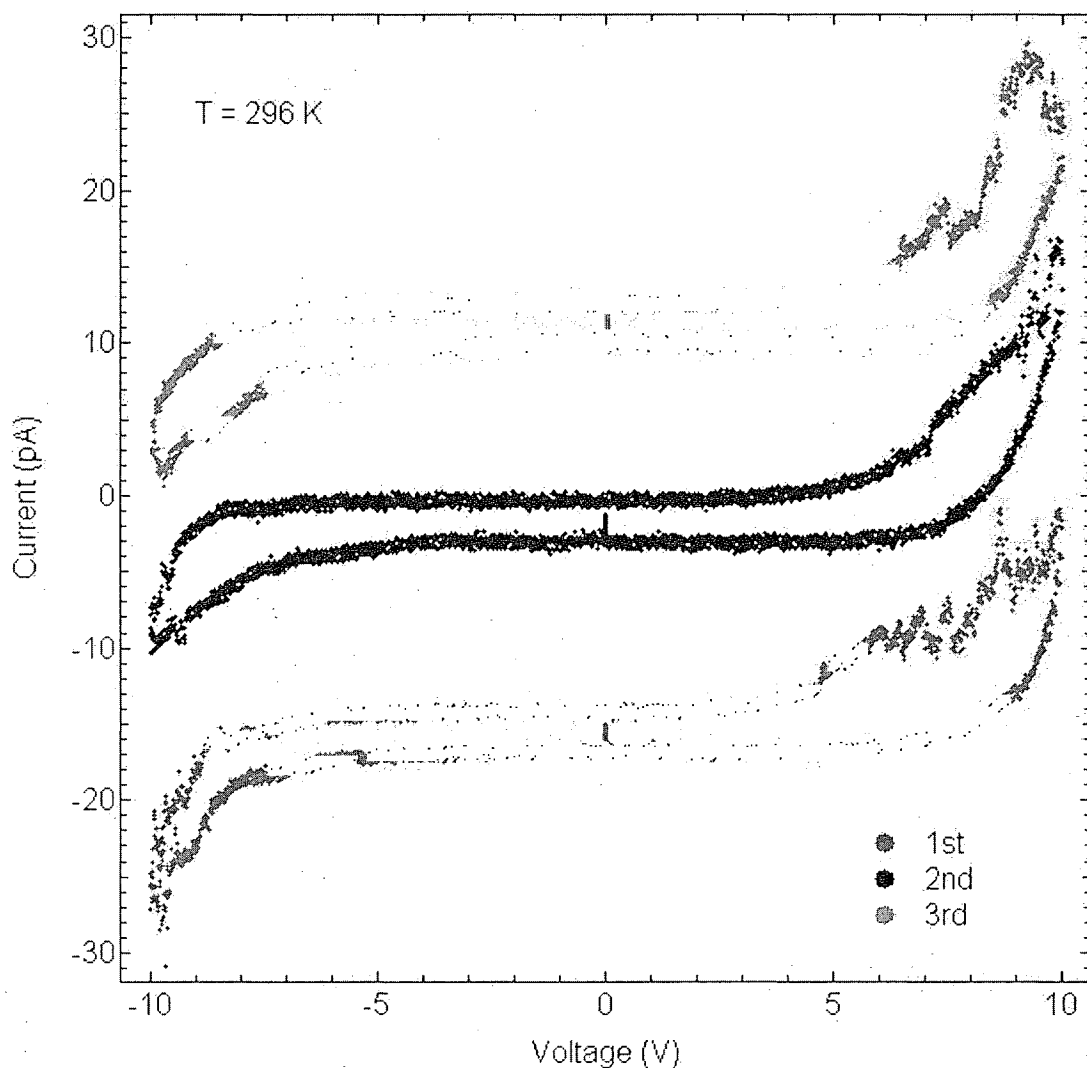


Figure 5.1: Three sequential current-voltage (I-V) measurements of a 3-dimensional CdSe NC array. The I-V curves are offset for clarity. The features seen in the non-zero current regions are not completely reproducible between sequential voltage sweeps. Hysteresis is observed due to system capacitance and history-dependent behavior of the NCs create a gap between the forward and reverse bias portions of each sweep. The reverse sweeps appear higher in magnitude than the forward sweeps. The sweep rates in these measurements was 100 mV/s.

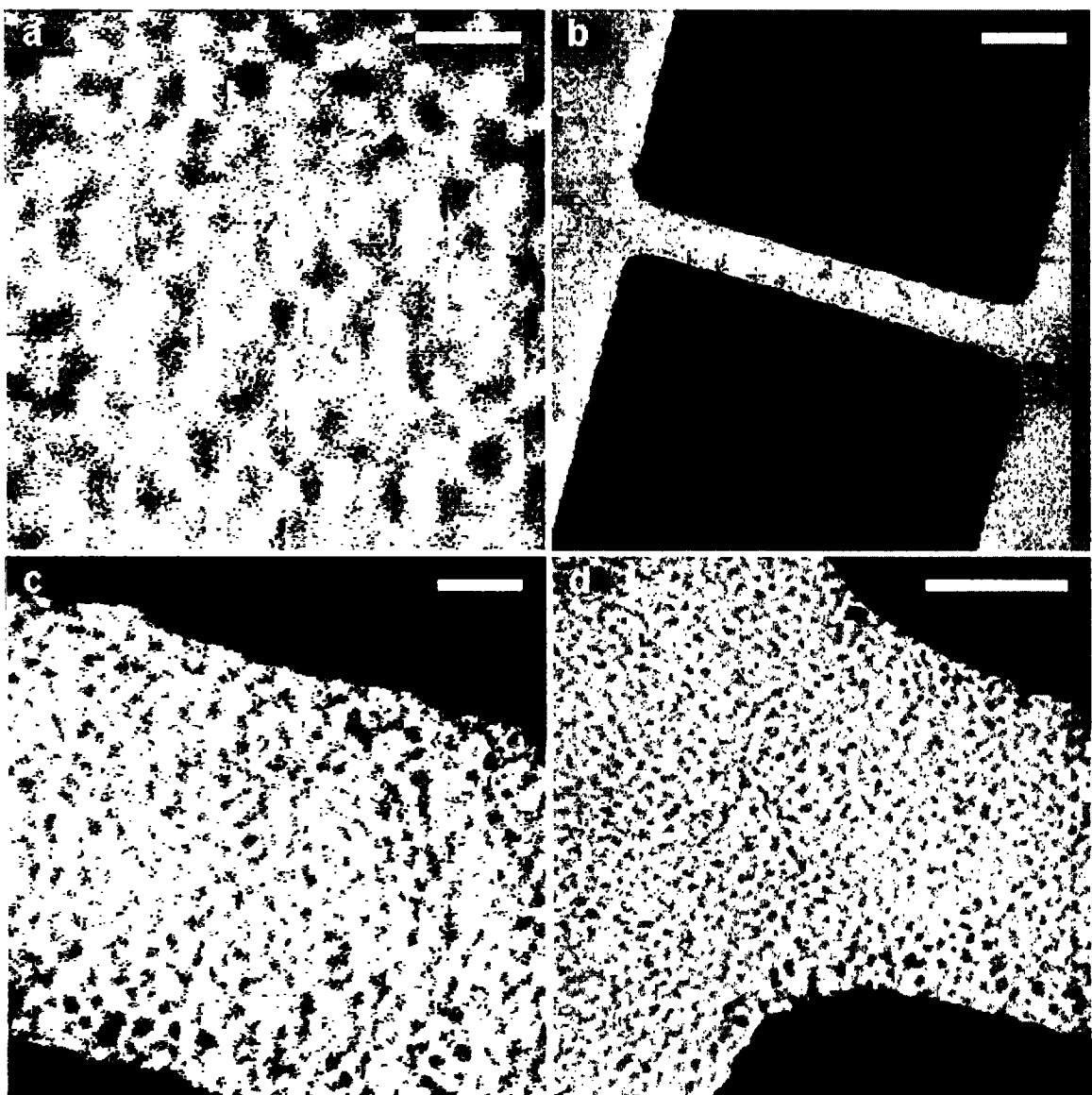


Figure 5.2: TEM images of a $100 \text{ nm} \times 1\mu\text{m}^2$ Au electrode gap device containing 3.4nm CdSe NCs. (a) Zoom-in of the gap region showing a disordered CdSe NC array. (b) TEM image of the full gap. CdSe NCs cover the surface and fill the gap. (c) TEM image showing good contact of the electrodes with the NC film. (d) TEM image of the left corner of the gap. From varying the focal plane during TEM imaging, it was estimated that the film was several NC layers thick. Scale bars are 10 nm, 1 μm , 20 nm, 50 nm.

1.1(d)). From varying the focal plane during TEM imaging, it was estimated that the film was several NC layers thick.

Figure 5.3 shows a representative *I-V* characteristic acquired at 78 K corresponding to the device shown in Figure 5.2, for measurements conducted in the dark and under photo-excitation with 532 nm wavelength light from a diode laser outputting approximately 1 mW/cm². In contrast to the immeasurable dark-current, photo-excitation of the device resulted in currents of several pico-amps, well above the measurement sensitivity of the setup. The photo-currents were linear in voltage throughout the measurement range, with a resistance of $\sim 10^{11} \Omega$ and corresponding resistivity of $\sim 5 \times 10^4 \Omega \cdot \text{m}$. Photo-enhancement of the current is expected only for illumination light with sufficient energy to produce electron-hole pairs,^[59] corresponding roughly to the wavelength of the size-dependent NC first absorption peak. These NCs had first absorption and emission peaks of 581 nm and 572 nm respectively. Consistent with this picture, illumination with red laser light, having a wavelength of 630 nm, substantially longer and out of the absorption range, did not produce a current enhancement effect.

Temperature dependence studies of CdSe NCs revealed an inverse relationship, where photo-conductance increased as temperature decreased. Figure 5.4 shows a set of *I-V* curves corresponding to a device that was cooled with LN₂ and measured as the temperature was increased slowly. The overall temperature sensitivity of the photo-current was rather dramatic, decreasing by two orders of magnitude as the temperature increases from 90 to 200 K. Changes in the photo-current magnitude for temperatures between 90 and 160 K also followed this inverse trend, but were very slight and the corresponding *I-V*s are not included in the plot for clarity. Furthermore, photocurrents above 200 K were very small and at room temperature photo-excitation produced no measurable current. The upper left inset shows a plot of conductance as a function of temperature. It is evident from this plot that the

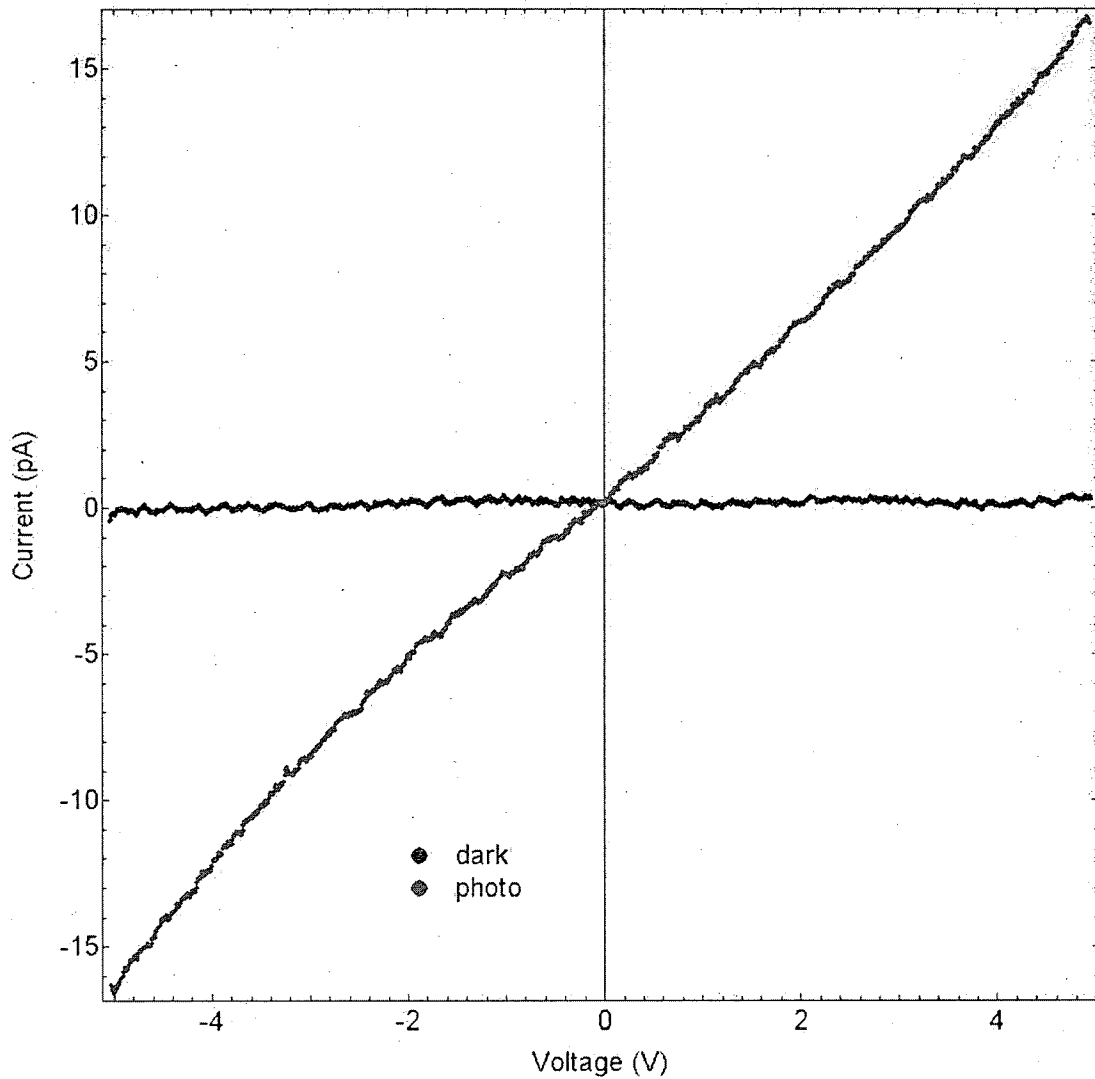


Figure 5.3: Dark and photo I-V characteristics measured at 78 K for the CdSe device in Figure 5.2.

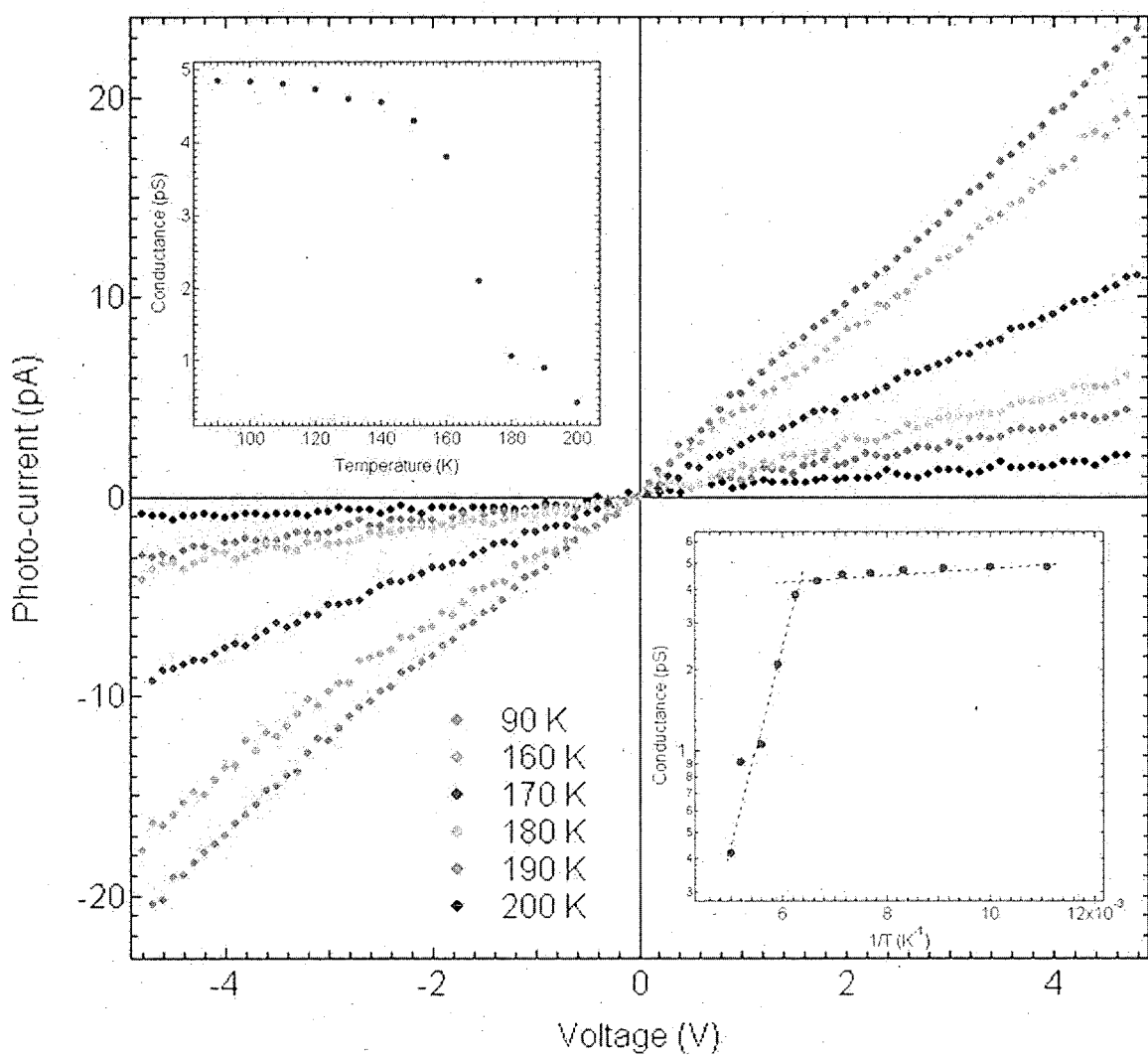


Figure 5.4: Photo-current measurements of the CdSe NC device shown in Figure 5.2 as a function of temperature. Inset (upper left) zero-bias conductance plotted versus temperature. Inset: (lower right) Arrhenius plot of zero-bias conductance against inverse temperature. Dashed lines were added to note the apparent presence of two temperature regimes. The current is higher at 90 K here than for 78 K in Figure 5.3 and is the result of history effects, which are discussed at length in Chapter 7.

decrease in photo-current is gradual up to approximately 150 K, where it then accelerates with increasing temperature. These two regimes are more clearly distinguished in the Arrhenius plot shown in the lower right inset of the temperature dependence figure. The inverse temperature dependence of the photo-current is evidence that the photo-conductivity is limited by exciton life-times and not charge traps in the film, since phonons assist in freeing trapped charges which ought to increase the current. Moreover, the observation of linear photo-current over this range of temperatures indicates that that field-assisted ionization of excitons is either insignificant or that its effect saturates at very low bias. Considering that the applied bias range used in these measurements corresponded to electric fields comparable to what was used in the previous studies in larger gaps, where non-linearity was regularly observed at a range of temperatures,^[59] it is unlikely that a non-linear regime was present but not observed for these smaller gap devices. The field independence therefore suggests that differences in site energies between neighboring NCs were well under ~ 100 meV, the scale of the voltage drop between two neighboring NCs for these applied voltages. However, that current saturation was not observed indicates that recombination was significant, i.e., not all carriers were extracted by the electrodes. Future measurements using devices designed to achieve higher fields without breaking down the SiN_x may reveal saturation and allow for a measure of the carrier mobilities.

5.3 CdSe + Au NC mixtures

Interesting electronic effects were observed in cases where 4.5 nm diameter Au NCs were mixed into the CdSe NC solution before drop-casting. Two cases were studied: one where the Au NCs were added in relatively small numbers compared to CdSe NCs and one where the number of Au and CdSe NCs were approximately equal. For the first case, a 1:5 mass ratio of Au to CdSe NCs was used. Using the density of Au (19.32 g/cm^3) and of CdSe (5.81 g/cm^3 , Wurzite) together with the known NCs

diameters, this mass ratio corresponds to 1 Au NC for every 35 CdSe NCs. In the second case, a 5:1 mass ratio of Au to CdSe NCs was used, corresponding to 2 Au NCs for every 3 CdSe NCs.

5.3.1 35:1 (CdSe:Au) Number Ratio

Figure 5.5 shows room temperature dark and photo current results from a device with the 35:1 (number ratio) CdSe + Au NC mixed assembly. An immediate distinction from the CdSe-only case is that the dark-current, though small, was measureable (see inset). It is also non-linear. Even more striking is that photo-excitation produced significant currents at room temperature, in contrast to the CdSe-only case. Furthermore, the photo-currents were non-linear. A significant history effect was also observed and repeated photo-current measurements led to qualitatively similar I - V curves, but with varying magnitudes. The data shown in Figure 9 correspond to five sequential current measurements. First, the dark-current was measured. Next, the photo-current was measured three times. Finally, the dark-current was measured again for comparison with the first dark measurement. The measurements were performed immediately after each other, corresponding to a \sim 4 minute separation between the start of each voltage sweep. The photo-current grew substantially with each measurement, increasing over 40 % (at \pm 5 V) by the third measurement. The dark-current was not significantly effected by the photo-current measurements, though there was an increase of a few percent. Measurements at lower temperature also displayed a history effect, but with an opposite trend. Figure 10 shows the results of performing the dark-photo-dark sequence on the same device at 78 K. Before beginning these measurements, the device was left unmeasured in the dark at room temperature for several hours to allow the effect of photo-excitation to decay. The 78 K data show that the effect of repeated I - V sweeps under photo-excitation at low temperature is to *reduce* the photo-current, but with less dramatic absolute changes (\sim 20 % decrease at \pm 5 V) compared to those at 296 K (\sim 40% increase at \pm 5

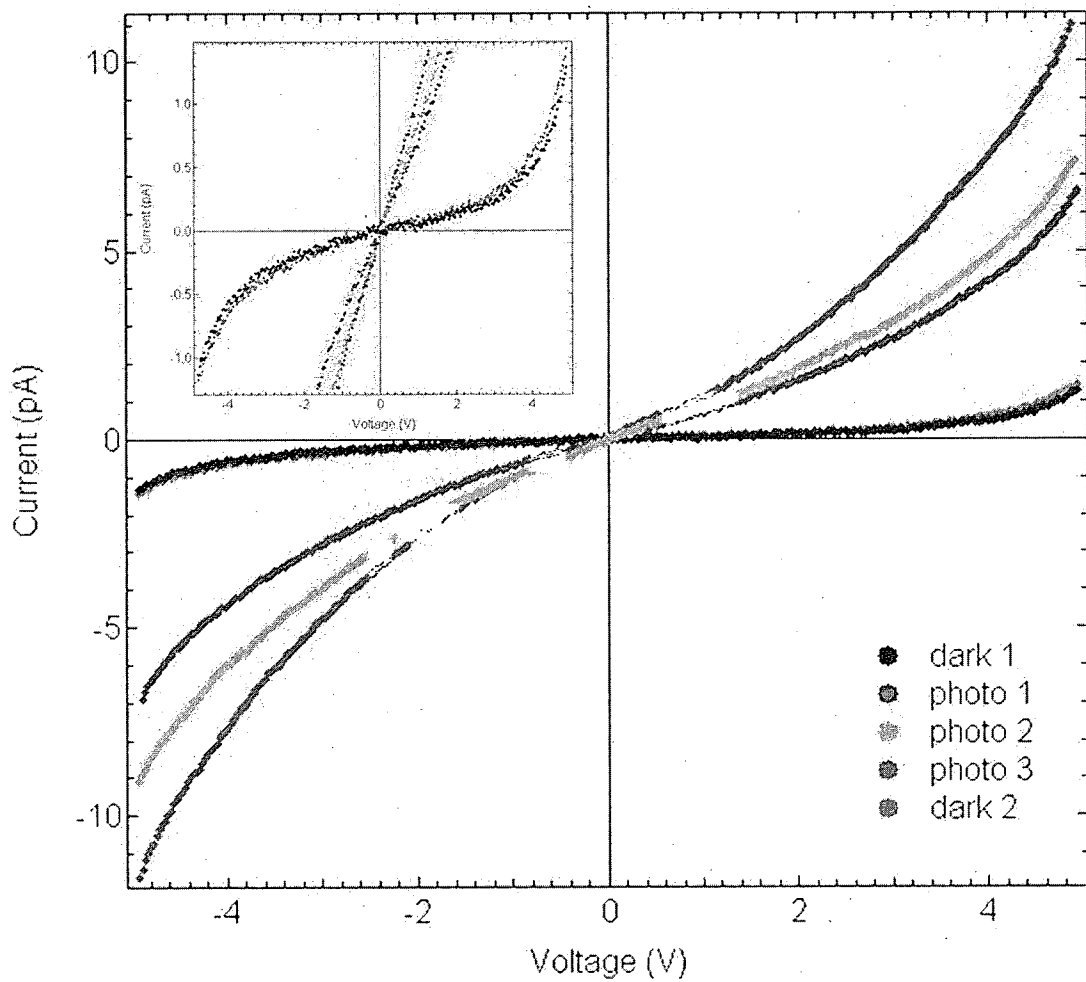


Figure 5.5: Dark and photo I-V characterization of a CdSe + Au NC mixture (35:1 number ratio) at room temperature. Inset (upper left) same plot at different current scale to better view the dark-current. Sequential photo-current measurements displayed history effects, while dark-currents did not change significantly.

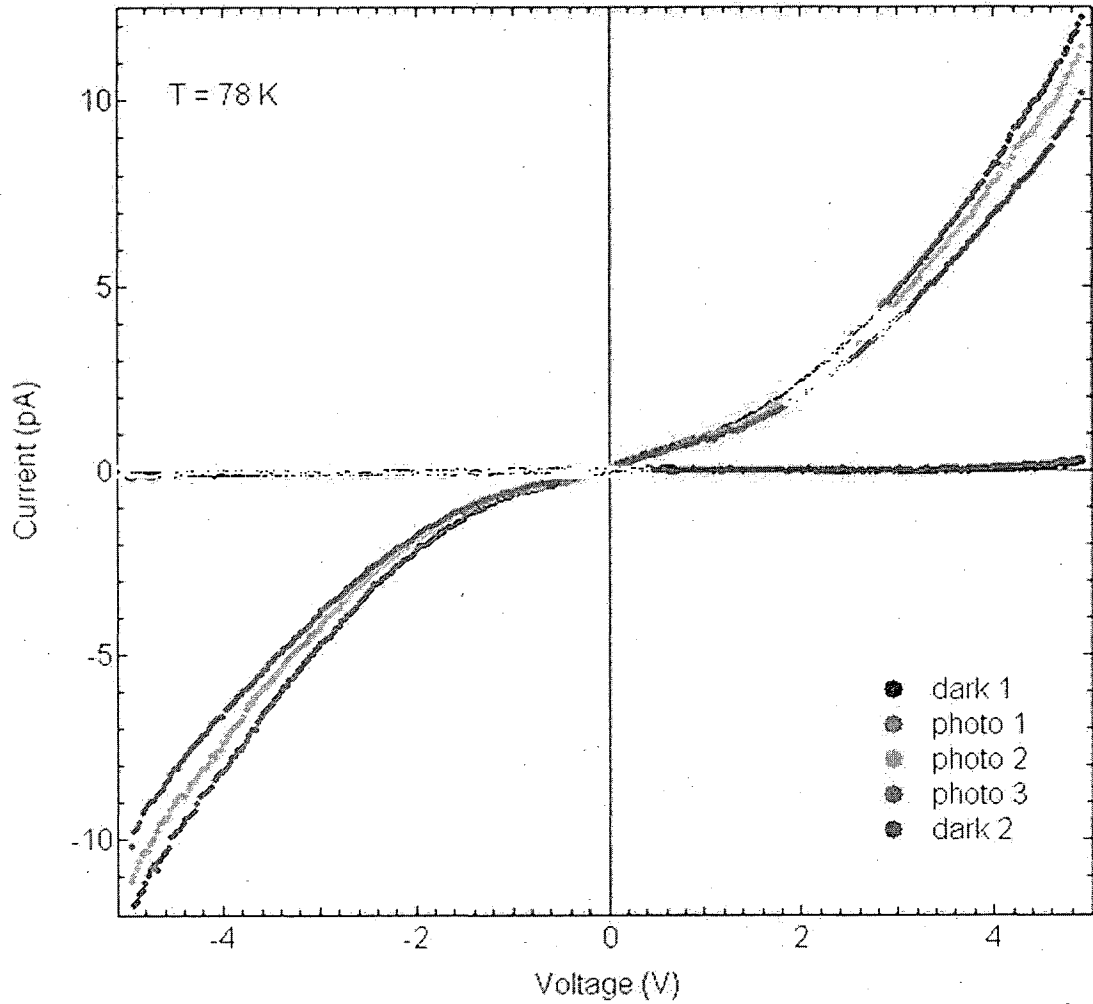


Figure 5.6: Dark and photo I-V characterization of a CdSe + Au NC mixture (35:1 number ratio) at 78 K. Sequential photo-current measurements displayed history effects, but with the opposite trend to what was seen at room temperature. Dark-currents were very small and any contribution of history could not be observed.

V). The dark-current was below the measurement sensitivity at this temperature and the effect of the photo-current measurements could not be observed.

Though these history effects may reveal valuable information about charge dynamics in the NC film, they complicate measurements of photo-current magnitude dependence on temperature. Figure 5.7 shows photo-current data taken at temperatures ranging from 24 to 212 K, taken several days after the measurements corresponding to Figure 5.6, during which time the device was left unmeasured at room temperature in the dark. The order of measurement is clearly important for interpreting the results. In obtaining the data shown in Figure 5.7, the first measurement was taken at 24 K and each subsequent measurement corresponded to a strictly monotonically increasing temperature (i.e., each measurement corresponded to a temperature that was the same or higher than the preceding one). Due to the processes required to cool the cryostat with LHe, the reverse measurement sequence, where low temperature is achieved last, would have necessarily involved substantial measurement perturbation (as well as vastly more LHe).

Even though the temperature dependence measurements were inherently convolved with history effects, it was still possible to extract a trend. As shown in the insets to Figure 5.7, the change in current for back-to-back photo-current measurements taken at 24 K is substantial, roughly 41 % at 4 V, while back-to-back measurements taken at 67 K displayed only a ~ 7 % decrease. Meanwhile, the decrease in photo-current between 67 K and 102 K was ~ 36 % at 4 V. Furthermore, the current reducing effect of multiple photo-current measurements decreases with increasing temperature and eventually turns around to begin increasing the photo-current. Therefore, the consistent decreases of the photo-current seen in Figure 11, each one over 20 %, cannot be due to history effects alone. This is obviously true in the temperature range where history effects serve to increase the photo-current. It can therefore safely be concluded that the effect of increasing temperature was to decrease the photo-current.

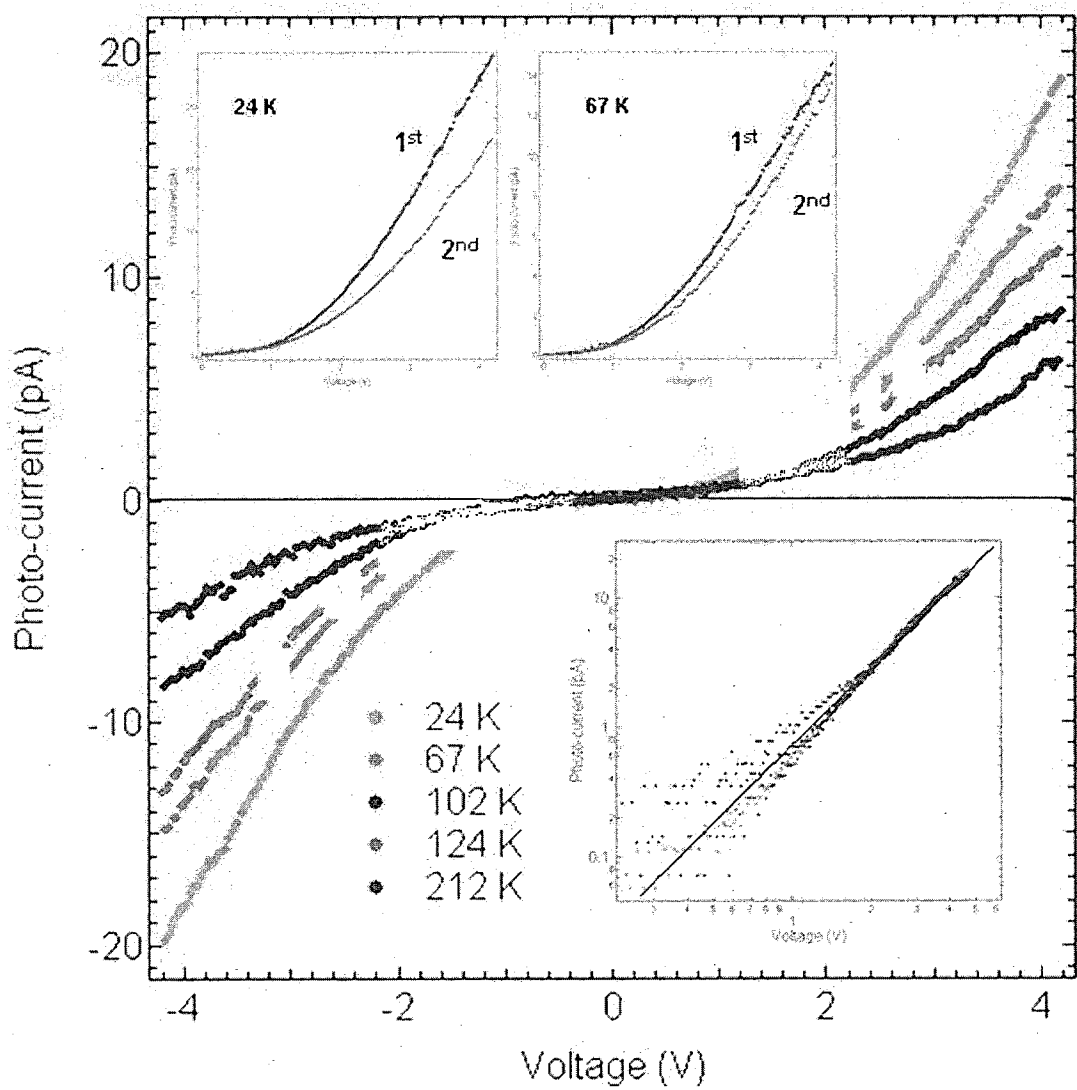


Figure 5.7: Photo-current of CdSe + Au NC mixture (35:1 number ratio) measured as a function of temperature. Insets: history effects seen at 24K (upper left) and 67K (upper right), log-log plot of the I-V curves (lower right). The dark straight line corresponds to quadratic behavior (included for reference).

In addition to the photo-current magnitude, the I - V shape was also observed to display temperature dependence. Specifically, the curvature of the photo-response was more pronounced at low temperature. However, a logarithmic plot of the I - V curves (see inset) reveals that the response is approximately quadratic at all temperatures, for voltages above roughly ± 1.5 V. No systematic trend was observed for lower biases.

5.3.2 3:2 (CdSe:Au) Number Ratio

The previous section demonstrated that introducing a relatively low population of Au NCs into the CdSe NC assembly resulted in qualitative changes, in both the dark and photo-current responses to applied voltages, compared to a pure CdSe NC assembly. Increasing the population of Au NCs in the mixture continued to qualitatively change the electronic properties. Figure 5.8 shows the room temperature response of a device containing a 3:2 (number ratio) CdSe + Au NC mixed assembly, in the dark and under photo-excitation. The dark-current is slightly higher than for the 35:1 ratio case. The photo-current is dramatically different than both the 35:1 ratio and CdSe-only cases. Although there is a clear increase in the current under photo-excitation, the change is only a factor of 2 larger than the dark-current at ± 5 V, much lower than the factors of 100 or more seen for the 35:1 ratio and CdSe-only cases. Furthermore, the photo-current in the 3:2 case *decreased* by over 40 % at ± 5 V, after cooling to 78 K (see Figure 5.9).

It is interesting to note that the photo-conductivity did not change in the linear regime and only decreased for voltages magnitudes above 3 V. Due to the photo-current values changing over such a small range between 296 K and 78 K, a systematic temperature-dependence study was not attempted for the 3:2 NC mixture.

Figure 5.10 summarizes the room temperature dark-current and 78 K photo-current behavior for the three CdSe NC cases studied. The dark-current (inset) trend was to increase for increasing Au NC population, though not by very much.

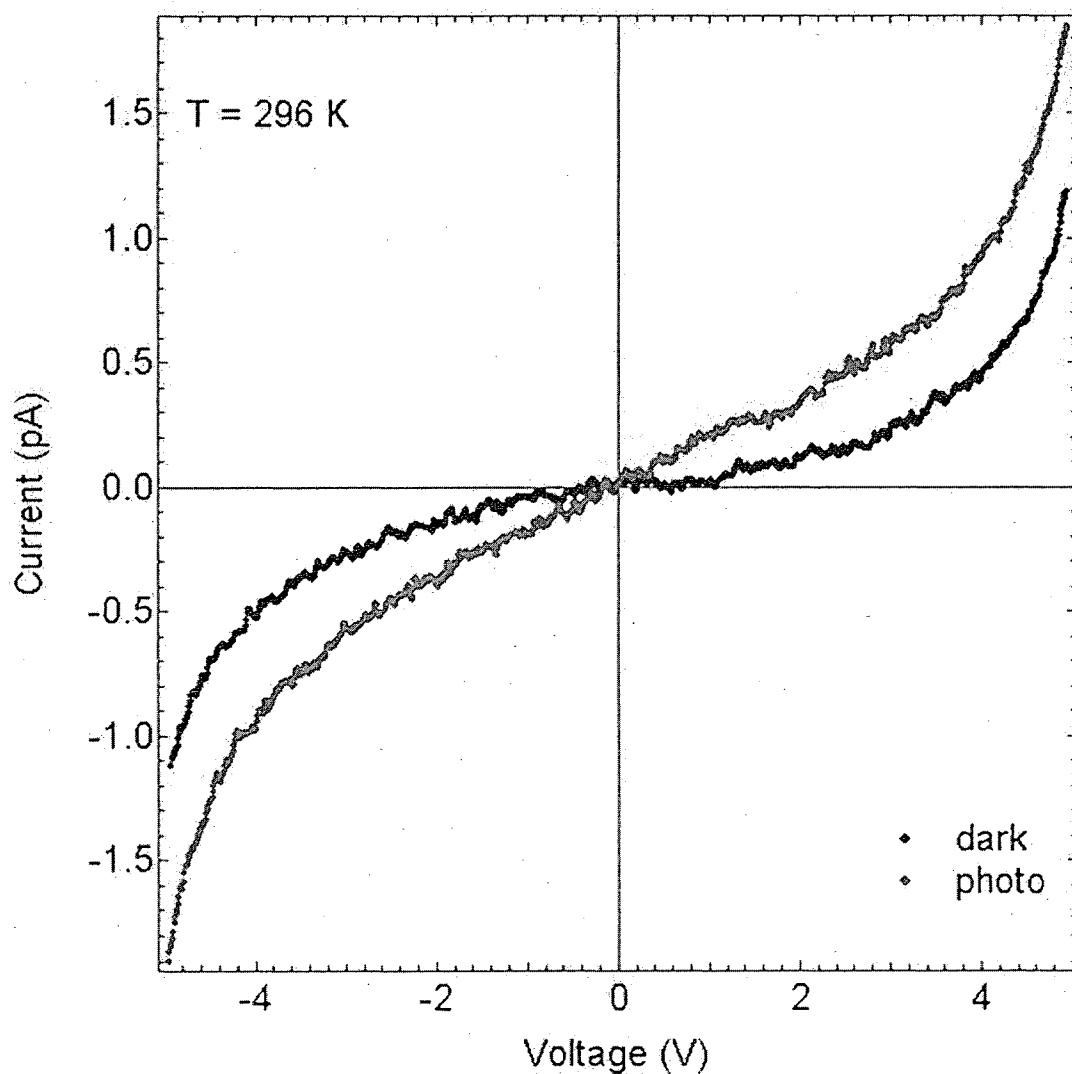


Figure 5.8: I-V characteristics of a CdSe + Au NC mixture (3:2 number ratio) measured at room temperature in the dark and during photo-excitation.

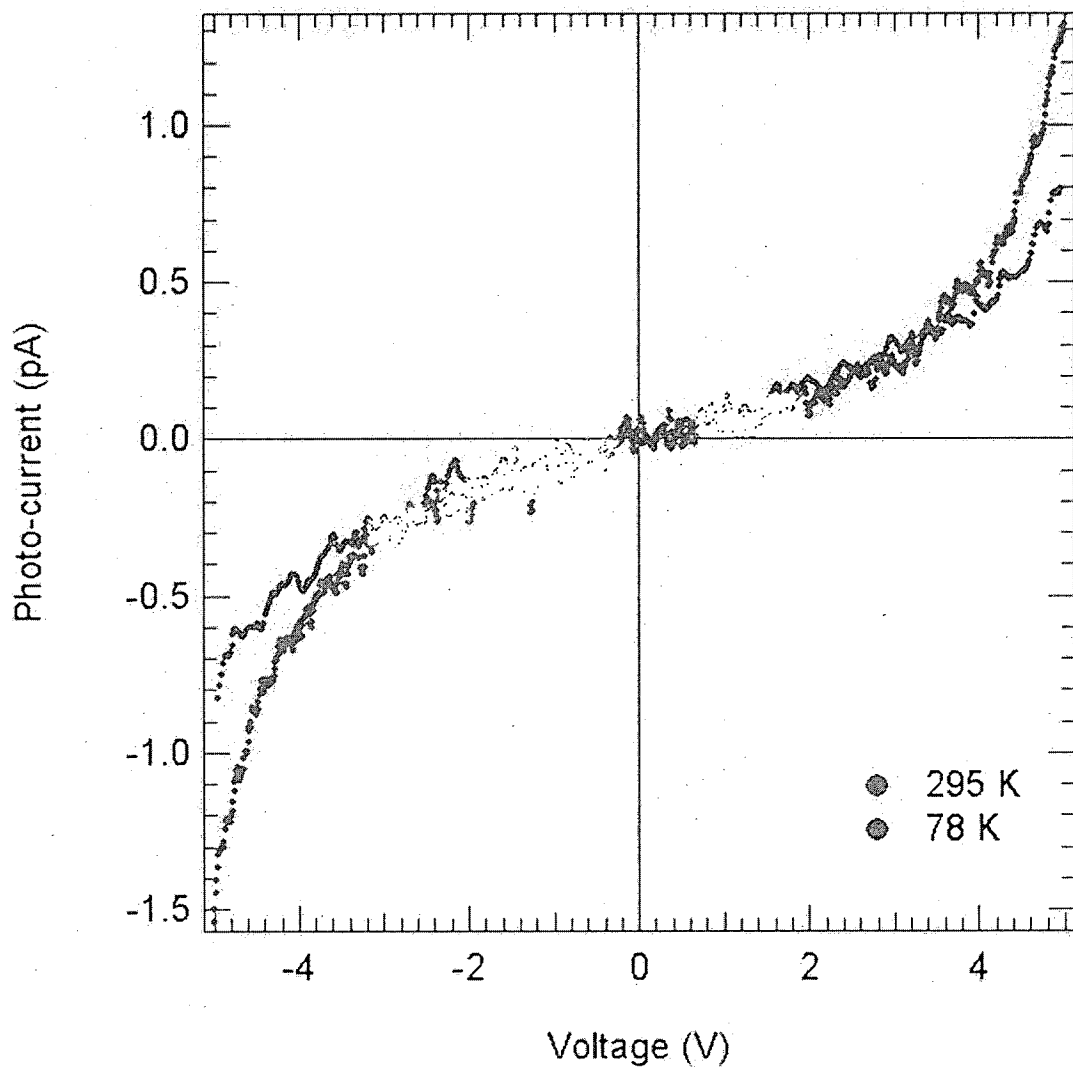


Figure 5.9: I-V characteristics under photo-excitation for a CdSe + Au NC mixture (3:2 number ratio). The photo-current is not effected significantly below 3 V. Above 3 V the photo-current is lower at 78 K than 296 K, in contrast to the temperature trend observed for the 35:1 ratio mixture.

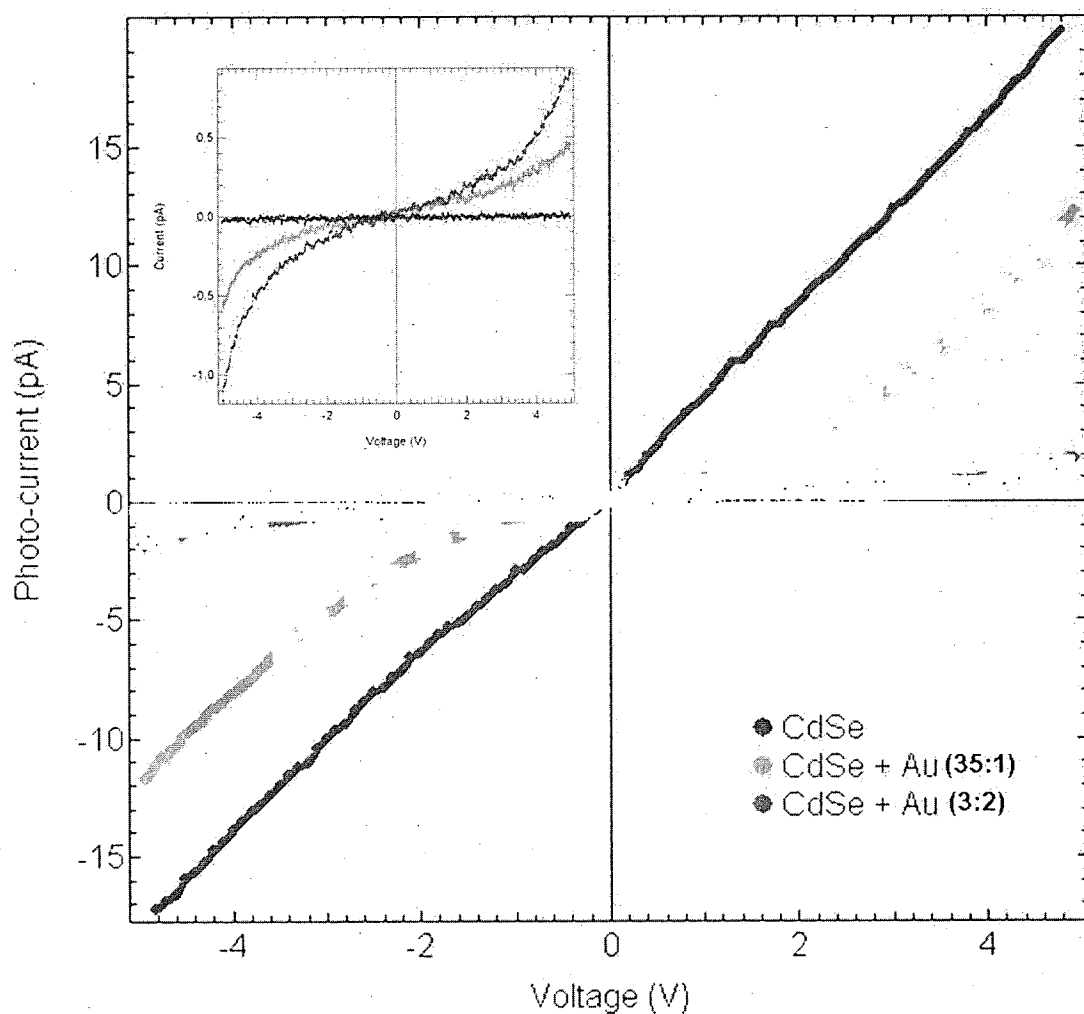


Figure 5.10: I-V characteristics under photo-excitation at 78 K for the three CdSe/Au NC ratios studied. Inset: comparison of dark-currents at 296 K for the different mixtures.

The 78 K photo-conductivity decreased slightly and became non-linear for low Au NC population, and decreased even more dramatically for the higher Au to CdSe NC ratio. The non-linearity seems reasonable because the Au NCs, being metallic, are highly polarizable, and the local fields around the CdSe NCs most likely did not increase linearly with bias during a voltage sweep.

The most striking result from this study of CdSe + Au NC mixtures is that the room-temperature photo-current was increased significantly by including a small concentration of Au NCs. Quenched photo-luminescence has been reported for Au + CdSe NC binary arrays.^[82] This suggests that excitons which form upon illumination of the film tend to not recombine radiatively. The results of increased room-temperature photo-currents described in this section is likely to be a direct consequence of this different charge dynamic compared to CdSe-only NC arrays. The history effects at the lower temperatures suggest that there are charge traps in the film, though the overall trend of increasing photo-current with decreasing temperature indicates that photo-conduction is still dominated by recombination dynamics.^[59,62] It is interesting that the enhancement of the photo-current gets lost as the device is cooled (c.f., Figure 5.10). Combined with the current-reducing effect of history at the lower temperatures, these trends suggest that charge traps may begin become more important as the temperature is reduced. It is possible that the traps are at the CdSe NC - Au NC interface and that the effective trap depth changes with temperature: a possible consequence of the change in local field contribution made by the Au NCs at different temperatures. These observations are consistent with extreme reduction of the photo-current seen in the higher Au:CdSe NC ratio studies. In particular, this temperature dependent trap interface picture may explain why the photo-current decreases with decreasing temperature in that system. The exact mechanisms involved are not completely understood at the present time and further studies are needed.

5.4 CdSe NRs

Transport in arrays of TOPO-capped 6nm diameter CdSe NRs, with length of 22 and 31 nm, were studied in the dark and under photo-excitation at temperatures ranging from 78 K to 296 K. A typical device in this study is shown in Figure 5.11. The gap is $600 \times 230 \text{ nm}^2$ and filled a thin layer of $6 \times 31 \text{ nm}^2$ CdSe NRs, achieved by drop-casting 1 μL of NRs in a toluene-butyl ether solution (concentration $\sim 3.0 \times 10^{-8} \text{ mol/L}$). NRs cover the substrate relatively homogenously, approximately forming a monolayer. Unlike for the CdSe NCs, the imaging contrast in the TEM for these NRs is high enough to obtain clear images of a single layer. The NR film does not exhibit extended voids and shows some regions where a second layer of NRs starts to form. The overall orientation of the NRs is isotropic and no preferred current pathway within the gap region is evident.

Figure 5.12 shows dark-current data taken at room temperature for the device shown in Figure 5.11. In general, these NRs had at least 50 times higher room temperature dark-conductivity than the CdSe spheres (NCs) and approximately 5 times higher than the CdSe + Au NC mixtures. In contrast to the bare device, shown in the figure for reference, the monolayer of CdSe NRs gave a dark current of $\sim 4 \text{ pA}$, for a 4 V bias applied across the gap.

Distinct from the CdSe NCs, which displayed typical *I-V* hysteresis (c.f., Figure 5.1) these NRs displayed an inverted behavior, where the dark-current was *higher* in the return voltage sweep compared to the forward sweep. The direction of the voltage sweep is indicated with arrows in the figure. The sweep rate in this measurement was 40mV/s. This behavior suggests that the NR film conductivity increases with time. In fact, measurements at fixed voltage showed that the current initially increases and then begins to decrease. An example of this behavior is shown in the inset. In this measurement, the voltage was ramped from 0 V to 1 V and the current was measured as a function of time. While the voltage was held constant at 1 V, the current continued to increase, exponentially, reaching a peak value of over twice the

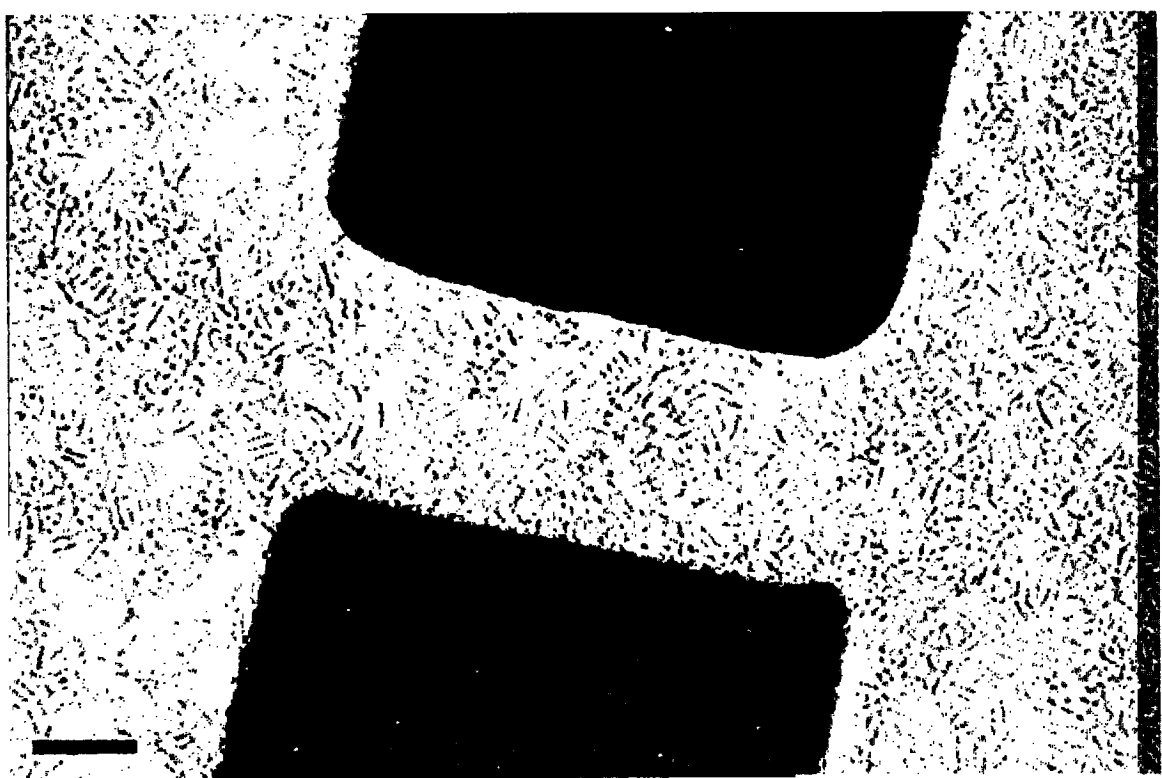


Figure 5.11: TEM image of 6×22 nm 2 CdSe NRs spanning a 600×230 nm 2 electrode gap with approximate monolayer coverage.

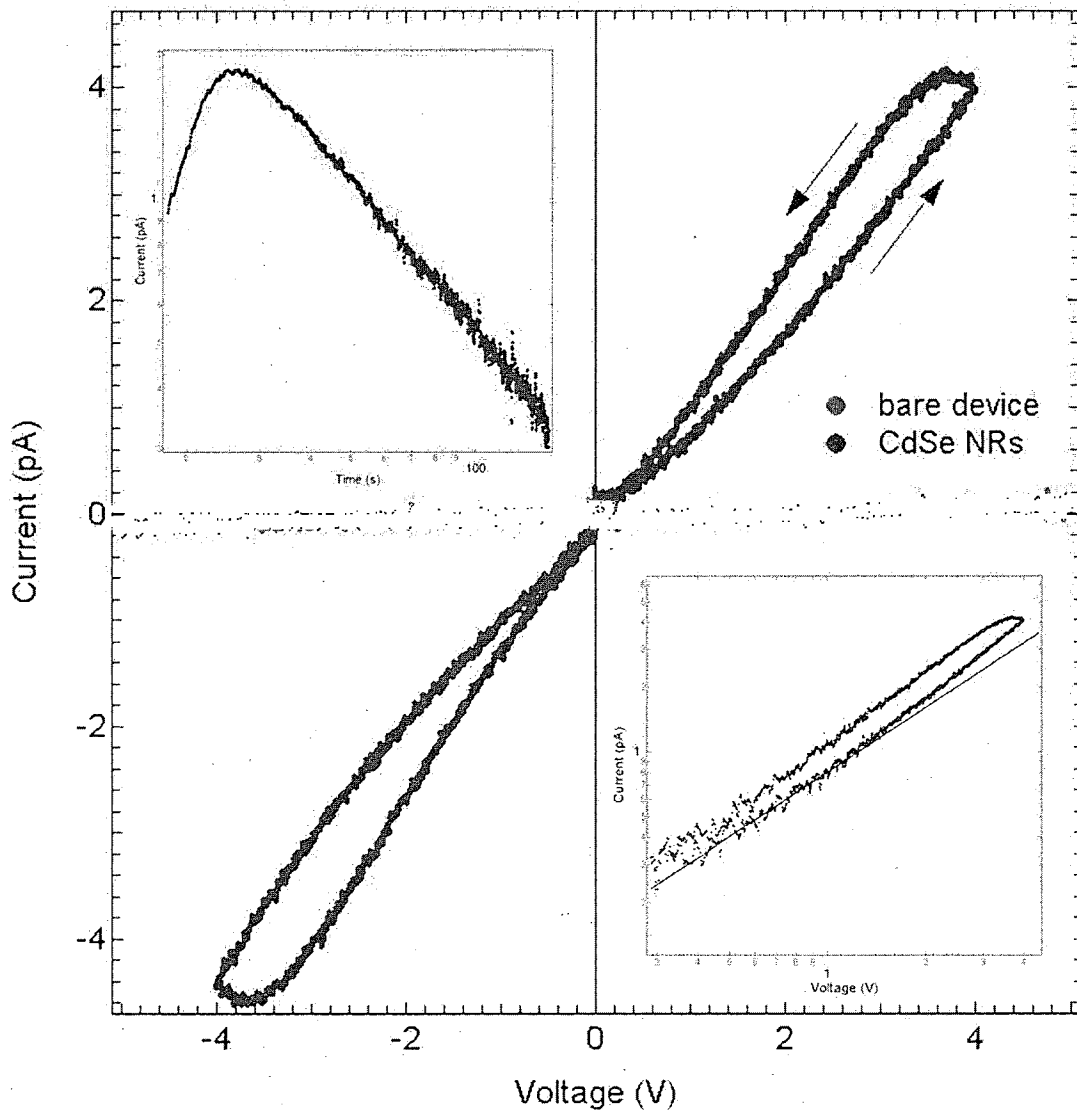


Figure 5.12: I-V characteristic of the $6 \times 22 \text{ nm}^2$ NR device shown in Figure 5.11, taken at room temperature. The bare device current is shown for reference. The voltage sweep directions are indicated by the arrows. Inset (upper left): log-scale plot of the time-dependence of the current at 1 V bias voltage. Inset (lower right): Log-scale plot of the I-V curve showing linear behavior below ~ 1.5 V (reference dark line corresponds to linear behavior).

initial value after roughly 10 s, at which point it began to decay as a power-law in time, i.e., $I \sim t^{-\alpha}$, where $\alpha \sim 1.3$.

At low bias the I - V curves are linear (see inset) for both the forward and return voltage sweeps. Using the device dimensions and known monolayer thickness, the resistivities in the Ohmic regime are estimated from the data to be $\sim 1.9 \times 10^4 \Omega \cdot \text{m}$ and $\sim 1.4 \times 10^4 \Omega \cdot \text{m}$ for the forward and reverse voltage sweeps, respectively.

Figure 5.14 shows I - V s taken in the dark in the temperature range 200 to 272 K, for a different device, shown in Figure 5.13, that also contained $6 \times 31 \text{ nm}^2$ CdSe NRs.

The voltage sweep rate was 100 mV/s for each curve. Below 200 K, the dark-current changed minimally with temperature down to 77 K and these curves were excluded from the plot for clarity. Both the forward and return voltage sweep directions have been included in the figure to show the temperature dependent behavior of the hysteresis. As can be seen from the plots, both the dark-current magnitudes and amount of hysteresis decreased with decreasing temperature. The inset shows an Arrhenius plot of the temperature dependent zero-bias conductance, taken as the I - V curve slope in the linear regime of positive forward bias. Above 210 K, the temperature dependence is seen to be linear in this logarithmic plot against inverse temperature, suggesting that the population of mobile carriers in the NR film follows a Boltzmann distribution; a model of transport often called “activated hopping”. The slope of the line corresponds to the characteristic energy required for a carrier to be mobile in the film and is estimated from the data to be 397 meV for this temperature range. The abrupt change in the Arrhenius plot near 210 K suggests that a different characteristic energy dominates at temperatures below ~ 210 K, approximately 46 meV. At these lower temperatures, however, the signals were weak. The corresponding error in the conductance measurements make this value only a rough estimate and is insufficient to support an activated hopping picture in this temperature regime.

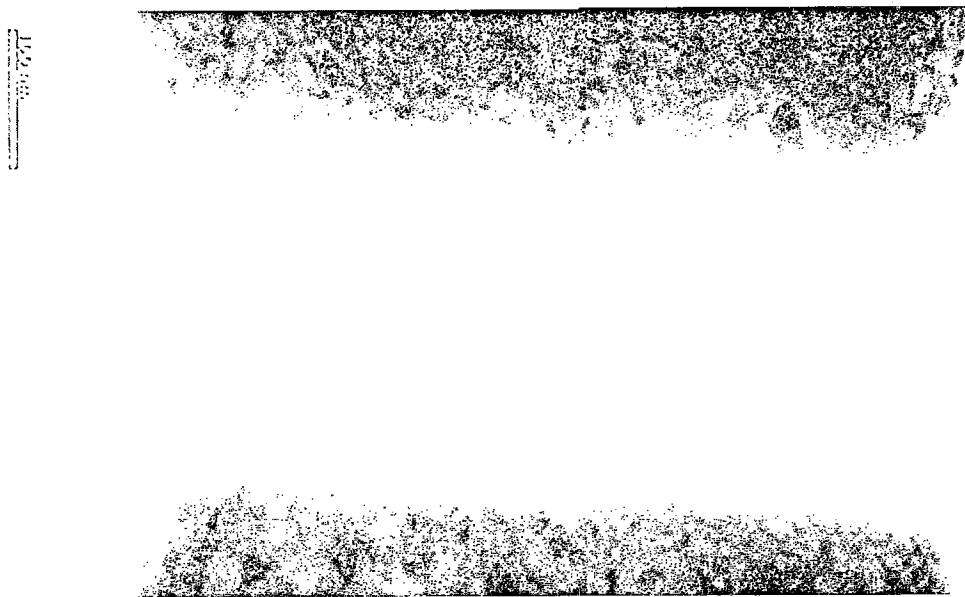


Figure 5.13: TEM image of $6 \times 22 \text{ nm}^2$ CdSe NRs filling an electrode gap used to obtain the temperature dependence plots shown in Figures 5.14 and 5.4. Scale bar is 100 nm.

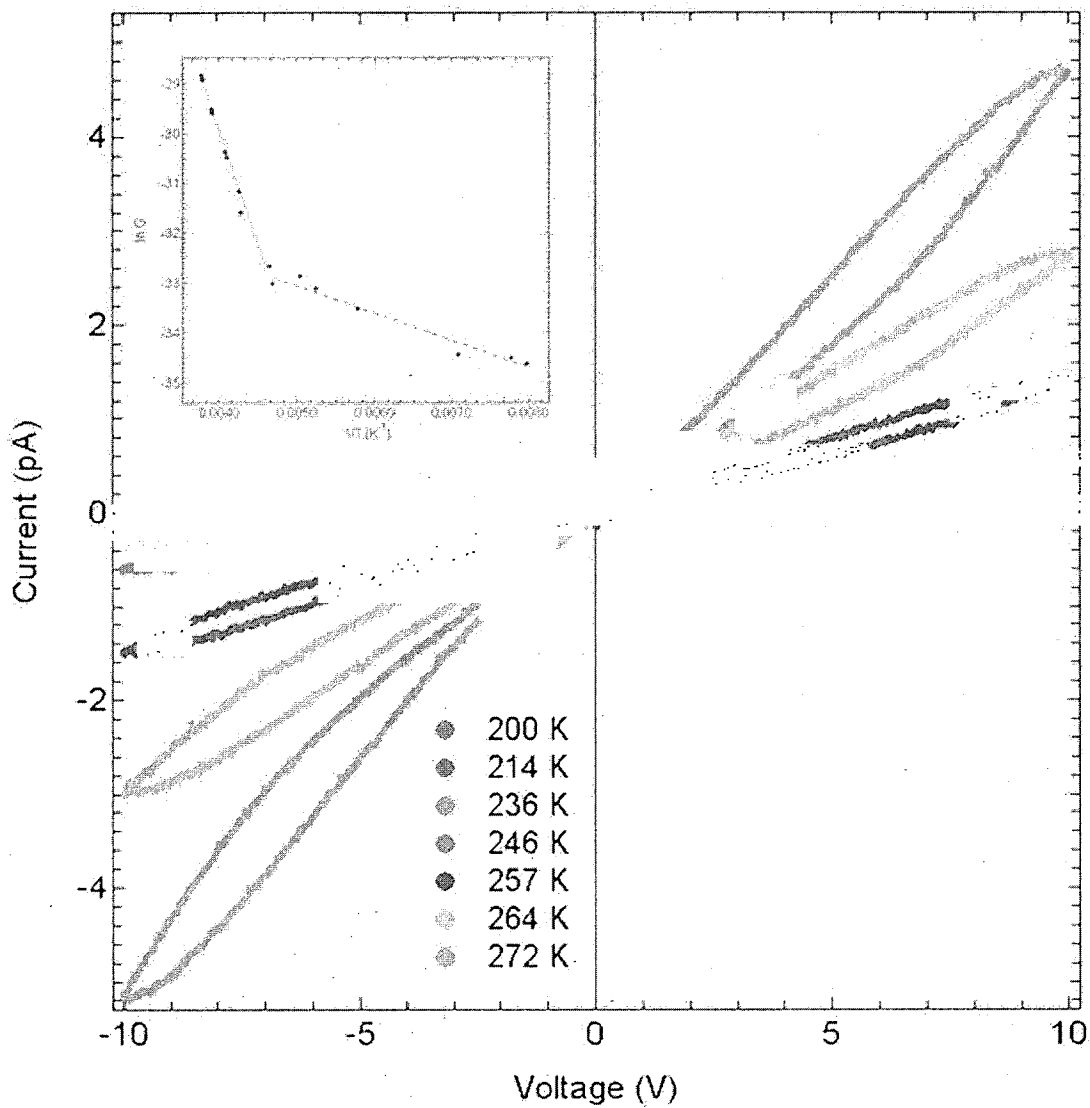


Figure 5.14: I-V characteristics of $6 \times 22 \text{ nm}^2$ CdSe NRs taken in the dark at temperatures ranging from 200 to 272 K. Inset: Arrhenius plot of the conductance showing two temperature regimes.

Another feature that distinguishes CdSe NRs from NCs is that photo-excitation does not increase their conductivity compared to measurements made in the dark. In fact, the NR film conductivity is even somewhat reduced by the photo-exposure. This behavior persists for lower temperatures as well. Figure 5.4 shows *I*-*V* characteristics for the device shown in Figure 5.13, taken between 238 and 280 K, under photo-excitation with the same 532 nm wavelength emission laser used to study CdSe NCs. Comparing to the dark-current measurements in Figure 5.14, it is evident that the current magnitudes are moderately reduced by the photo-exposure. Furthermore, in contrast to the CdSe NCs, the NR photo-current was observed to decrease with decreasing temperature. The corresponding Arrhenius plot (inset) shows that temperature dependence of the photo-current is similar to that of the dark-currents. An issue that complicates direct comparison with the dark-current data is that the hysteresis behavior of the photo-current is more complex. As seen in the figure, the forward and reverse voltage sweeps cross each other twice, making the *I*-*V* curves look like doubly twisted loops. This behavior persisted as the temperature was reduced, but became less pronounced.

Recently published results on CdSe NR transport measured in air with large, inter-digitated electrodes, reported similar current decays to those described here, though the decay was said to be irreversible.^[74] It is possible that the currents in the devices shown above also would have eventually decayed irreversibly if they had been measured for a long enough time, since the degree of exposure to oxidation is kept so much lower in the cryostat compared to ambient conditions. Overall, the extent of charge traps in CdSe NRs seems to play an important role in their transport behavior, whether induced by oxidation or as a result of conditions during synthesis. In fact, reports of a permanent dipole in CdSe NRs have led to a picture of individual NRs where the crystal orientation is not aligned with the long axis, leading to uncompensated charges at the NR surface.^[83] This picture of non-uniform surface charge may explain the initial dark-current increase, if the surface charge

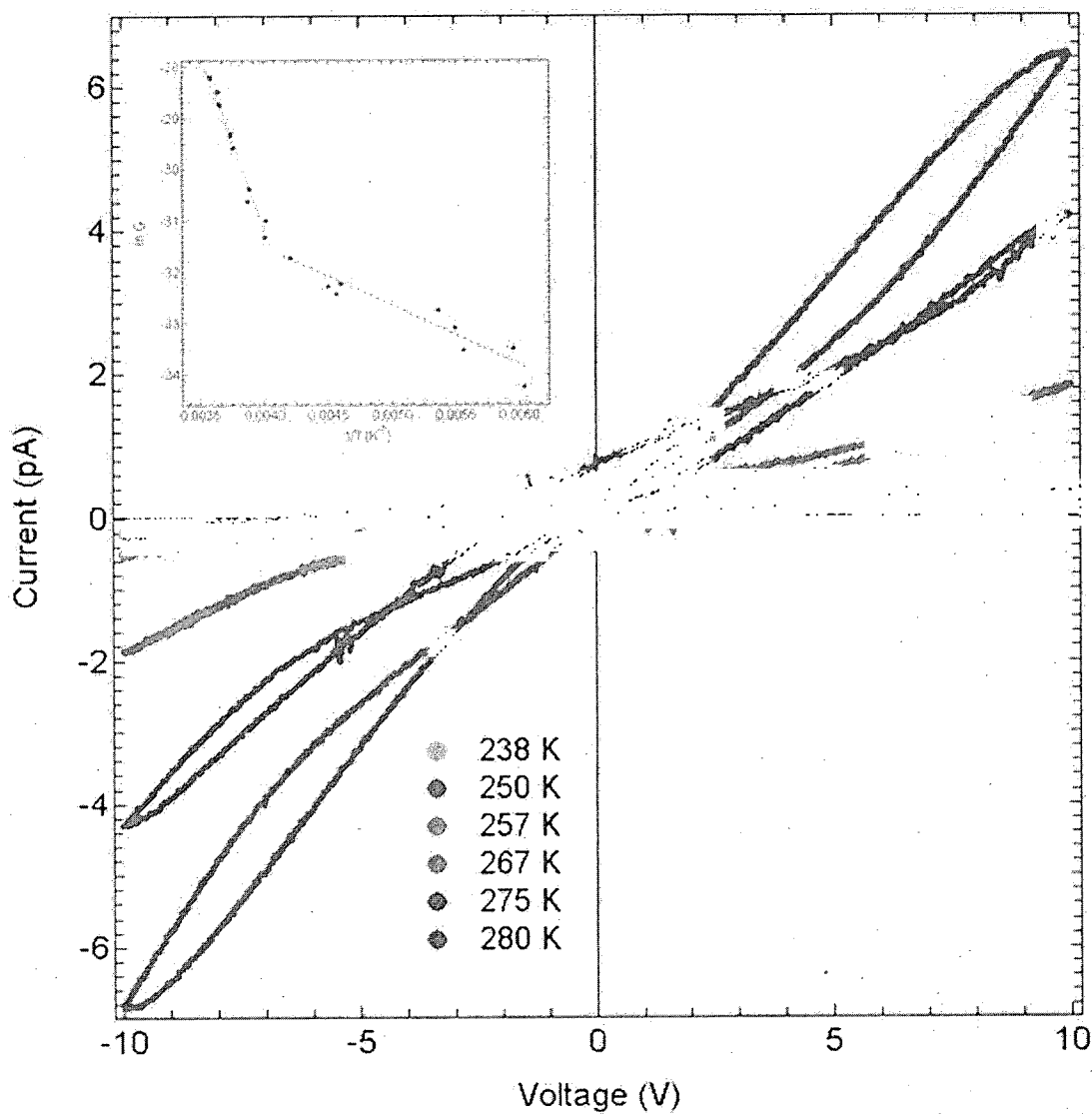


Figure 5.15: I-V characteristics of $6 \times 22 \text{ nm}^2$ CdSe NRs taken under photo-excitation at temperatures ranging from 238 to 280 K. Inset: Arrhenius plot of the conductance showing two temperature regimes.

gradually becomes compensated by mobile carriers accumulating at the NR. The current maximum and subsequent decrease would then follow if charges continue to accumulate on the NRs. It would be interesting if the direction of the current has an effect on the time-dependence, since a NR with a permanent electric dipole would clearly have a preferred direction for current flow. However, from the TEM images shown above, these films tend to be isotropic and any directional preference would be averaged out. Measurements on highly aligned NRs may therefore provide an opportunity to correlate time-dependence with the direction of current flow.

The presence of traps is also consistent with the lack of photo-current enhancement described above. In fact, the photo-current gains were less than one for these NRs, suggesting that photo-excitation may actually increase the amount of surface charges or traps. The measurements of positive photo-conductivity in the ambient intrepidity device study do not support this picture, but the total channel areas involved in the two device geometries make it difficult to compare directly. Studies of time-dependence and photo-current gain of NRs with varying length may serve to reveal the role of the dipole in NR transport. Controlled surface trap engineering may also allow for valuable control studies to be performed.

5.5 PbSe NCs

Figure 5.5 shows TEM images of a device containing six electrode gaps, each filled with 6.4 nm diameter PbSe NCs capped with oleic acid ligands (~ 2 nm). The PbSe NCs are distributed non-uniformly on the millimeter and micron scales; seen as the colorful structure in the optical image of the full chip and as the marble-like background in the TEM image of the full set of electrode gaps. Inside the electrode gaps, however, the NC distributions were relatively uniform and specific NC assembly cases could be studied. Figure 5.5(d) shows a zoom-in TEM image corresponding to one of the gaps, with 350 nm wide electrodes separated by 50 nm. Here PbSe NCs

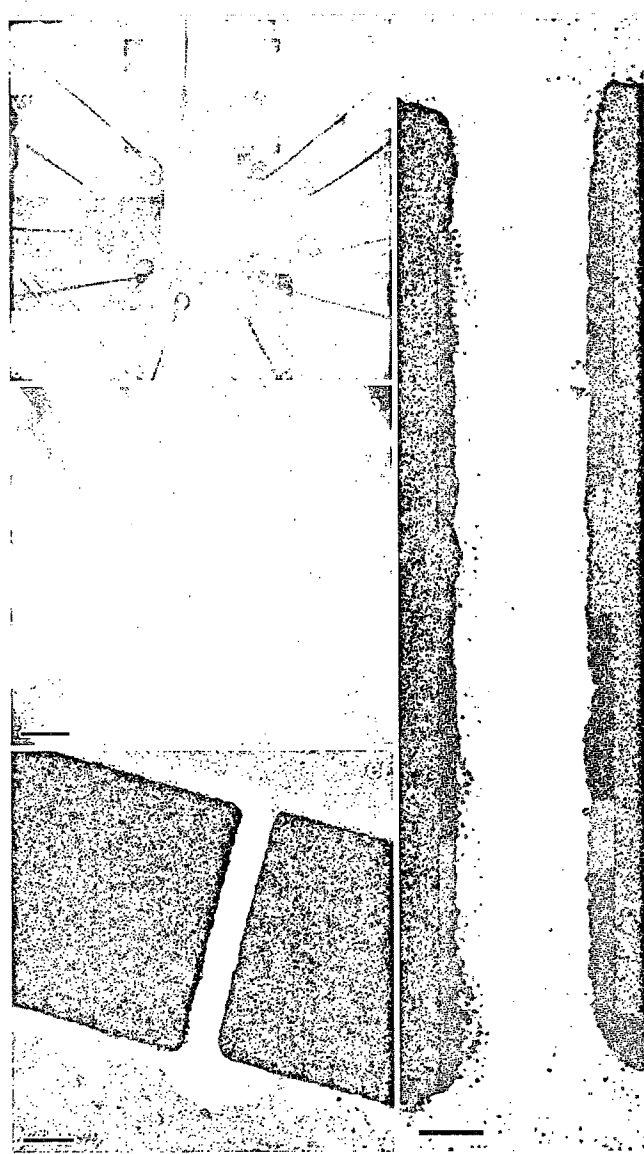


Figure 5.16: PbSe device shown at three scales: (a) optical image of the device surface (5 mm wide image). (b) TEM image of the electrodes on the window region. The non-uniform NC film looks like a marble structure in the background. (scale bar = 10 μm) (c) Image of gap in the lower right corner of (b). (scale bar = 200 nm) (d) Several TEM images pieced together to show the sub-monolayer of PbSe NCs spanning the gap. (image height corresponds to 1.2 μm)

can clearly be seen spanning the electrodes with sub-monolayer coverage and local triangular lattice order. Importantly, these TEM images show that there are many complete NC paths available for conduction, despite the sub-monolayer coverage. Furthermore, the contact of the electrodes to the PbSe NCs is good (c.f., Figure 5.11). However, this device and others corresponding to the same PbSe NC coverage did not show any measurable current for either the dark or photo-excited cases. Applied fields ranged up to $\sim 10^8 \text{ V/m}$, the approximate limit imposed by dielectric breakdown of the SiN_x layer. Optical characterization of these PbSe NCs showed a first absorption peak at 1743 nm and strong absorption for shorter wavelengths. The 630 and 532 nm laser light wavelengths used to photo-excite the samples therefore should have been sufficient to reveal any photo-currents.

To determine if thicker NC films were necessary to observe measurable currents, higher concentration solutions were also tested. Figure 5.5 show several electrode gaps, ranging in width from 530 to 565 nm and separation from 140 to 230 nm, each containing 6.4 nm diameter PbSe NCs highly ordered in 3-dimensions. Such “lattices of NCs” are often called “super-lattices”. Again, TEM imaging provided valuable evidence that these measured NC assemblies spanned the electrodes and were well coupled to them, eliminating the likelihood that the absence of current was due to insufficient contacting or breaks in the assembly. Furthermore, TEM imaging allowed for the distinction between different super-crystal types and domain structure. As with the sub-monolayer devices, however, these super-crystal devices also displayed no dark or photo-current.

Assuming that conduction in NC arrays is dependent on electron tunneling between nearest neighbor NCs, it is important to recognize that the NC-ligand-NC junction is a $\sim 2\text{-}4$ nm wide tunneling barrier in the case of oleic acid capped NCs. It was possible to reduce this barrier significantly by replacing the relatively long oleic-acid ligands with butane-dithiol (~ 1 nm) using a simple solution chemistry process. PbSe NCs capped with oleic acid were transferred into a solvent containing

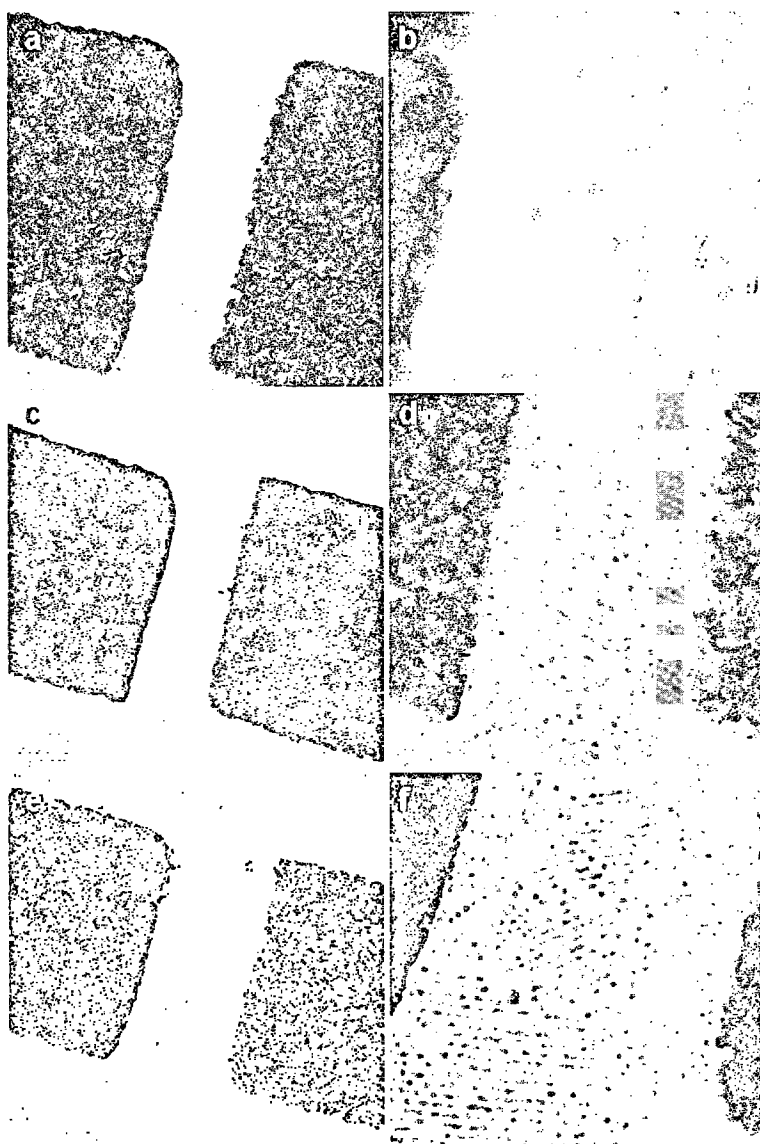


Figure 5.17: TEM images of PbSe NCs assembled into superlattices inside different electrode gaps. Each gap image (a,c,e) has a zoom-in to its right (b,d,f). (b) and (d) correspond to single domain super-crystals, while (f) consists of subdomains most likely because the assembly was disturbed by the debris seen as a dark spot. The debris was probably Au left over from fabrication. Scale bars are 100, 20, 200, 50, 200, 20 nm.

a high percentage of butane-dithiol and mixed briefly. The bond strengths between the PbSe NC surface and either of these two ligands being close in energy, entropic forces rapidly led to the comparatively few oleic acid ligands being replaced with abundant butane-dithiols.

Figure 5.5 shows an example of 6.4 nm diameter PbSe NCs that underwent exchange before being drop-cast onto a SiN_x device for *I-V* characterization. High-resolution TEM images revealed that the separation between NCs has been reduced from ~ 3 nm (c.f., Figure 5.5) to under 1 nm. In addition to the reduced NC spacing, the butane-dithiol ligands were able to enhance the coupling of NCs to the Au electrodes because of the high affinity of thiols to Au. Figures 5.5(c-d) show a device with 530 nm wide electrodes separated by 200 nm, filled with the ligand-exchanged PbSe NCs. The NCs are completely disordered in a several monolayer-thick film, but clearly span the electrodes and are well coupled to them. Surprisingly, this PbSe NC configuration still gave no measurable current signal during dark and photo-excitation conduction characterization.

In another attempt to measure currents in PbSe NCs, the electrode separation was reduced by an order of magnitude, down to the scale of individual NC diameters. Electrode gaps at the scale of 10 nm and below are often referred to as “nanogaps”. Techniques for achieving such small gaps are non-trivial and nanogap fabrication continues to be an active area of research in nanoscience. Two methods for fabricating nanogaps were developed while conducting the NC transport research discussed in this thesis and they are described in a separate chapter.

Figure 5.5(a) shows a TEM image of several 6.4 nm diameter oleic acid capped PbSe NCs localized in an 11 nm gap. The NCs were drop-cast from a heavily diluted hexane/octane (9:1) solution in order to avoid many NCs landing in the nanogap area. As a consequence, it was necessary to drop-cast multiple times before a measurable change in the current was detected, corresponding to successful incorporation of NCs into the gap.

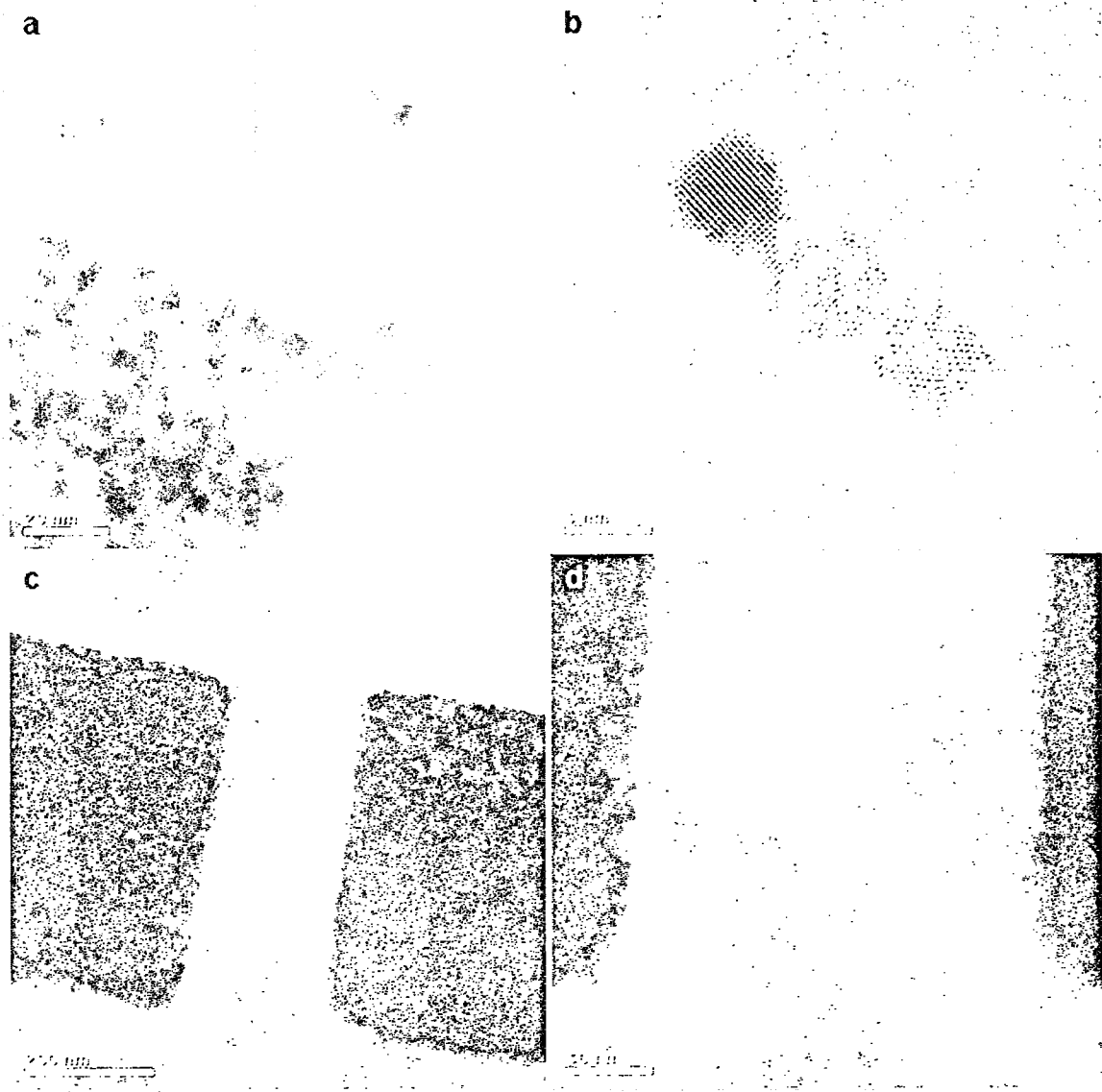


Figure 5.18: TEM images of PbSe NCs after ligand exchange from oleic acid to butylamine. (a) The NCs are packed together closely, but without much order. (b) High-resolution image showing three NCs close together. The inter-NC spacing is below 1 nm. (c) Butane-dithiol-treated NC assembly filling an electrode gap. No current was measurable, despite the reduction in NC separation. (d) Higher magnification image of the gap showing good contact to the electrodes and many complete paths between them. Scale bars are 20, 5, 200, 50 nm.

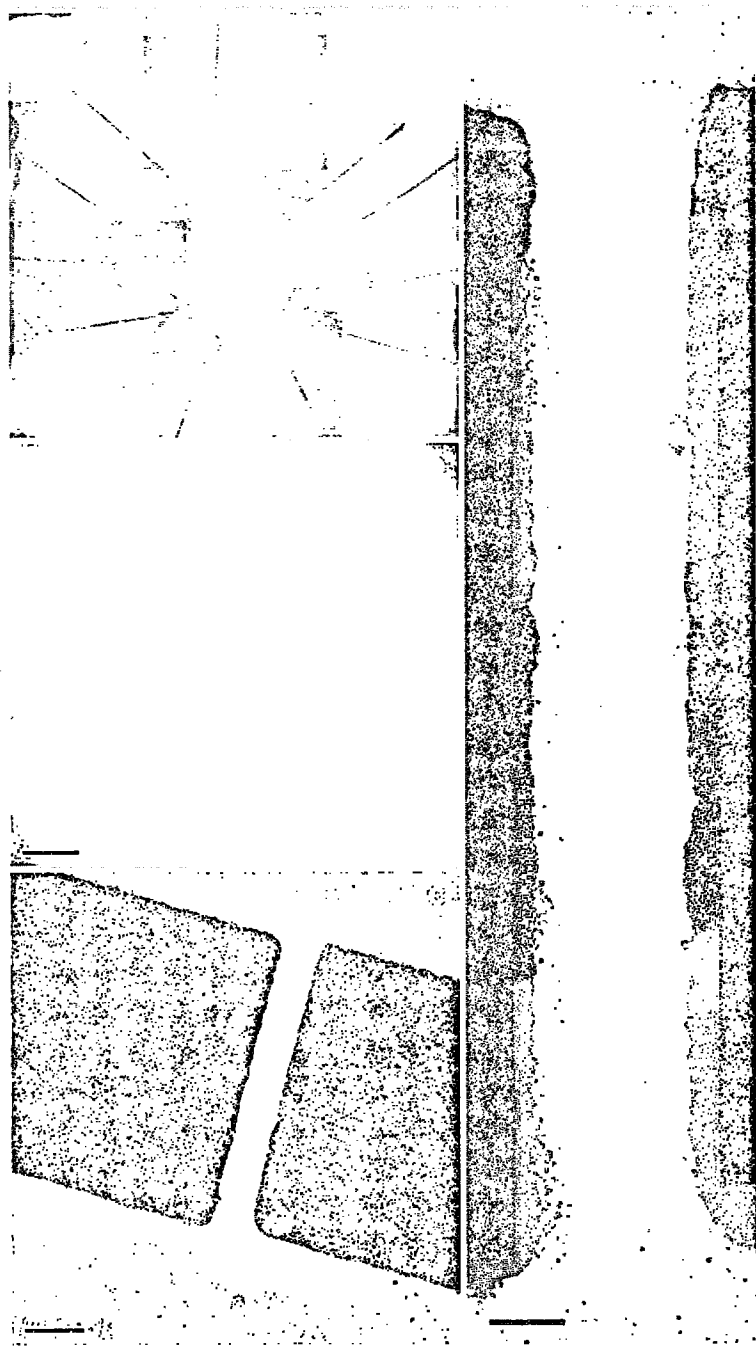


Figure 5.19: (a) TEM image of a small array of PbSe NCs inside of an 11 nm nanogap defined by two Au electrodes. (b) I-V characteristic at $T = 5$ K in high vacuum for the same device in a without NCs (red curve) and with NCs (black curve). The threshold voltage for positive forward bias is marked at 53 mV. A TEM image of the device before depositing NCs is also shown (inset, scale bar is 20 nm). (c) HRTEM image of the upper portion of the gap showing the detailed lattice structure of four PbSe NCs that dominate the charge transport across the gap. The scale bar is 2 nm.

Figure 5.5(b) shows an I - V characteristic, taken at 5 K with a 1 mV/s sweep rate, for the nanogap shown in Figure 5.5(a), before and after PbSe NC deposition. The current measured after imaging the bare gap (inset to Figure 5.5(b)) and before adding NCs is in the noise (< 30 fA). In contrast, the I - V curve for the added PbSe NCs shows a rich structure that was reproducible for each voltage sweep. In particular, there is a clear voltage threshold, $V_{th} \sim 53$ mV, for the transition from zero to finite current at positive forward bias. This corresponds to an electric field strength of $\sim 4.8 \times 10^3$ V/m, equivalent to a ~ 30 μ V drop across each NC, though the field is most likely non-uniform due to the electrodes tips each having ~ 10 nm radius of curvature, a dimension typical for atomic force probes.

Figure 5.5(c) is a HRTEM image focusing on the upper region of the gap area. It shows the detailed lattice structure of four closely packed PbSe NCs between two Au electrodes. From the image it is evident that only two NCs actually touch the contacts. From this and several other HRTEM images focusing on different parts of this device, this area was determined to be of primary interest. No other region of the nanogap contained NCs that completely bridged the two electrodes and were also close enough to each other for electron tunneling to occur between them. Inter-NC charging is approximated to cost an energy $E_c \approx e^2/2C$, where for a given NC radius, r , and inter-NC spacing, $2d$, the capacitance between neighboring NCs separated by a medium with dielectric constant, ϵ , is $C \sim 2\pi\epsilon r \ln\left(\frac{r+d}{d}\right)$.^[56] From the image, the NC diameter (~ 6.4 nm) and inter-NC spacings between NC nearest-neighbors (from 1 to 2.3 nm) were obtained. Using the dielectric constant of oleic acid ~ 2 , this gives a value $E_c = 56$ meV, which agrees very closely with the measured value for V_{th} .

That it was possible to measure current in this few-NC device suggests that the longer channel lengths in the ~ 100 nm gaps may have acted to suppress transport more than the NC spacing, possibly due to their being a high density of charge traps in the PbSe NC films. The NCs in Figure 5.5(d) are packed more closely than would be expected considering the ligand length, though the confined space in the

nanogap, combined with the influence of capillary forces during solvent evaporation and NC assembly may be responsible for the close packing. Compared to the sub-nm spacing for the case of butane-dithiol ligands, their spacing in the nanogap is still comparatively large. The measurable current signal in the nanogap device is most likely possible because of the minimal distance that carriers have to travel in the nanogap.

Chapter 6

Local Charge Transport in PbSe Nanocrystal Assemblies Studied by Correlated Electrostatic Force Microscopy and Transmission Electron Microscopy

6.1 Introduction

Conventional current-voltage (*I-V*) measurements on PbSe NCs have shown them to be highly resistive and it has not been possible to measure current, with or without photo-excitation, in electrode gap devices. However, *I-V* measurements only probe collective transport properties. Little information is revealed about the local transport behavior around features such as defects in the NC film assembly. By using a complimentary scanning probe technique, electrostatic force microscopy (EFM), it was possible to observe charge injection from the electrodes into the PbSe NC films with high spatial resolution. The charge dynamics were correlated with NC film structure imaged by standard atomic force microscopy (AFM). Measurement devices were made using the SiN_x membrane window platform, which allowed additional imaging by transmission electron microscopy (TEM) to be performed on the samples. As-deposited PbSe NC arrays were found to be insulating, consistent with

previous I - V characterization. Charge injection into the as-deposited NCs films was very slow and several hours were required for charge signals to become detectable. Mild annealing in a vacuum was found to improve the array ordering, to reduce the separation between NCs, and to dramatically enhance the conductivity of the arrays. Excellent correlation was demonstrated between local charging patterns in the annealed NC films and nanometer-scale variations in the complex NC film structure. The high resolution afforded by TEM made it possible to image individual NCs and precisely determine NC assembly order throughout the film.

6.2 Electrostatic Force Microscopy: Theoretical Description

Electrostatic force microscopy (EFM) is a technique developed on the basis of atomic force microscopy (AFM). AFM is able to obtain structural and force information of a sample by detecting interactions between a sharp tip and the sample surface. The tip is situated at the end of a cantilever that is mechanically coupled to a piezo. The piezo vibrates the cantilever at a frequency ω near its resonant frequency, ω_0 . The motion of the tip position is modeled as a driven oscillator:

$$\frac{d^2z}{dt^2} + \gamma \frac{dz}{dt} + \omega_0^2 z = \frac{F_0}{m_e} \cos(\omega t) \quad (6.1)$$

where z is the tip-sample separation, F_0 is the strength of the piezo driving force, γ is the damping factor, $m_e = k/\omega_0^2$ is the effective mass, and k is the spring constant. The solution is

$$z(t) = A(\omega) \cos(\omega t - \phi(\omega)) \quad (6.2)$$

where

$$A(\omega) = \frac{F_0}{m_e} \frac{1}{\sqrt{(\omega_0^2 - \omega^2)^2 + \gamma^2 \omega^2}} \quad (6.3)$$

$$\phi(\omega) = \tan^{-1} \left(\frac{\gamma \omega}{\omega_0^2 - \omega^2} \right) \quad (6.4)$$

If in addition to the piezo driving force, z -dependent force, $F(z)$, acts on the tip, the resonant frequency will shift because the cantilever effectively becomes stiffer (k increases). If the force is weak and the cantilever oscillation about its zero amplitude distance from the surface, z_0 , is small, the standard trick approach is to expand around z_0

$$F(z) \approx F(z_0) + z \frac{\partial F}{\partial z}(z_0) \quad (6.5)$$

and add this to the piezo driving force in Eq.(6.1). After minimal rearrangement this gives:

$$\frac{d^2z}{dt^2} + \gamma \frac{dz}{dt} + \left(\omega_0^2 - \frac{1}{m_e} \frac{\partial F}{\partial z}(z_0) \right) z = \frac{F_0}{m_e} \cos(\omega t) + \frac{F(z_0)}{m_e} \quad (6.6)$$

Neglecting the constant term, which only causes a constant offset, this equation is the same as Eq.(6.1) with a modified resonance frequency:

$$\omega' = \sqrt{\left(\omega_0^2 - \frac{1}{m_e} \frac{\partial F}{\partial z}(z_0) \right)} \approx \omega_0 \left(1 - \frac{1}{2k} \frac{\partial F}{\partial z}(z_0) \right) \quad (6.7)$$

Therefore, the resonance frequency of the cantilever is reduced for attractive forces by an amount proportional to the derivative of the force with respect to height from the surface.

The AFM feedback system can either be set to track the resonance frequency shifts:

$$\Delta\omega = -\frac{\omega_0}{2k} \frac{\partial F}{\partial z}(z_0) \quad (6.8)$$

or track the corresponding shift in the phase lag between the tapping drive force and the actual oscillation of the cantilever:

$$\Delta\phi = -\frac{Q}{k} \frac{\partial F}{\partial z}(z_0) \quad (6.9)$$

The two signals offer the same information about the tip-sample interactions. Both frequency and phase shift images are shown throughout this chapter.

Figure 6.1 shows a schematic of the EFM technique. EFM measurements involve scanning every line of the sample surface twice. The first scan is used to record the

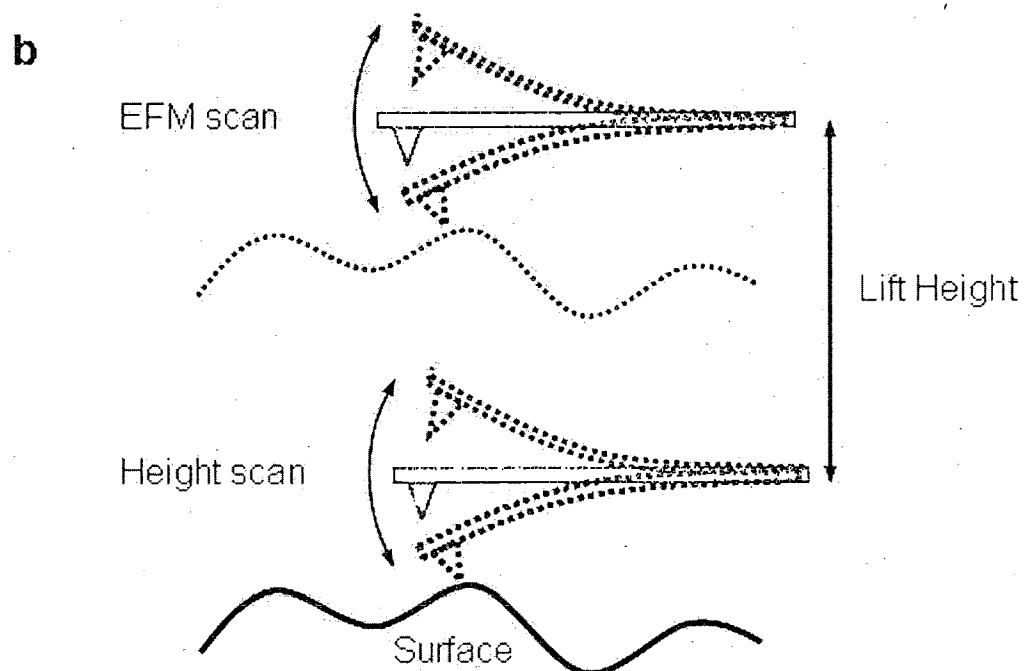
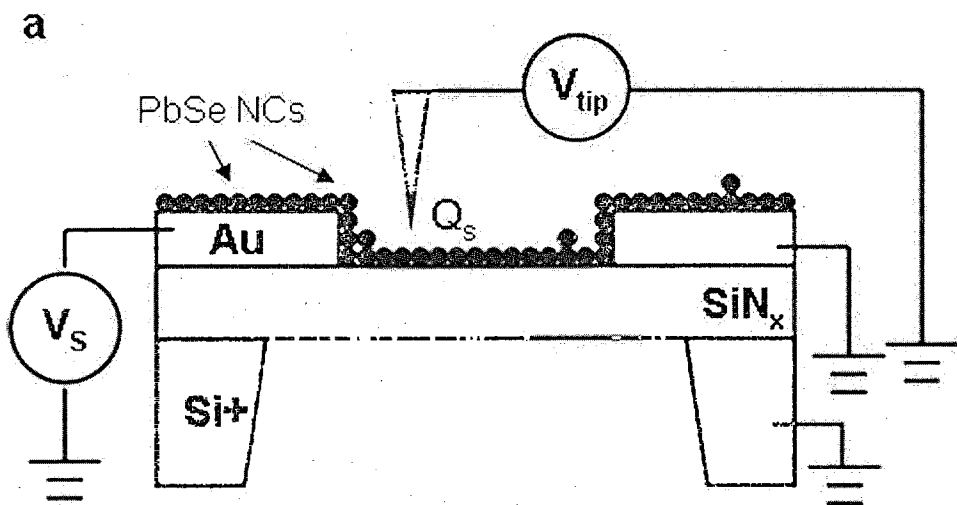


Figure 6.1: (a) Schematic of EFM imaging of NC arrays charged by electrodes. In this example, the right electrode is grounded. EFM measurements were also performed where voltages were applied to both electrodes. (b) Schematic of the double-scan sequence used to subtract contributions from height variations to the charge images

topography of the sample. During the second scan, the tip is lifted to a specified height (typically 10-30 nm in these measurements) and follows the height contour obtained in the first scan, thereby maintaining a fixed tip-surface distance. Having thus removed the contributions to the frequency/phase shifts due to variations of the surface height, this second scan can in principle sensitive only to longer-range forces acting on the tip. It is in this second scan that variations in charge and voltage in the NC films are imaged.

As shown in the cross-section in the figure, the measurement configuration involves a SiN_x device with PbSe NCs assembled between electrodes on the surface. The tip is conductive and therefore sensitive to local static charges, Q_s , and voltage biases, V . Specifically, the electrostatic force acting on the tip is:

$$F(z) = \frac{Q_s^2}{4\pi\epsilon z^2} + \frac{Q_s(CV)}{4\pi\epsilon z^2} + \left(\frac{dC}{dz}\right) \frac{V^2}{2} \quad (6.10)$$

where C is the capacitance between the tip and the environment. The first term is the Coulomb interaction between Q_s and the image charge that it induces in the tip (approximated to also be Q_s). The second term corresponds to the interaction between Q_s and charges present in the tip due to capacitive charging at finite V . The third term is purely due to capacitance. For the SiN_x , C is only non-zero when the tip is near any metal that is connected to ground (i.e., the electrodes and the Si+ outside of the window region). Therefore, when scanning over the window in regions away from the electrodes, the only contributions to the force are those from Q_s , i.e., charges in the NC film. V can be made non-zero either by applying a setting the tip and electrodes to different potentials. Corrections due to the workfunction difference between the tip and the electrodes also contribute to V , but these are on the order of $\sim \text{mV}$ and are insignificant compared to the voltages used in the measurements of PbSe NCs.

6.3 Experimental Details

The AFM used in this EFM study of PbSe NCs was a Veeco EnviroScope. The advantage of the EnviroScope is its environmentally controlled sample chamber, which allows samples to be kept under vacuum or inert gas flow. This is a valuable feature for PbSe NC research because their optical properties are known to degrade in ambient conditions. Additional capabilities include sample stage heating and compatibility with auxiliary electrical feed-throughs for applying voltages to device electrodes. Figure 6.2 shows a picture of the sample stage, modified slightly to allow measurement devices to be easily wired to the electrical feed-throughs. Voltages were applied to device electrodes with a LabVIEW controlled Yokogawa DC power supply connected through a BNC breakout box to a socket on the back of the AFM sample chamber. Devices were wire bonded to terminals on the stage which were themselves wired to a PCB insert that plugged into the AFM socket. Standard *I-V* measurements could be performed, but leakage currents ($\sim 10^{11} \Omega$) in the AFM hardware made low-level ($\sim 20 \text{ pA}$) current measurements impossible. The use of SiN_x window devices served to eliminate undesirable contributions to the EFM signals, such as screening of the sample by the Si substrate and effects caused by charges typically located at the dielectric/Si interface.

PbSe NCs with $\sim 2 \text{ nm}$ oleic acid capping were drop-cast from a diluted 9:1 hexane/octane solvent onto the device. Two sizes of PbSe NCs were studied with EFM; their diameters were 3.5 nm and 6.8 nm ($\sim 5\%$ size dispersion). Immediately after drop-casting the NCs, devices were placed into the EFM measurement chamber which was then quickly evacuated to pressures $\sim 10^{-5} \text{ Torr}$. Exposure of NCs to air was kept under $\sim 2 \text{ min}$, which was sufficiently short to avoid oxidation or degradation of the NCs. As-deposited PbSe NC arrays were first imaged with EFM and subsequently annealed at temperatures up to 150 C, either under vacuum or N_2 gas. After slowly cooling to room temperature, EFM studies were carried out for a range of voltages applied to device electrodes. Samples were imaged with TEM after

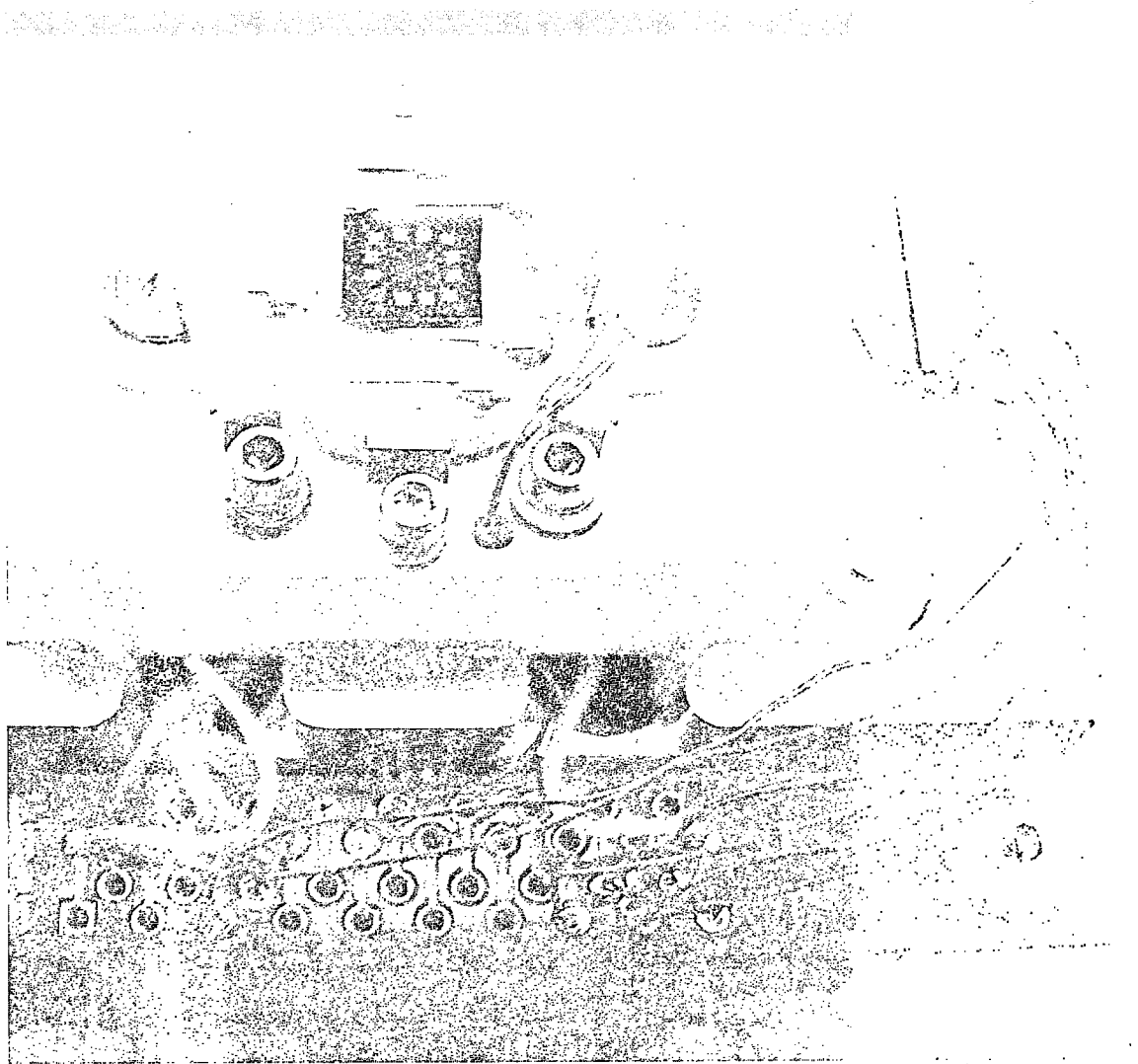


Figure 6.2: Photo of the stage used for EFM measurements with a 5×5 mm² SiN_x device wired up.

the EFM measurements were completed.

6.4 Background measurements

Figure 6.3(a) shows an AFM height image of an electrode gap, with $1.5 \mu\text{m}$ separation and 500 nm tapered width. It was preferable to use this size gap because of the larger area available for EFM imaging. Figure 6.3(b) shows a frequency shift map (EFM image) of the same area, with -10 V on the lower electrode, taken at 35 nm lift height. The upper electrode and tip were grounded during the scan. Although this region is over the suspended membrane (window) region of the chip, it is worth noting that the Si outside the window region was grounded during all of the EFM measurements. The EFM image in Figure 6.3(b) was taken after the -10 V had been applied continuously for ~ 16 hours, to determine if charging of the SiN_x would have any significant contribution to the EFM signals. By comparison with an EFM image taken at the beginning of the voltage application (Figure 6.3(d)), it was confirmed that SiN_x charging was negligible and would therefore not contribute to measurements of the PbSe NCs. Figure 6.3(c) shows an EFM image corresponding to the upper and lower electrodes at 0 V (i.e., grounded). The scale (0.1 Hz) in this image is much lower than for the -10 V images (30 Hz), demonstrating that the structure observed in Figure 6.3(c) is truly due to tip-sample voltage differences and that system noise is very low.

6.5 Results

As-deposited PbSe NCs were very insulating and charging from electrodes was very slow, requiring many hours for the EFM signal to develop in the NC film. Figure 6.4(a) shows the surface topography of a device in the region of an electrode gap, with narrow ends ($\sim 30 \text{ nm}$) and 800 nm separation, after drop-casting 3.4 nm diameter

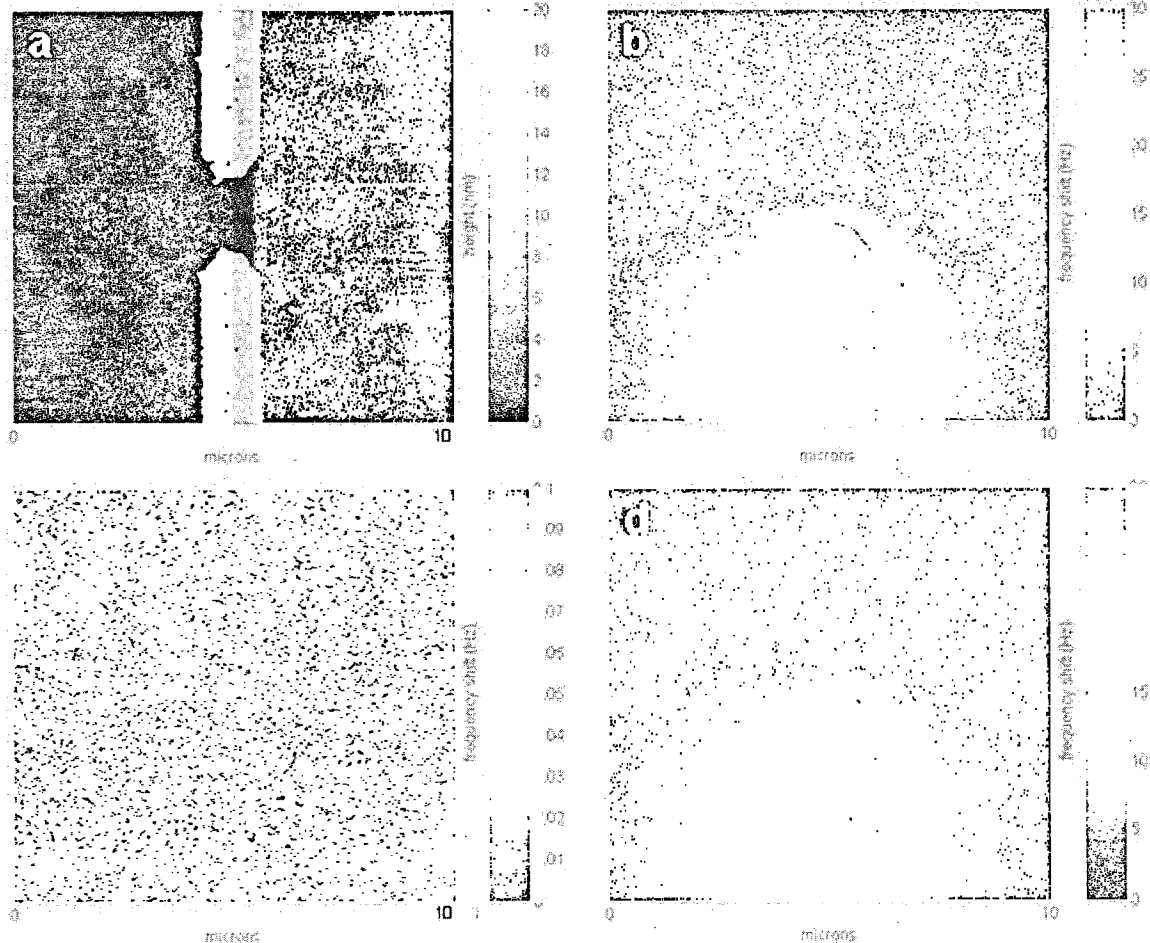


Figure 6.3: (a) Height scan of a bare electrode gap device (i.e., before depositing NCs). (b) EFM (frequency) image of the gap corresponding to -10 V applied to the lower electrode. The voltage was applied for 16 hours to image the effect of charging the substrate. Comparison with (d), the EFM image of the gap at the beginning of the voltage application, shows that the substrate does not charge noticeably. (c) An EFM image taken of the same gap corresponding to both electrodes grounded showing that signal noise is low.

PbSe NCs from a hexane/octane (9:1) solvent. The film was allowed to dry in an inert N₂ gas environment overnight with the electrodes grounded before imaging. The images were acquired with a highly doped Si “super-sharp” tip (radius of curvature ~5 nm). Figure 6.4(b) shows a zoomed-in height scan of the area directly between the two electrodes where individual NCs can be seen. Their width is exaggerated by about 20 nm due to the finite size of the tip. The NC film heights measured in the images correspond to approximately 5 NC layers. EFM signals obtained shortly after applying a voltage to the upper electrode looked no different than for the bare device. For this reason, voltages were applied for a significant amount of time before imaging with EFM. Figure 6.4(b,d) show EFM (phase) images corresponding to the two height scans. Prior to taking these images, a bias of -6 V had been applied to the upper electrode for ~16 hours to charge the film. The images were acquired immediately after setting the electrode back to 0 V. That the NC film is charged is evident because the upper electrode only appears due the contrast between its null EFM signal and that of the NC film. The film charge contours roughly follow equipotential lines between the two electrodes. The charge gradient can be seen clearly in the zoom-in image corresponding to the middle of the gap region. The NC film charge decayed very slowly and could still be seen in EFM scans after 16 hours, the duration of the charging period. This asymmetric behavior demonstrates that some charges become trapped in the film.

Mild annealing had a significant effect on both the structure and conductivity of the NC film. Figure 6.5(a) shows a device, where again 3.5 nm diameter PbSe NCs were drop-cast. In this case the electrode gap was 700 nm wide and 800 nm across. The as-deposited NC film was amorphous even after it was allowed to dry for several hours and detailed structure could not be resolved. However, resolution was sufficient to identify that the NC film completely filled the electrode gap. Figure 6.5(b) shows the corresponding EFM (phase) image for -6 V applied to the upper electrode. The EFM signal was indistinguishable from the bare device and there were

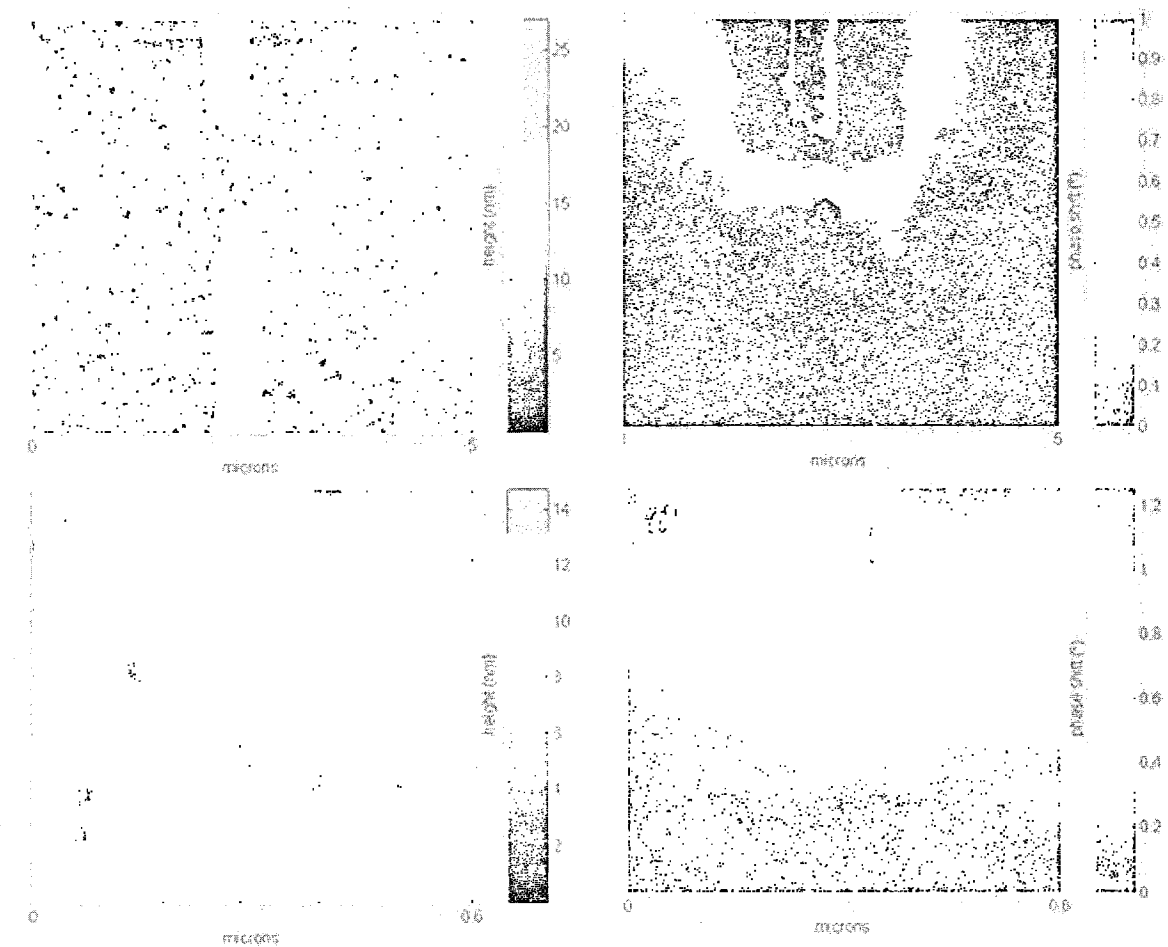


Figure 6.4: Height scans (a,c) taken of an unannealed film of 3.5nm diameter PbSe film across an electrode gap region of a device surface and corresponding EFM (phase) images (b,d) taken after charging the NC film by applying -6 V to the upper electrode for 16 hours, immediately after turning the voltage back to 0 V.

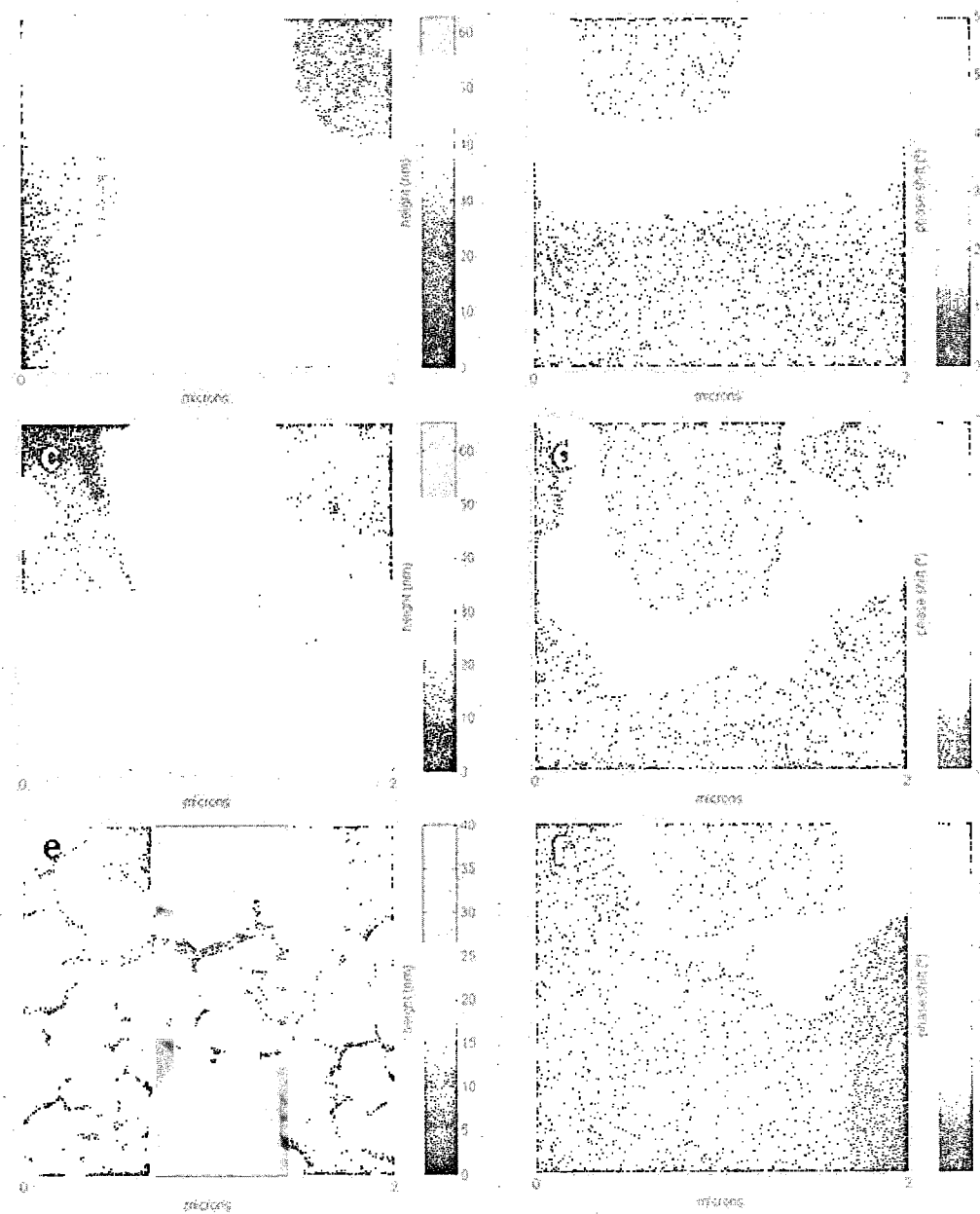


Figure 6.5: Height images of a 3.5 nm diameter PbSe NC film (a) before annealing, (c) after annealing at 100 C and (e) after annealing at 130 C. The corresponding EFM images for -6 V applied to the upper electrode are shown to the right of each height image (b, d, f).

no clear EFM features that correlate with NC film structure seen in the height image. Figure 6.5(c-f) show AFM images characterizing the effect of annealing on PbSe NC film structure and conductivity. Figure 6.5(c,d) show height and EFM images for the same electrode gap area from Figure 6.5(a,b) after annealing at 100 C for 3 hours in N₂ gas. As seen in the height image, the NC film became more structured, indicating that the NCs were mobilized during annealing. Furthermore, EFM scans revealed changes in the NC film charging behavior. Figure 6.5(d) shows an EFM scan taken immediately after applying -6 V to the upper electrode. Compared to the EFM results before annealing, the NC film rapidly became charged, most notably in the regions along the edges of the upper electrode, though a weaker charge signal can be seen extending away from the electrode.

Subsequent annealing at 130 C for 4 hours had an even more dramatic effect on both the NC distribution and film conductivity. The NC assembly underwent significant structural evolution and the film became largely discontinuous. As seen in Figure 6.5(e), the NCs clustered into densely packed regions separated by 10 to 100 nm-scale cracks. EFM scans revealed a corresponding change in the charging behavior. Similar to the 100 C case, applying -6 V to the upper electrode immediately charged the nearby NCs. In this case, however, the charge signal in the NC regions near the electrode was considerably stronger and more clearly correlated with the film topography, particularly near the right corner of the electrode. Interestingly, in contrast to the right half of the EFM image, the charge distribution in the left half was not as extended for the 130 C case, as it was for the 100 C case. Analysis of the surface topography suggests that this was caused by a film discontinuity that formed during the 130 C annealing that was able to block charge transport, though AFM resolution was insufficient to confirm this picture. However, correlated TEM imaging allowed for over an order of magnitude higher spatial resolution and the full role of film discontinuities was revealed.

Figure 6.6 shows detailed structure of the NC film in the proximity of the upper

electrode as imaged with TEM. The film cracks are seen much more clearly than was possible with AFM. Specifically, the NC film discontinuity around the left side of the electrode is seen to be completely devoid of NCs (Figures 6.6(c,e)), confirming the picture of charge propagation blocking by discontinuities. For image comparison, a zoom in AFM image is also shown in the of the discontinuity directly below the electrode. Clearly, the resolution is inferior to that obtained by TEM and the absence of NCs in the discontinuity could only be identified with TEM. In contrast to this, the TEM image shown in Figure 6.6(f) reveals some degree of connectivity between the NCs near the right corner of the electrode with NCs further away, consistent with the EFM structure observed in these regions.

Figure 6.7 shows additional height and EFM scans for this electrode gap at several magnifications. Figure 6.7(a) is zoomed out sufficiently to show some of the other electrode gaps on the surface, all of which were grounded throughout the measurements. The corresponding EFM image (Figure 6.7(b)) shows that the NC film charging pattern extended from the upper electrode all the way to the neighboring electrode pairs, each approximately $5 \mu\text{m}$ away. The electric field in the region between neighboring source electrodes is an order of magnitude lower than in the gap between a source and drain electrode pair. That the film charged more significantly in these weaker regions was a consequence of the many discontinuities in the NC film.

In addition to discontinuities, the varying number of NC layers throughout the film also influenced charging. As an example, the upper right quadrant of the EFM image shown in Figure 6.7(d) has a contour separating two large regions of 0.7 and 1.6 degrees (average). From analysis of the height image, it was found that this contour is correlated with the NC film thickness decreasing from 4 to 3 NC layers (average). Systematic analysis of EFM signal versus NC layer number was not possible because of spatially varying contributions from the electric field.

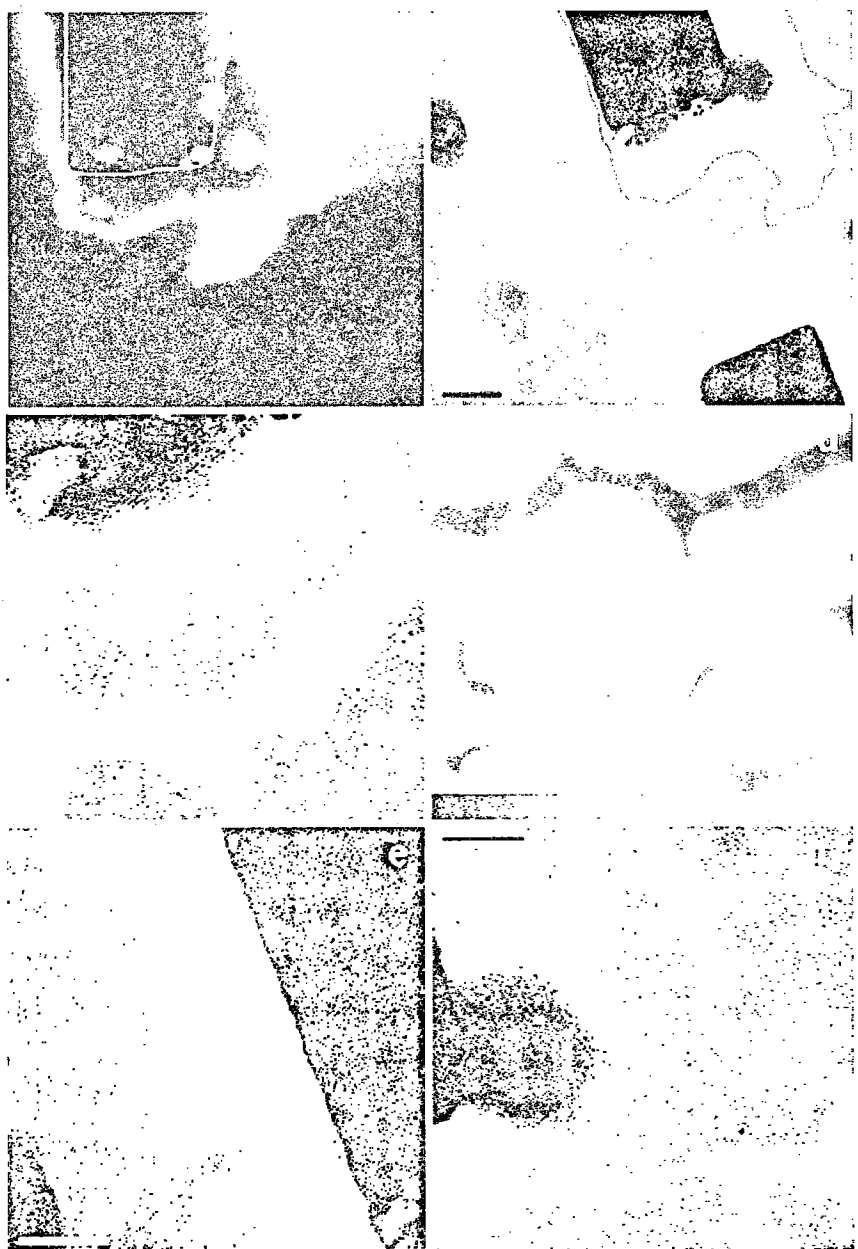


Figure 6.6: (a) EFM image of the upper electrode region for of the annealed PbSe NC film device, while -6 V was applied to the electrode and the other electrode was grounded. (b) TEM image of the discontinuities in the NC film. (c) Higher magnification image of a discontinuity of the film on the left side of the electrode in which no NCs An EFM were present. (d) High-resolution AFM image of the same discontinuity. The resolution of the AFM scan is inferior to that of the TEM and the NC population in the discontinuity cannot be assessed. (e) TEM image along the left side of the electrode showing a complete discontinuity, which correlates well with the absence of EFM signal on the left. (f) TEM image of the right side, where NC are seen partially populating a discontinuity.

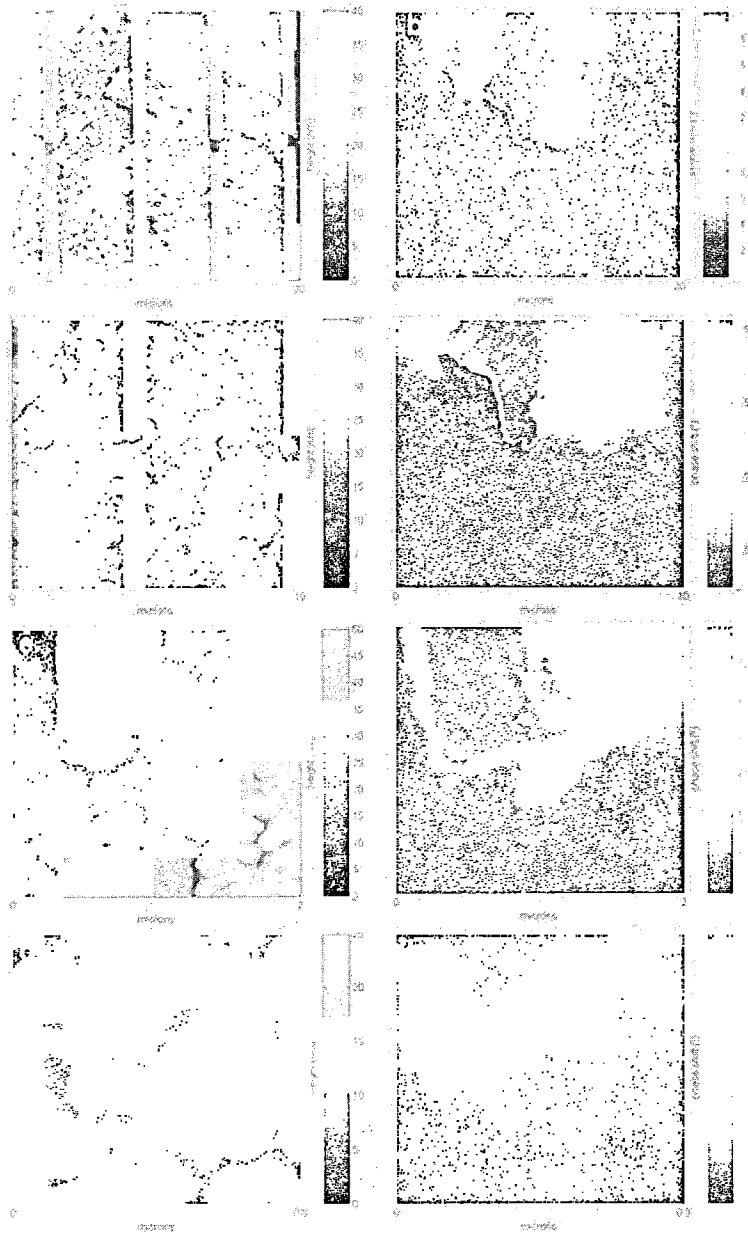


Figure 6.7: Height images at increasing magnification of the non-uniform annealed film of 3.5 nm diameter PbSe NC film distributed across the device surface (a,c,e,g). The corresponding EFM (phase) images for these scans are shown to the right (b,d,f,h). -6 V was applied to the upper electrode and the lower electrode was grounded.

6.6 Annealed 6.8 nm diameter PbSe superlattice networks

Figure 6.8(a) shows an AFM height scan of the electrode pair from Figure 6.3 after depositing 6.8 nm diameter PbSe NCs and annealing in vacuum at 130 C for ~12 hours. As seen in the image, the PbSe NC film ranges in thickness from roughly 1 to 4 NC layers and is highly structured. The solution used for drop-casting was roughly 10 times more dilute than for the devices shown in Figure 6.7 and Figure 6.5. TEM imaging of the device revealed that the NCs assembled into complex networks of superlattices (Figure 6.9).

Similar to the 3.5 nm diameter PbSe NCs devices, charge injection was very inefficient without annealing, while post-anneal measurements revealed significant increases in conductivity. Figure 6.8(b) shows the corresponding EFM (phase) image for this electrode gap, taken immediately after applying 5 V to the upper electrode and -5 V to the lower. Applying opposite polarities was useful for concentrating the electric field in the gap region. This measurement configuration achieves a 10 V drop across $\sim 1.5 \mu\text{m}$ ($\sim 7 \times 10^6 \text{ V/m}$) from the upper to lower electrode, compared to a 5 V drop across $10 \mu\text{m}$ ($\sim 5 \times 10^5 \text{ V/m}$) from these electrodes to neighboring grounded electrode pairs. The highly branched structure in the EFM image is well correlated with the cluster-network topography of the NC film seen in the height image. A clear example of structure correlation is shown for another region of the device in Figure 6.10, where charge has been injected into a NC network from the electrode at the bottom of the image.

6.7 Voltage Dependence

The extent of NC charging is dependent on the voltages applied to the electrodes. Figure 6.11 shows that EFM signals increase with increasing voltage magnitude.

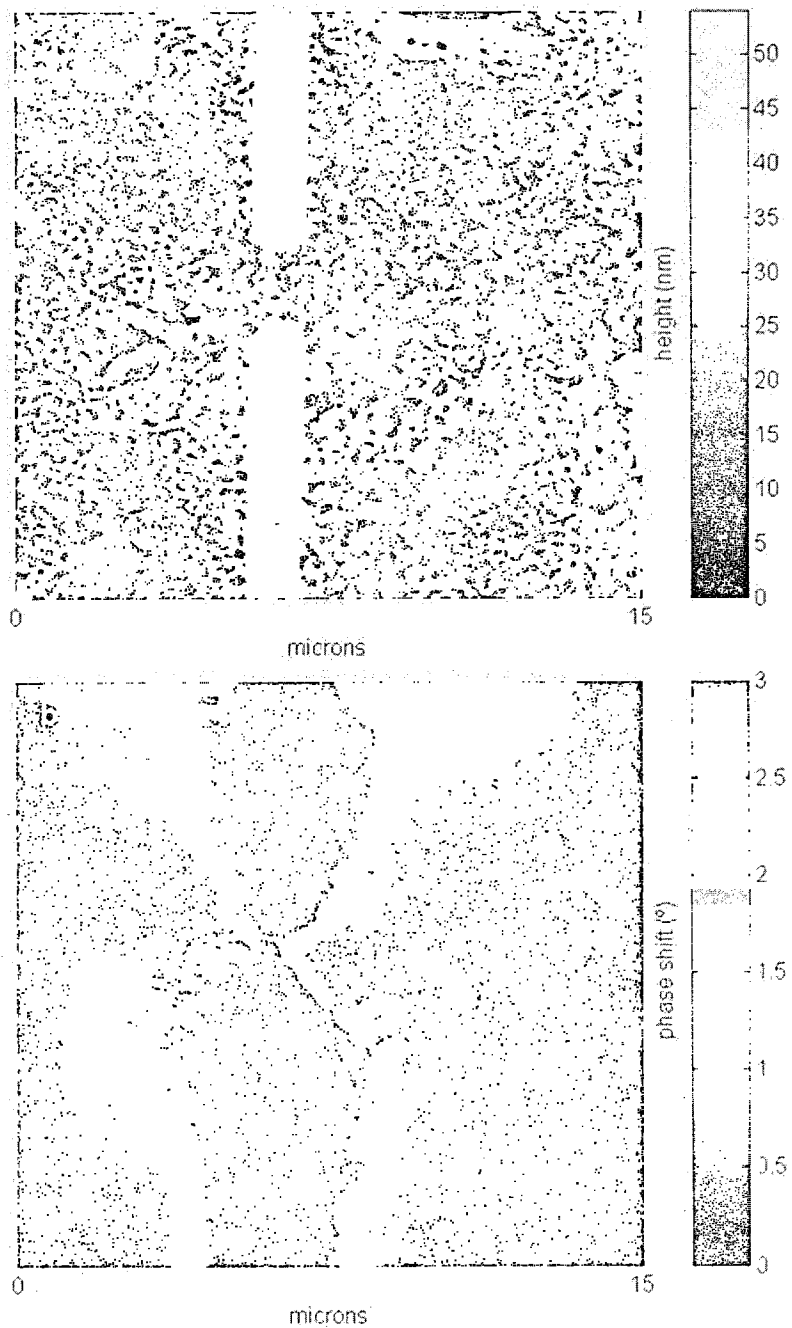


Figure 6.8: (a) Height image of an electrode gap with a non-uniform film of PbSe NCs distributed across the surface. (b) An EFM (phase) image taken of this gap corresponding to 5 V applied to the upper electrode and -5 V applied to the lower electrode.

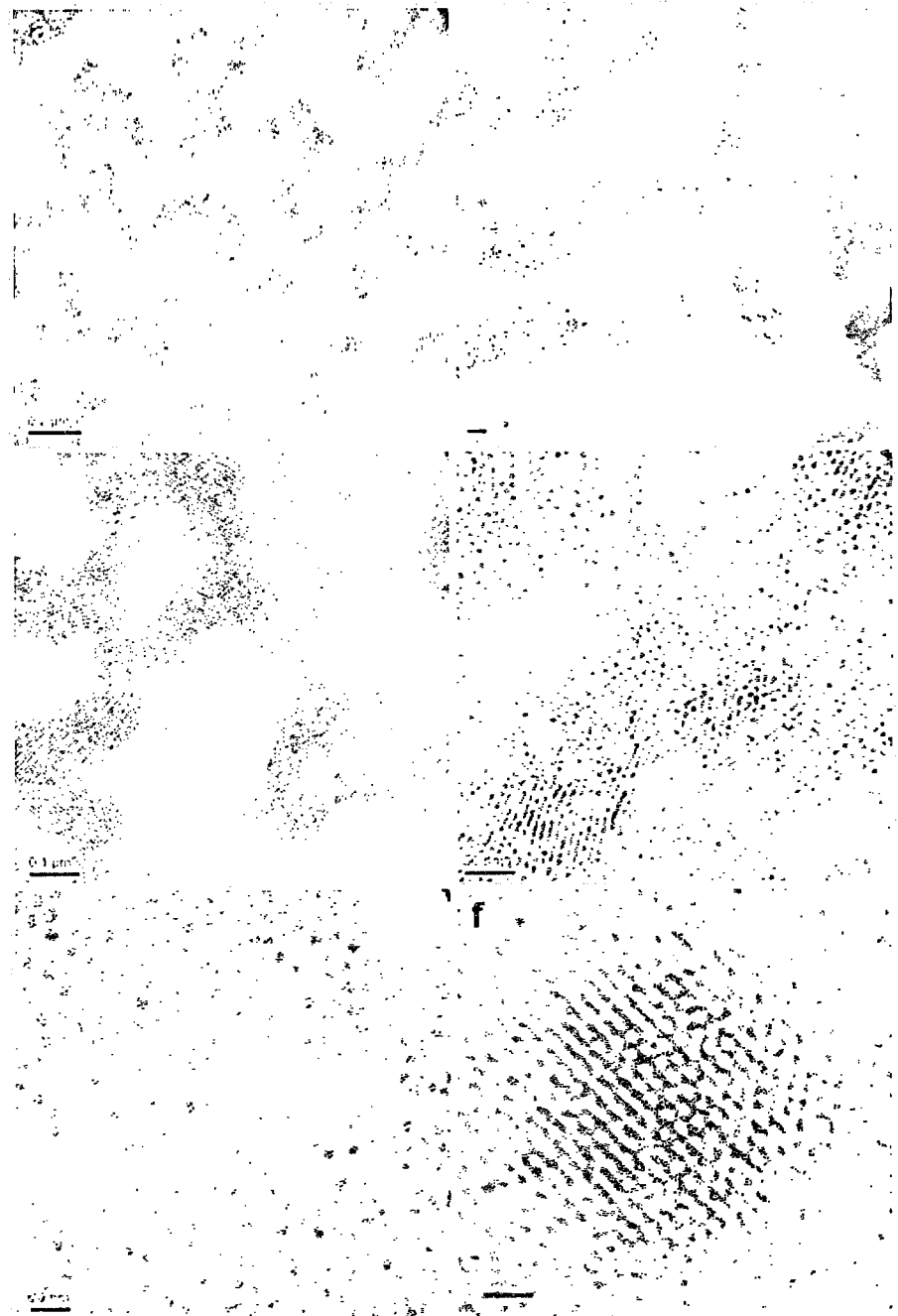


Figure 6.9: TEM images taken at increasing magnification of the PbSe NC superlattice network structure across the device. The scale bars in the images are 200, 50, 100, 50, 20, 2 nm for (a) through (f). The high-resolution TEM image shown in (f) reveals that the NC structure remained crystalline after annealing.

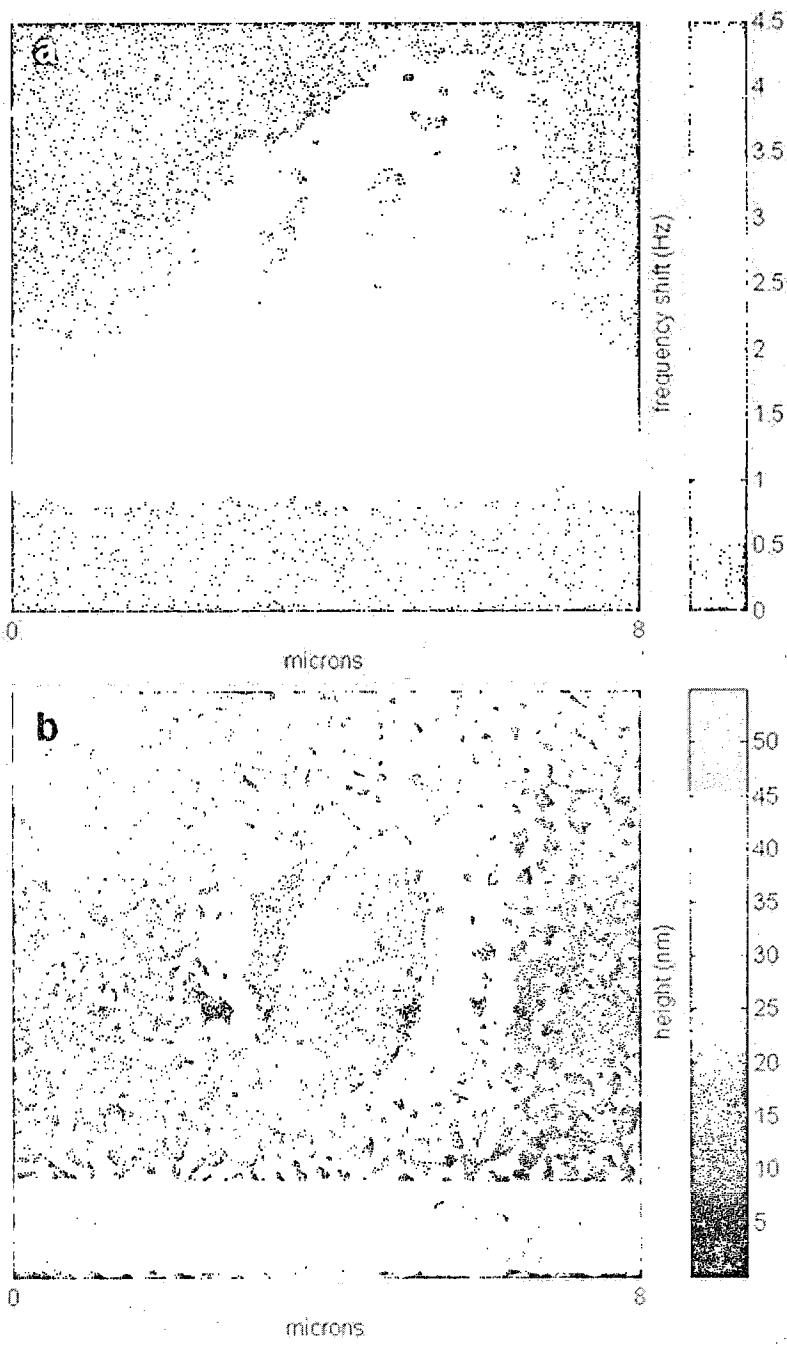


Figure 6.10: (a) EFM (frequency) image of 6.8 nm diameter PbSe NCs assembled in a complicated pattern, touching an electrode at -5 V. (b) The corresponding height image. Many of the NCs were not charged by the electrode, consistent with a picture of inefficient charge propagation through monolayers.

This series of images corresponds to the voltage magnitudes on the electrodes increasing from 0.5 V to 4 V , with the upper (lower) electrode at positive (negative) bias. In addition to increased signal magnitude, new EFM structure was seen to emerge as the increasing voltage caused charge to diffuse more deeply into the NC film. Even though the NC film is clearly able to take accommodate charge, the fact that the charge distribution is non-uniform and also spreads out for increased electrode voltage indicates that PbSe NC films do not behave like typical conductive materials. Specifically, its conductance is dependent on voltage, in contrast to Ohmic conductors. For instance, if the NC film behaved like an Ohmic conductor, then all regions connected to an electrode would be at the same potential and have the same EFM signal. Increasing the electrode voltage would increase this signal, but it would do so uniformly.

Additional evidence of the non-Ohmic properties of PbSe NC films was obtained by performing EFM measurements using a different voltage configuration. In this alternative configuration, the electrodes were grounded and a voltage was instead applied to the tip. If the NC film and its contact to the electrodes were Ohmic, then this measurement should yield similar EFM signals to those seen in Figure 6.11 because the tip would be able to induce image charges in the PbSe NC film. Put another way, the tip would feel a capacitive force when scanning over the NC film area, as if the NC film were just an extension of the electrodes. However, this voltage configuration resulted in EFM signals appearing only for the electrodes. Figure 6.12 compares (a) the EFM image corresponding to $\pm 4\text{ V}$ on the electrodes and the tip grounded with (b) the electrodes grounded and 4 V applied to the tip. The absence of any significant EFM signal from the NC film in the latter case is direct evidence that the NC film did not electrically couple the tip to the grounded electrodes. In other words, the tip experienced no capacitive force when scanning over the NC film regions and only the first term in Eq.(6.10) contributed significantly to the EFM signal.

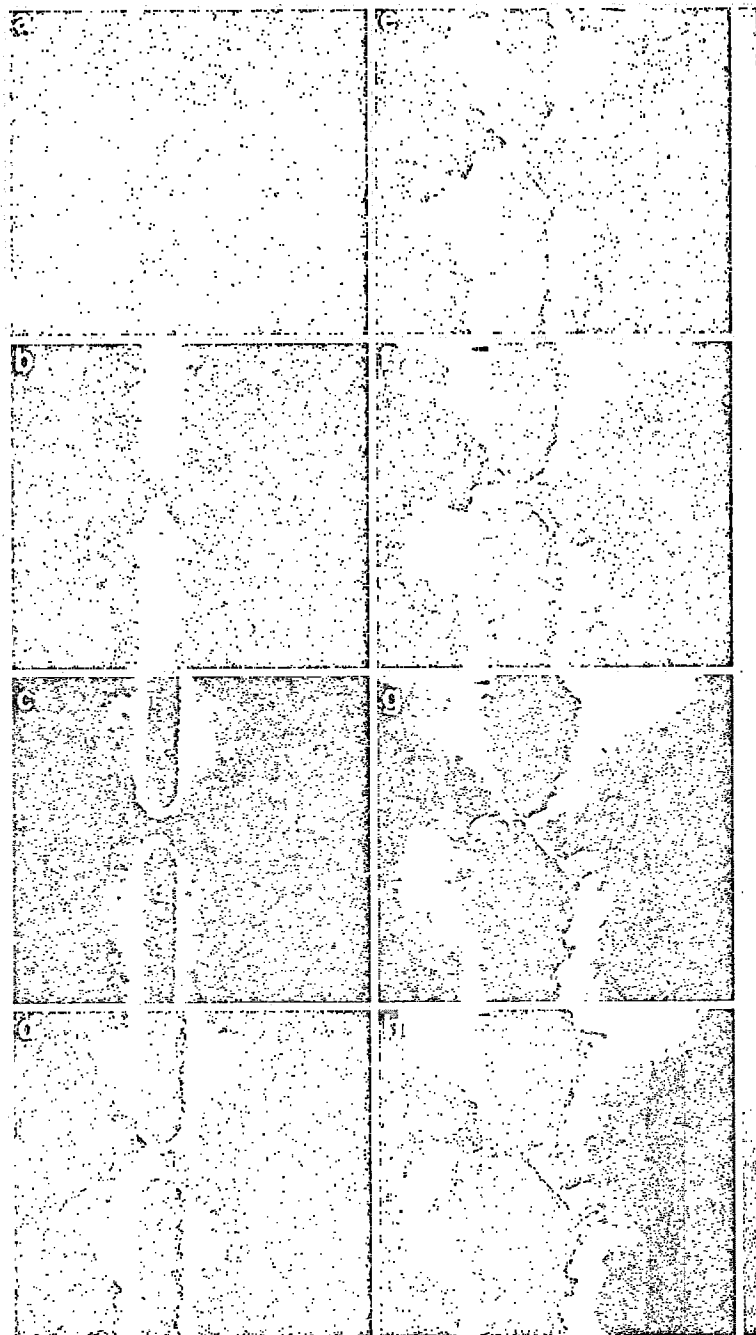


Figure 6.11: Voltage dependence of the charge distribution in the PbSe NC film. (a)-(h) Correspond to the voltage on the upper (lower) electrode increasing (decreasing) from 0.5 V (-0.5 V) to 5 V (-5 V) in steps of 0.5 V. The EFM signal (phase) scale ranges from 0 (blue) to 3 degrees (red). Each panel is a $15\mu\text{m}$ scan.

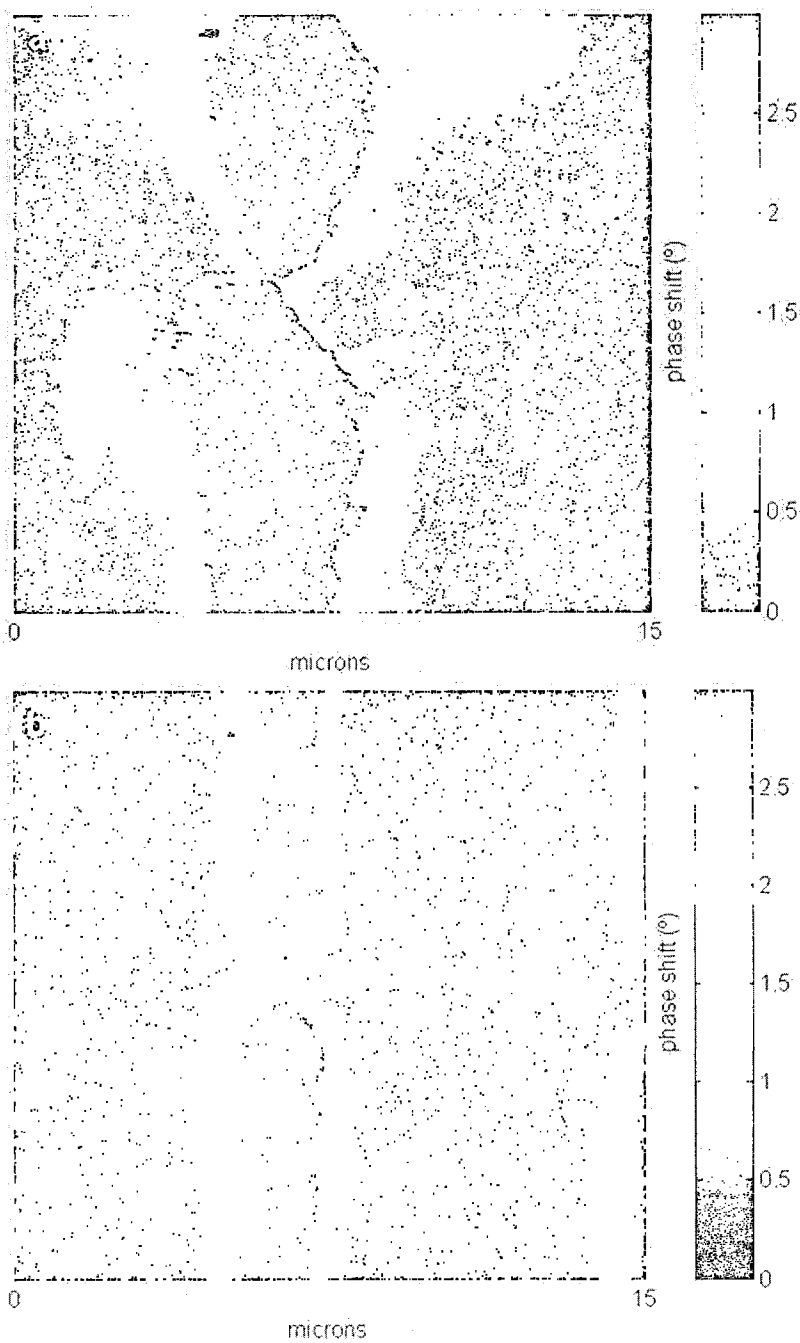


Figure 6.12: Comparison of the EFM signal (phase) for (a) voltages applied to the upper and lower electrodes (4 V, -4 V, respectively) with the tip grounded and (b) the electrodes grounded and the tip at 4 V. A neighboring electrode pair to the right can be seen as well in (b).

One possible explanation is that the NC film is Ohmic, but its contact with the electrodes is not. This possibility can be ruled out easily because if it were true, then the EFM signal seen in Figure 6.12(a) would have been uniform throughout the NC film and the non-Ohmic contact would at most have caused the NC film signal differ from the electrodes.

TEM characterization of the device revealed further insight into the role of NC film structure in charging behavior. The NC film is well characterized as a continuous NC film with very non-uniform layer number (thickness). Similar to the 3.5 nm diameter PbSe NC devices, the annealed NC film was very highly ordered. An important difference, however, is that the 6.8 nm diameter NCs did not pack into domains of relatively uniform height and cause film cracks, but instead formed super-crystal networks, branching throughout a fragmented monolayer background. Figure 6.9 shows representative TEM images of the NC patterns seen across the entire device surface. Figure 6.13 focuses on the area around the upper-right edge of the lower electrode studied in Figure 6.12. This region was chosen for detailed analysis because of the high degree of structure seen in its corresponding EFM image. Figure 6.13(a,b) show magnified AFM and EFM images of this area. Topographic structure can be seen to be correlated with EFM features, though there are many NC structures in the height image that do not appear strongly in the EFM image. Figure 6.13(c) shows a collection of roughly 25 TEM images that were sewn together to recreate the full region shown in the AFM and EFM images. The electrode edge can be seen as the large dark structure along the left edge of the image.

Figure 6.13(d) shows a higher magnification TEM image of a region corresponding to the middle of the EFM image, where a charged structure is seen extending \sim 25 degrees upward and to the right. The TEM image shows that this charged structure is a \sim 150 nm wide super-crystal that extends \sim 1 μ m from the lower-left corner of the image. Along its length, the height varies between \sim 16 nm and \sim 25 nm, corresponding to approximately 2 and 3 layers. Comparison with the EFM image

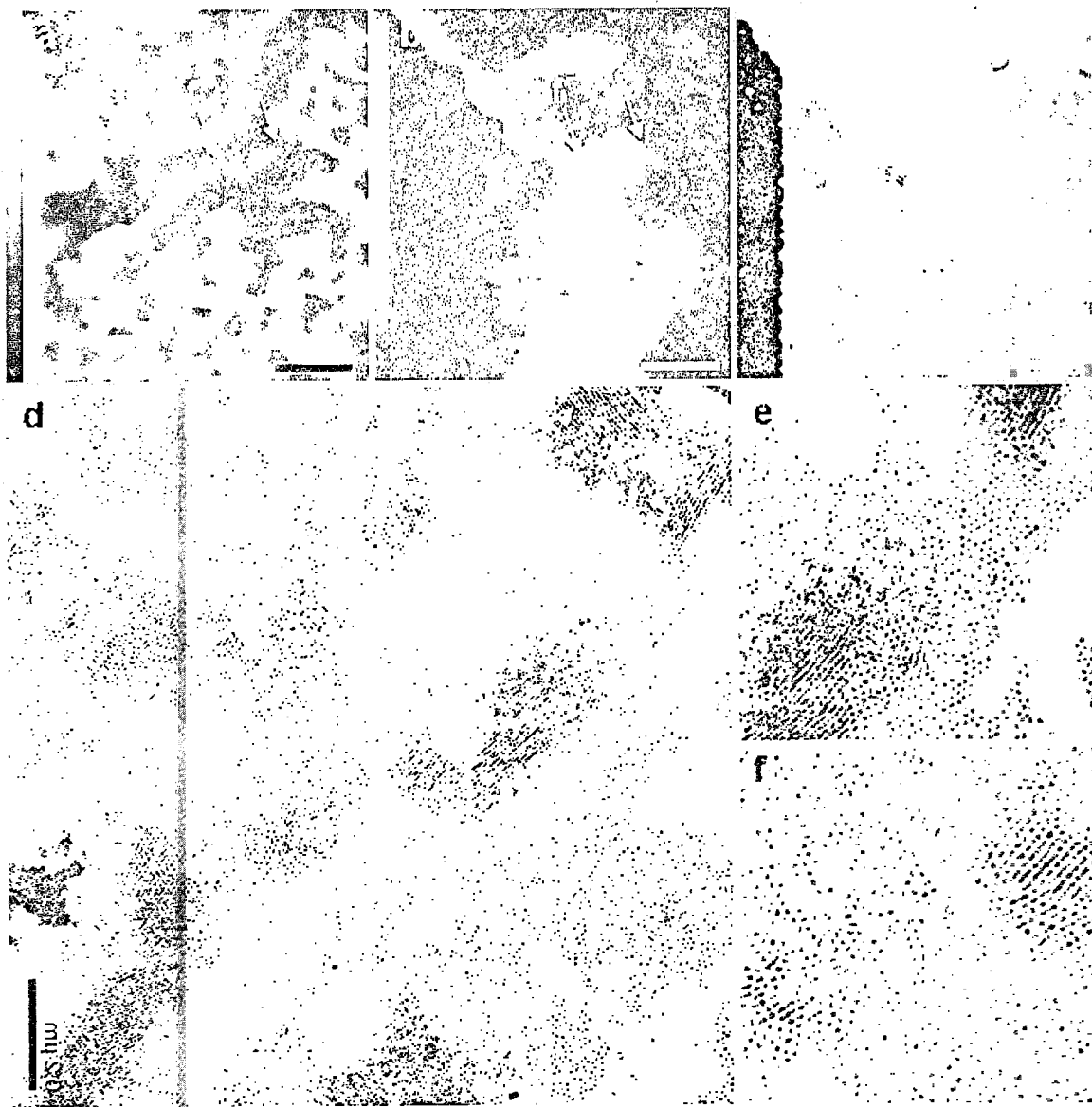


Figure 6.13: (a) Height image of a region along the right edge of the lower electrode where the highly structured PbSe NC film is in direct contact. Portions of the height structure match structure in (b) the corresponding EFM (phase) image. (c) A collection of about 25 TEM images taken in this same region and sewn together to recreate the full area seen in (a) and (b). The dark regions in the TEM image correspond to the NC super-crystal networks and the patterns match the AFM and EFM structure. (d) Higher magnification TEM image of the middle of the region. (e,f) TEM zoom-in corresponding to the regions indicated by arrows in (a,b,d). Charge was able to propagate through the few-layer channel (f) but not through the monolayer (e).

shows that charging was significantly interrupted by the transition from multi-layers to monolayer (Figure 6.13(e)). Furthermore, the superlattice in the upper-right region of the TEM image is not charged in the EFM image even though it is directly connected by monolayer patches to the highly charged superlattice. These observation indicate that charge transport through NC monolayer regions is very inefficient. This is somewhat surprising, considering that regions only 2 and 3 NC layers thick became significantly charged, as demonstrated in Figure 6.13(f).

By zooming-in further with the TEM, it was possible to observe that NCs in the multi-layer regions became more closely packed due to annealing than the NCs in the mono-layer regions, consistent with the contrast in charging efficiency. Figure 6.14 shows TEM images of the different inter-particle spacings mono-layers and multi-layers. Figure 6.14(a) shows a PbSe NC monolayer before annealing. The inter-NC spacing is ~ 2.5 nm (average). Figure 6.14(b) shows that the annealing treatment did reduce the inter-NC spacing, down to ~ 1.8 nm (average). The remaining images show that the inter-NC spacing was reduced much more significantly in multi-layer regions, to under 1 nm.

6.8 Conclusion

In conclusion, performing EFM on electrode gap devices containing PbSe NCs revealed them to be highly resistive, consistent with results from *I-V* characterization. Mild annealing resulted in significant increases in charging rates throughout the NC films, though charge distributions resulting from injection by electrodes at fixed voltages were non-uniform, with detailed structure that was sensitive to the applied voltage values. TEM imaging revealed that EFM signal contours were often the result of NC film discontinuities, but that charge transport through mono-layers was inefficient and their presence tended to suppress charge propagation between multi-layer regions. Further study is necessary to understand the mechanisms responsible.

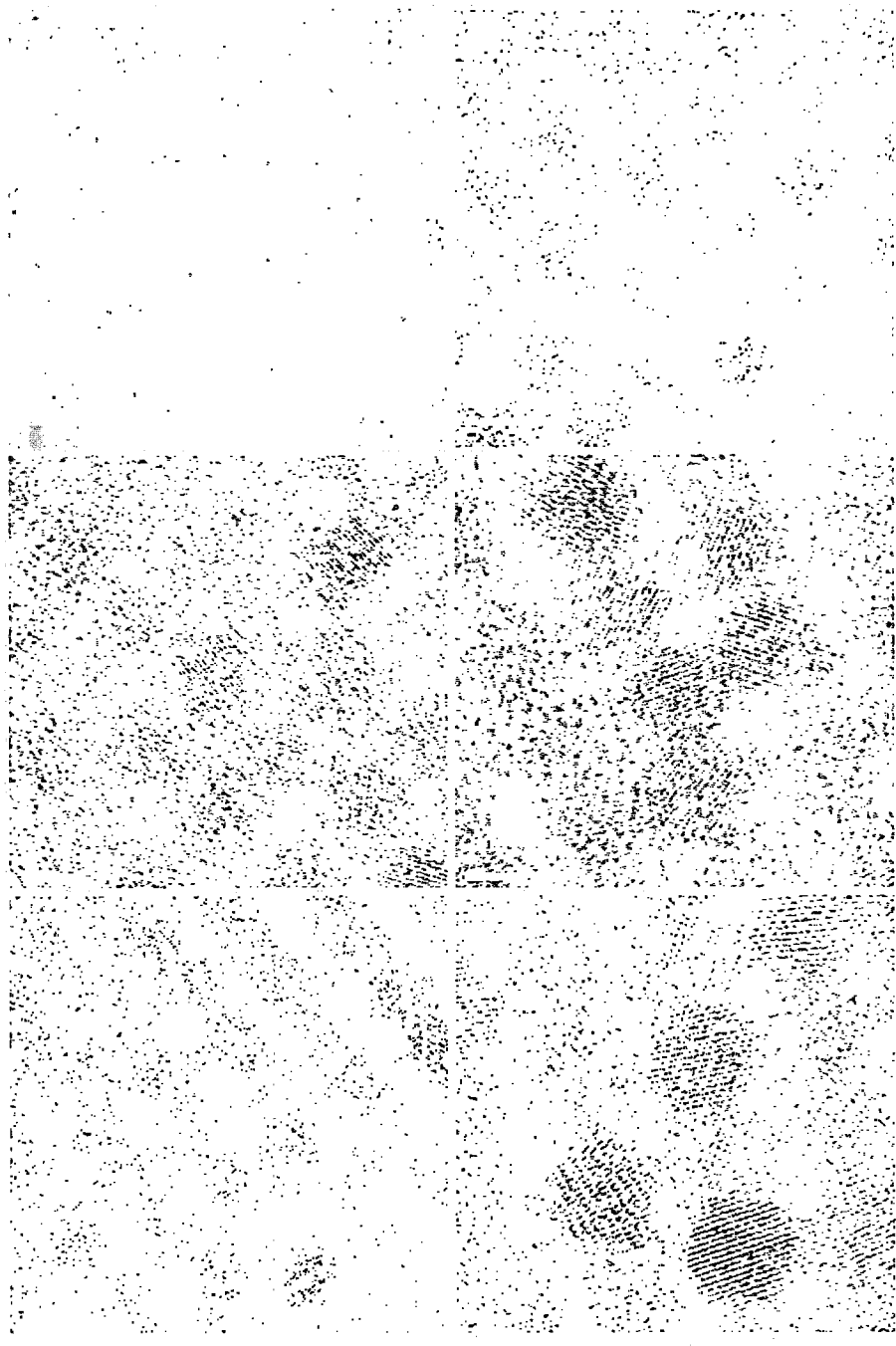


Figure 6.14: (a) TEM image of the PbSe NCs, as-deposited. (b) TEM image taken of PbSe NCs on the device after annealing at 130 C, showing reduced inter-NC spacing. (c-f) Multilayers of well ordered PbSe NCs after annealing showing substantially reduced inter-NC spacing. The lattice orientation of individual NCs can be seen. Scale bars are 10, 10, 5, 5, 10, 5 nm.

In addition to the seemingly enhanced reduction of inter-NC spacing in the multi-layers versus the mono-layers, it is possible that the local electrostatic environment and degree of wavefunction delocalization in the two cases are inherently different.

Chapter 7

Electronic Memory Effects in Large Assemblies of CdSe Nanocrystals

7.1 Introduction

Undoped semiconductor CdSe nanocrystal (NC) arrays have been found to be highly insulating.^[49,84] Due to the nanometer size scale of the NCs, quantum confinement effects play a dominant role in their electronic properties. Individual CdSe NCs have discrete energy levels separated by ~ 100 meV and charging energies ~ 150 meV.^[49] CdSe quantum dots are capped with ~ 1 -nm thick organic ligands which act as tunnel barriers for charge transport between adjacent dots. Time-dependent transport phenomena, history effects and persistent photoconductivity in CdSe NC arrays have been observed.^[49,50,84,85] Proposed models to explain these effects include charge traps,^[84] the Coulomb glass,^[49,50] and Lèvy statistics.^[86]

In this chapter, memory effects in the electronic transport in colloidal undoped CdSe NC quantum dot arrays are studied. Conduction through a NC array can be reduced by applying a negative voltage and then reset with a positive voltage. Light can be used to reset or even to increase conduction in the NC array. The switching

of the conduction in CdSe NC arrays is highly sensitive to the value and duration of the laser and voltage pulses. The ability to controllably switch NC array conduction can be exploited to fabricate memory devices composed of CdSe NCs. Such devices may be advantageous for several reasons. (i) Production of large quantities of CdSe NCs is easy and inexpensive. (ii) CdSe NC spectra are dependent on the NC size, which may allow selective memory resetting with visible light in devices composed of different size NCs. For instance, in a device composed of red and blue NCs, green light will reset the red NCs but not the blue NCs. (iii) As described in this letter, NC memory is robust, re-writable and persists for long times.

To study the memory effects, field-effect transistors (FETs) composed of organically-capped CdSe and CdSe/ZnS NCs were fabricated. Devices consisted of monodisperse TOPO-capped NCs, 3 to 6 nm in diameter, with rms size dispersion < 5%. NCs are either drop-casted or spin-coated onto the device from a highly concentrated hexane-octane solution and dried in vacuum. The NCs self-assemble between 1-mm long Au electrodes, separated by $\sim 2 \mu\text{m}$ on top of a 300-nm thick silicon oxide and a conductive gate below the oxide (Figure 38, inset).^[49] The NC film thickness was varied from a few to hundreds of NC layers. NCs were annealed in vacuum at ~ 600 K to 650 K for one hour *in situ* and measured at 300 K and 77 K. Annealing *in situ* decreases the separation between the NCs and increases the conductivity^[50] to a magnitude comparable with that of n-doped CdSe NCs.^[55] NCs were photo-excited with a 532 nm wavelength (green) diode laser operating at ~ 3 mW.

7.2 Results and Discussion

Figure 7.1 shows the current-voltage curves of a device with 5 nm CdSe NCs at 300 K and 77 K in the dark and during photo-excitation. Voltage was applied to the source electrode and current was measured at the drain electrode with a current amplifier; the gate was grounded. For this FET geometry, the photocurrent curve is nearly symmetric while the dark-current curve is highly asymmetric.

Hysteresis is seen in both cases and is inversely proportional to the voltage sweep rate. The dark current is ~ 0 for $V > 0$, while for $V < 0$ electrons contribute to transport.^[49] A constant negative voltage generates a current transient in the NC array which decays as a power law in time; specifically, $I(t) = I_0^{\alpha t}$ where $-1 < \alpha < 0$.^[49,50]

NC memory was probed with the four step voltage sequence shown in Figure 7.2. The four steps are labeled as, 1) write, 2) wait, 3) read and 4) erase to illustrate the potential for NC-based memory technology. The step durations are t_{write} , t_{wait} , t_{read} and t_{erase} , respectively and the current transients during the write and read steps are $I_{write}(t)$ and $I_{read}(t)$, respectively; $I_{write}(T)$ and $I_{read}(T)$ are the currents at time T after the start of their corresponding voltage steps. This four step cycle will be referred to as the memory cycle. The first three steps are the voltage pulses -

V

, 0, and -

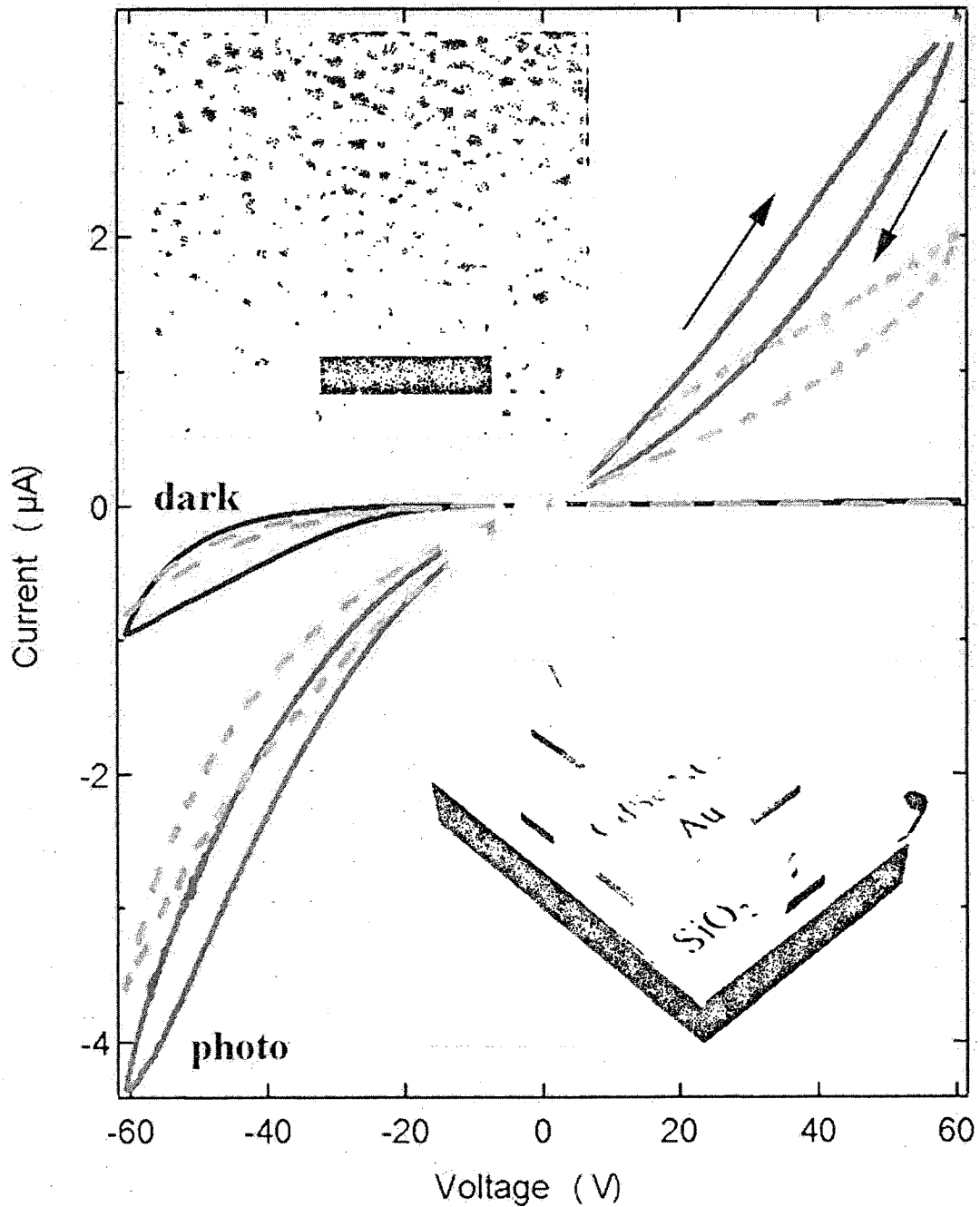


Figure 7.1: Current-voltage curves at 300 K (dashed lines) and at 77 K (solid lines) for an array of 5 nm TOPO-capped CdSe nanocrystals (NCs) in the dark and during excitation with green laser. The voltage sweep rate is 1 V/s. Upper inset: transmission electron micrograph of the NC film. The scale bar is 50 nm. Lower inset: device schematic; 1-mm long electrodes are separated by 2 μm . The back gate is grounded.

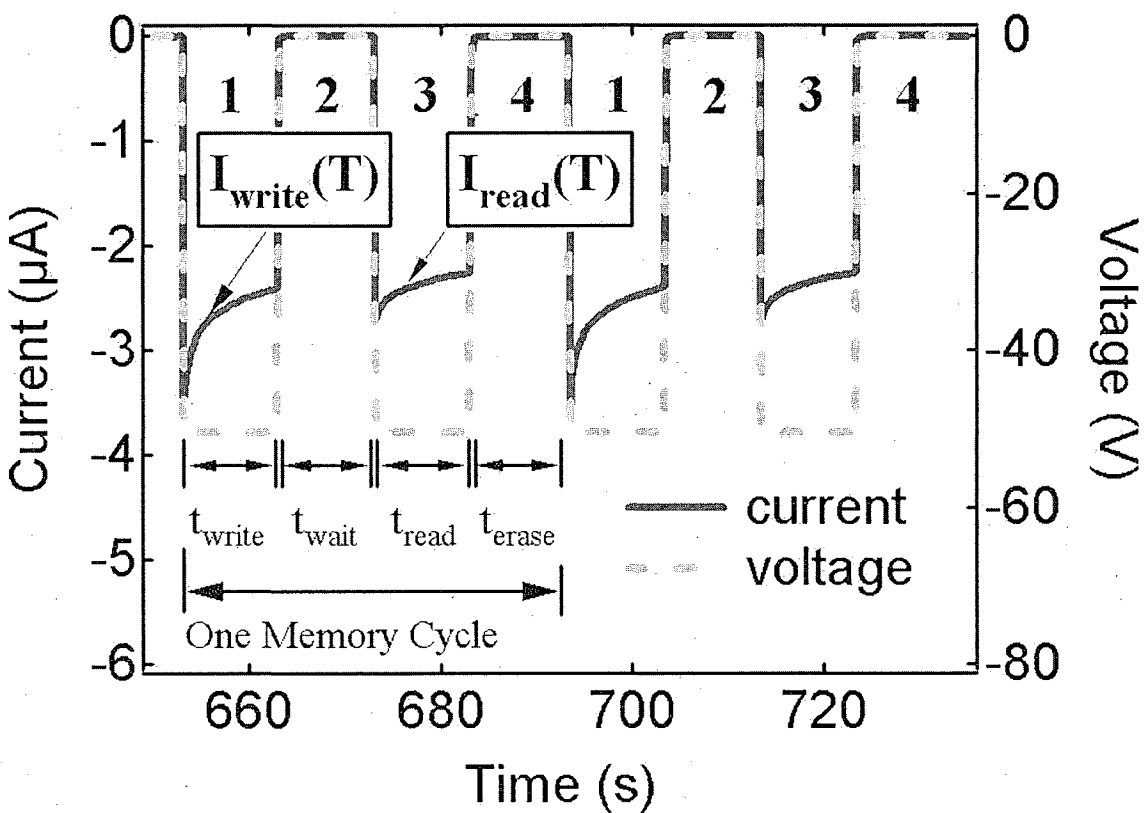


Figure 7.2: Voltage (dashed line) and current (solid line) vs. time for two consecutive memory cycles for the device in Fig.1. The numbered steps are: 1) write ($V < 0$, dark), 2) wait ($V = 0$, dark), 3) read ($V < 0$, dark), 4) erase ($V = 0$, photoexcitation) OR ($V > 0$, dark). In this example, $t_{\text{write}} = t_{\text{wait}} = t_{\text{read}} = t_{\text{erase}} = 10$ s and $V = -50$ V during t_{write} and t_{read} . In step 4, NCs were photoexcited. $I_{\text{write}}(T)$ and $I_{\text{read}}(T)$ are currents at time T after the start of the write and read steps, respectively.

$V|$. As shown in Figure 7.2, this generates the current transient sequence, $I_{write}(t)$, 0, and $I_{read}(t)$, respectively, where $|I_{read}(t)| < |I_{write}(t)|$. In the fourth step, either a positive voltage is applied or photo-excitation is induced with visible light at $V = 0$. This fourth step is used to reset or erase the memory so that a subsequent application of $-|V|$ will generate $I_{write}(t)$ again. Memory cycles were measured for electric fields from 0 to $-30 V/\mu m$; t_{write} , t_{wait} , t_{read} and t_{erase} , were each varied from 1 s to 1000 s. Measurements were performed for both positive voltage and visible light resetting. In all cases $|I_{read}(T)| < |I_{write}(T)|$. Memory was exhibited at both 300 K and 77 K for all voltages. The results shown are for 77 K and $E = -2.7 \times 10^5 V/cm$ across the device.

Figure 7.3 (a) shows $|I_{write}(T)|$ and $|I_{read}(T)|$ for a thousand consecutive memory cycles from the device in Figure 7.2. Here, $T=500$ ms, $t_{write} = 1$ s, $t_{wait} = 3.5$ s, $t_{read} = t_{erase} = 1$ s and photo-excitation was used in the erase step. As shown, $|I_{read}(T)| < |I_{write}(T)|$ and both are nearly constant over thousands of iterations (~ 2 hrs). To illustrate the potential of CdSe NCs for memory applications, $I_{write}(T)$ and $I_{read}(T)$ can be defined as two states, “1” and “0”, respectively. The difference $\Delta I(T) = |I_{write}(T) - I_{read}(T)| \sim 0.2 \mu A$ is sufficiently large to avoid overlap of “1”s and “0”s due to current fluctuations ($\sim 10 nA$). $\Delta I(T) > 0.1 \mu A$ for all t_{write} , t_{wait} , t_{read} and t_{erase} . The memory properties are robust. The device in Figure 1 was probed with thousands of voltage pulses over three months and no measurable degradation was observed.

Reversible switching of the current between “1” and “0” states in Figure 40 (a) can be explained by charge trapping in the NC array. During negative voltage pulses, electrons are injected into the array and some get trapped. Coulomb interactions between charges in CdSe NC arrays are unscreened and allow the trapped electrons

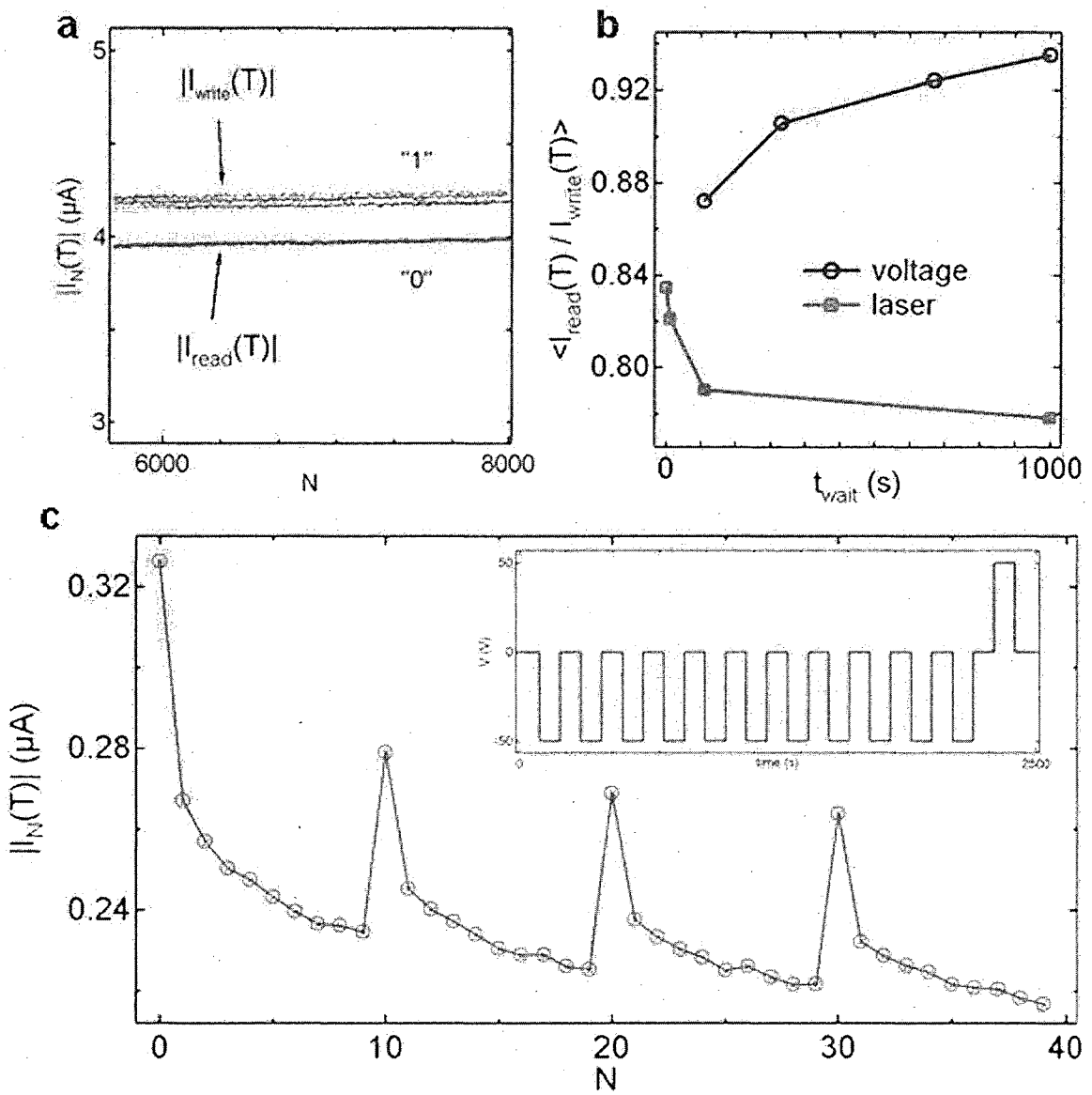


Figure 7.3: (a) $|I_N(T)|$ vs. the transient number i.e., the number of the negative voltage steps, N , for 1000 consecutive memory cycles. $I_N(T)$ is the current at time T after the application of the N^{th} negative voltage step. $I_{\text{write}}(T)$ and $I_{\text{read}}(T)$ correspond to even and odd values of N , respectively (see Figure 7.2); $t_{\text{write}} = t_{\text{read}} = t_{\text{erase}} = 1$ s, $t_{\text{wait}} = 3.5$ s, $T = 500$ ms, $V = -50$ V and photoexcitation was used to erase. (b) $|I_N(T)|$ vs. the transient number, N , for consecutive memory cycles modified to have nine read steps per cycle; $t_{\text{write}} = t_{\text{wait}} = t_{\text{read}} = t_{\text{erase}} = 100$ s, $T = 500$ ms, $V = -50$ V and positive voltage was used to erase. Inset: Voltage vs. time for one modified memory cycle ($N = 0$ to 9). (c) The average value $\langle I_{\text{read}}(T)/I_{\text{write}}(T) \rangle$, calculated over consecutive iterations, vs. t_{wait} for positive voltage erasing (circles) and photoexcitation erasing (squares).

to repel new electrons from entering the array, which reduces conduction. A positive voltage pulse removes trapped charges and therefore enhances conduction. This interpretation is supported by Figure 7.3b) which shows memory cycles modified such that $I_{read}(T)$ is measured nine times before the NCs are reset (by positive voltage).

The number of trapped charges increases with each additional negative voltage pulse and each set of nine $I_{read}(T)$ values show monotonic decrease. In each cycle, the positive voltage used in the erase step removes most but not all of the trapped charges that accumulate during the single write step and the nine read steps. The currents in the subsequent cycles are therefore lower (Figure 7.3(b)). Even without the positive voltage step, trapped charges are able to diffuse out of the NC array during the wait step, when $V=0$ across the array. As t_{wait} increases, the number of charges which escape during this step increases. This is reflected in the upper curve (triangles) in Figure 7.3(c) showing the average ratio $\langle I_{read}(T)/I_{write}(T) \rangle$ plotted against t_{wait} . As expected, $\langle I_{read}(T)/I_{write}(T) \rangle$ increases as t_{wait} increases. As t_{wait} approaches infinity, all of the trapped charges diffuse out of the array and $\langle I_{read}(T)/I_{write}(T) \rangle$ approaches unity.

The lower curve in Figure 7.3(c) shows $\langle I_{read}(T)/I_{write}(T) \rangle$ vs. t_{wait} when photo-excitation at $V = 0$ is used as the erase step. As shown, $\langle I_{read}(T)/I_{write}(T) \rangle$ decreases as a function of t_{wait} , which is opposite to the behavior for positive voltage erasing. It was shown in Figure 7.1 that the photocurrent is significantly larger than the dark current. Photoconductivity has previously been shown to persist in thin films of CdSe NCs for up to 10^4 s after exposure to light.^[84] This mechanism of persistent photoconductivity explains the lower curve in Figure 7.3(c). Persistent photoconductivity is at its maximum immediately after the photo-excitation erase step ends, and then decays. $I_{read}(T)$ is measured at a time $\tau = t_{write} + t_{wait} + T$ after

the erase step ends. As τ increases, the persistent photoconductivity decreases and $|I_{read}(T)|$ decreases. The lower curve in Figure 7.3(c) can therefore be interpreted as a measurement of the decay of persistent photoconductivity.

When photo-excitation is used to erase NC memory, the effect of persistent photoconductivity can be used to “tune” the NC array’s response to the write and read steps. If many memory cycles are measured consecutively, increasing (decreasing) t_{erase} , i.e., the duration of photo-excitation at $V = 0$, will increase (decrease) $|I_{write}(T)|$ and $|I_{read}(T)|$ with each iteration of the memory cycle. To demonstrate this effect, t_{write} and t_{wait} were held constant while t_{erase} (by photo-excitation) was varied. First, t_{erase} was set to 1 s and then increased by one order of magnitude after every ten memory cycles, up to $t_{erase} = 1000$ s. After ten $t_{erase} = 1000$ s cycles, t_{erase} was set back to 1 s and the entire 40-step sequence was repeated. Three consecutive 40-step sequences are shown in Figure 7.4 for $t_{write} = t_{read} = t_{wait} = 10$ s. As shown, the slopes of the two lines, $|I_{write}(T)|$ and $|I_{read}(T)|$, change periodically with each repetition of the 40-step sequence. The slopes are negative for $t_{erase} = 1$ s (i.e., $t_{erase} / t_{write} < 1$), nearly zero for $t_{erase} = 10$ s ($t_{erase} / t_{write} = 1$) and positive for both $t_{erase} = 100$ s and $t_{erase} = 1000$ s ($t_{erase} / t_{write} > 1$). The increase (decrease) of the slopes as t_{erase}/t_{write} increases (decreases) was observed for all parameters. The slopes and the ratio t_{erase} / t_{write} for which the slopes change sign, depend on t_{wait} and the laser power. As shown in Fig. 41, the current increase for $t_{erase} = 1000$ s is greater than the current decrease for $t_{erase} = 1$ s and there is, therefore, a net increase of the current. After ~ 120 hrs of repeating these 40-step cycles, the current was increased by nearly an order of magnitude.

In conclusion, colloidal CdSe NCs show robust memory effects that can be exploited for memory applications. NC memory can be erased electrically or optically

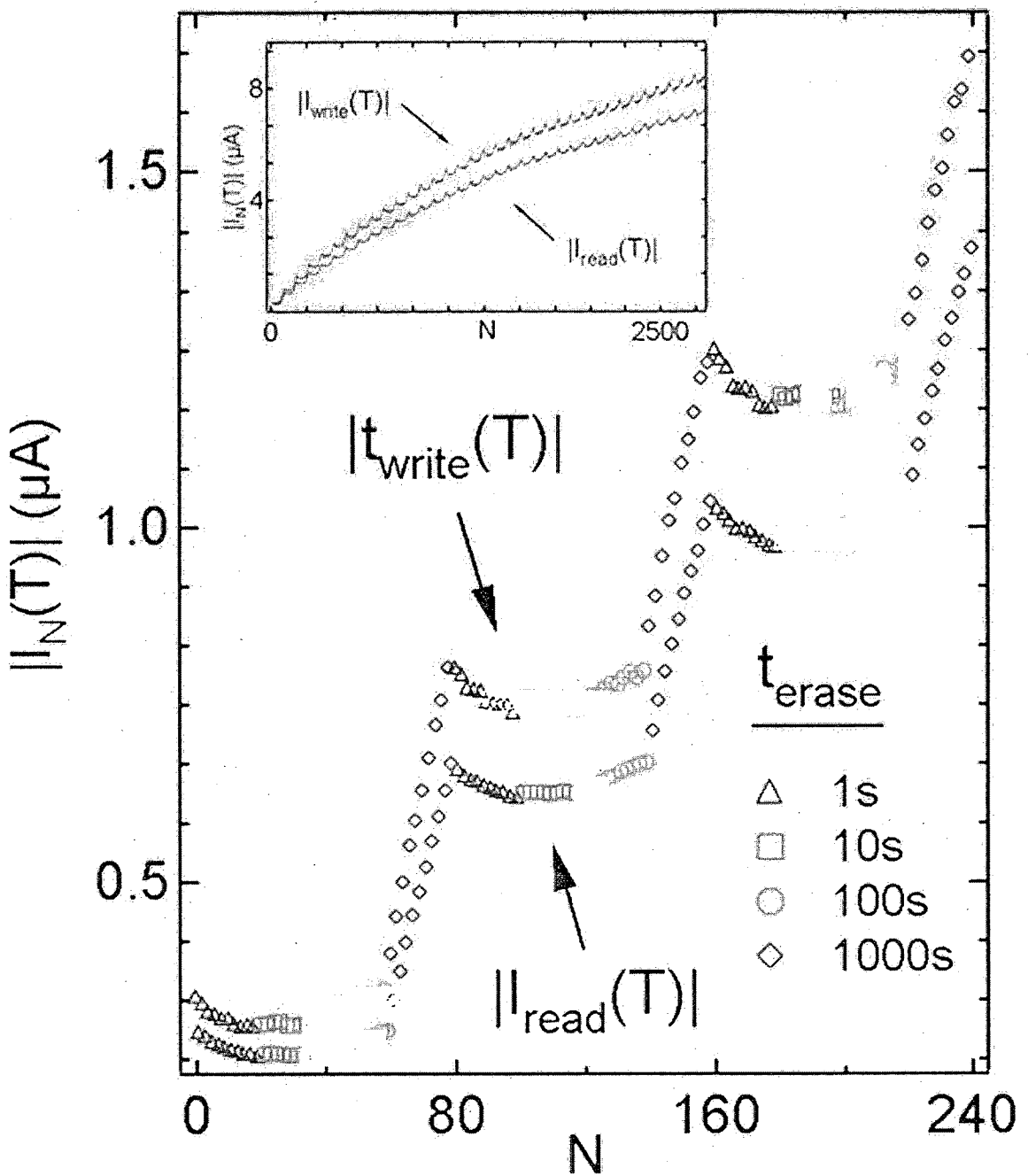


Figure 7.4: $|I_N(T)|$, the current at time T after the application of the N^{th} negative voltage step, versus the transient number, N , for consecutive memory cycles with laser resetting (Figure 7.2); t_{erase} changes every ten cycles from $t_{\text{erase}} = 1\text{s}$ (triangles), to 10s (squares), 100s (circles) and 1000s (diamonds). After ten $t_{\text{erase}} = 1000\text{s}$ memory cycles, t_{erase} is set back to 1s and the entire 40-step sequence is repeated; $t_{\text{write}} = t_{\text{wait}} = 10\text{s}$, $T = 500\text{ ms}$ and $V = -50\text{ V}$. The first 3 repetitions of these 40-step sequences are shown. $I_{\text{write}}(T)$ and $I_{\text{read}}(T)$ correspond to even and odd values of N , respectively (see Figure 7.2). In one 40-step sequence N increases by 80. Inset: $|I_N(T)|$ vs. the transient number, N , for ~ 35 repetitions of 40-step sequences (~ 120 hrs).

and is re-writable. CdSe NC memory devices can be scaled down. For example, for a 100 nm gap, the voltage required to obtain similar currents is ~ 5 V.

Chapter 8

Nanogaps by direct lithography for high-resolution imaging and electronic characterization of nanostructures

8.1 Introduction

Efforts toward achieving electrical contact to nanostructures have been active for over a decade.^[87-90] Even though several devices based on “nanogaps” - two wires separated by a nanometer-scale distance - have been demonstrated,^[48,77,88,91-93] their realization has remained a significant challenge. Even the best methods are highly labor intensive and suffer from low yield and poor geometrical control. Most nanogaps are also incompatible with high-resolution transmission electron microscopy (HRTEM). As a consequence, the proof of the nanogaps’ quality and content in past studies has been indirect. Moreover, interesting quantum effects, such as Coulomb blockade and Kondo effects, have now been reported in electromigrated-breakjunction gaps containing no sample - only metallic debris produced from the fabrication.^[78,79] High-resolution imaging is therefore required to ensure the quality of nanogaps and

to be able to identify possible artifacts.

In this chapter, a technique for fabricating sub-nanometer size gaps on thin membrane substrates directly with electron beam lithography (EBL) is described. Because these nanogaps are made on thin films, it is easy to examine their structure and content with HRTEM.

The EBL on was performed on thin SiN_x membrane substrates with a thermal-emission JEOL 6400 scanning electron microscope (SEM) operating at its maximum accelerating voltage of 30 kV. The electron beam (smallest attainable diameter \sim 30 nm) was controlled with a Raith writing program. A layer of C2 PMMA (950 molecular weight PMMA, 2% in chlorobenzene) was spin-cast onto the SiN_x windows at \sim 5000 rpm to achieve a resist thickness of \sim 100 nm. Nanogaps were written using a 10 pA electron beam in the EBL chamber with pressure below 10^{-6} Torr. The resist was exposed at a magnification of 2000 \times , corresponding to a write field of $(40 \mu\text{m})^2$, to beam doses ranging from 600 to $900 \mu\text{C/cm}^2$, depending on the desired size and geometry of the nanogap. Larger features were then written into the resist with standard EBL parameters for the purpose of later connecting the nanogaps to large contact pads. The device was then developed in MIBK:IPA (3:1 volume ratio) for 60 seconds and loaded into the low pressure environment of a thermal evaporator. For metallization, several nanometers of either nickel or chromium were evaporated first to act as an adhesion layer between the gold and the substrate, followed by 30 nm of gold. The wafers were put into acetone at room temperature in order to achieve lift-off. The gaps were then imaged with JEOL 2010 and JEOL 2010F Transmission Electron Microscopes.

8.2 Results and Discussion

Figure 8.1 shows TEM images of examples of nanogaps on SiN_x membranes with gap sizes 0.7, 1.5, 3, 4, 5 and 6 nm (Figure 8.1 (a-f), respectively). A HRTEM image of another 4 nm gap is also shown (Figure 8.1(g)). This nanogap fabrication process is high-yielding and hundreds of nanogaps have been made controllably from as small as < 1 nm to arbitrarily large size with step sizes < 1 nm. These nanogaps are robust at room temperature and do not change over time.

This high-resolution fabrication was achieved as the result of minimizing electron back-scattering during the EBL processing. Electron back-scattering is the primary factor limiting the feature resolution of EBL. Efforts to understand and reduce electron back-scattering in EBL date from the 70s and 80s, with most contributions made by IBM.^[94-96] Interestingly, despite these efforts and the acquired fundamental knowledge, the potential of this knowledge has not been explored for realizing nanogaps. Moreover, recent efforts of making nanogaps compatible with TEM characterizations pursued electromigration without first exploring the limitations of standard EBL.^[97] Electromigration induced by high-intensity electron-beam irradiation in a HRTEM has also been demonstrated, though without much control.^[98]

Standard EBL is a several step process. In short, a layer of “electron-resist” (PMMA) is spin-cast onto a wafer and exposed to an electron beam in targeted areas. The energetic electrons break the PMMA bonds and this soluble resist is dissolved. The remaining resist acts as a stencil of the lithographically defined pattern. Devices are made by metal deposition and a “lift off” of the undesired metal by dissolving the resist underneath it. The final device is composed of metal features

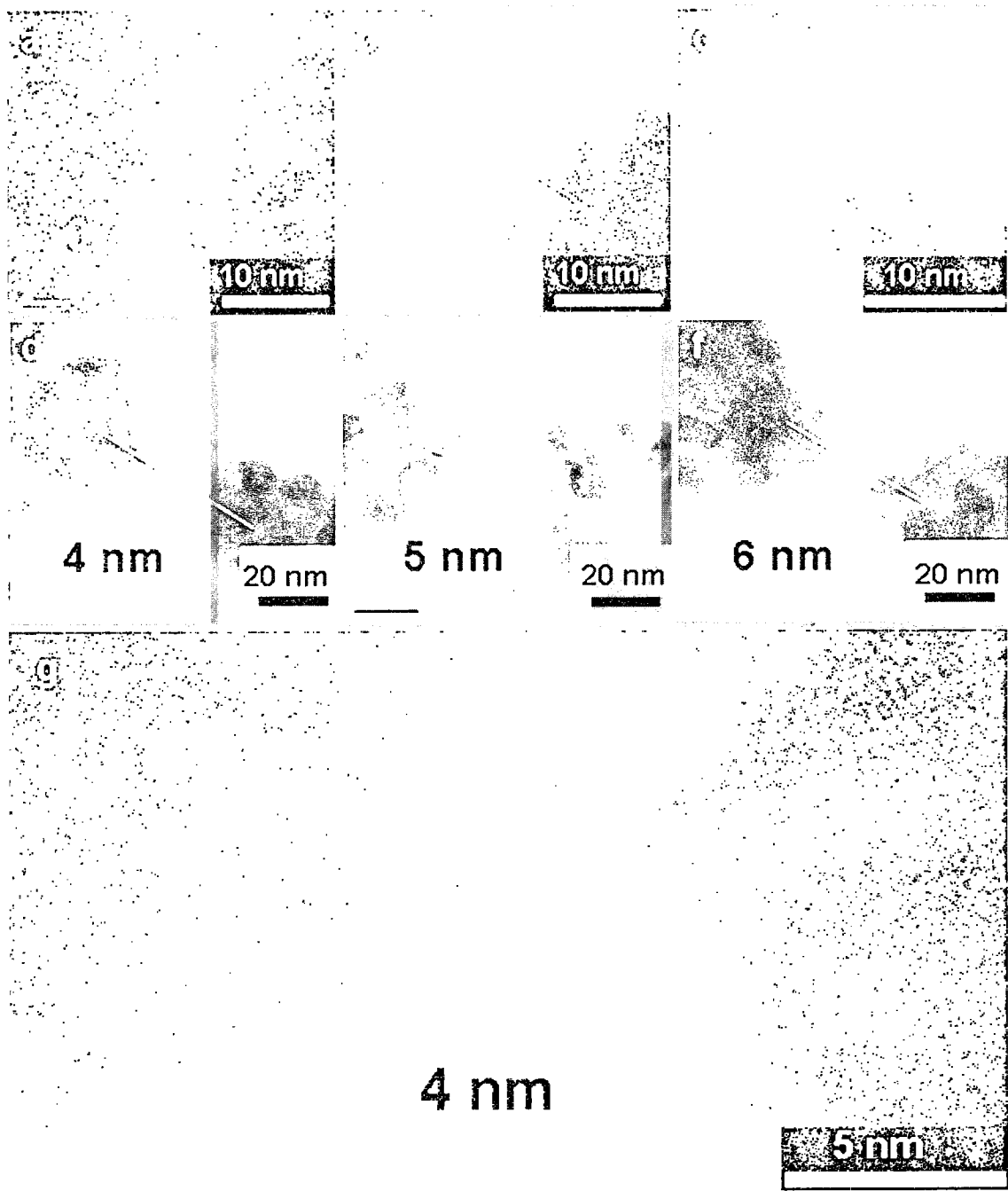


Figure 8.1: TEM image of nanogaps with sizes 0.7 nm (a), 1.5 nm (b), 3 nm (c), 4 nm (d), 5 nm (e) and 6 nm (f). (g) HRTEM image of another 4 nm nanogap. The crystal lattice planes of the electrodes (g) are seen clearly. Inset to (a): SEM image of a full device consisting of electrodes (white lines) on a suspended $50 \mu\text{m} \times 50 \mu\text{m}$ SiN_x membrane (black square) and connected to larger wires. Inset to (c): TEM image of electrodes (black lines) on a suspended SiN_x membrane.

defined by the EBL pattern.

Figure 8.2(a) is a schematic of the electrons' trajectories in a thick resist-insulator-silicon substrate. The incident electron beam passes through the PMMA resist and the insulator (in this example, SiO_2) without affecting most of the resist bonds. When these "forward-scattered" electrons reach the doped silicon, strong scattering with the silicon lattice cause many to reflect backward with a wide spatial distribution and energies similar to that of the incident beam. The size of this burst of back-scattered electrons largely determines the size of the feature written. Worse still, areas intended to remain unexposed can get a large dose of these energetic electrons. This phenomenon is known as the "proximity effect".^[99]

If the distributions of scattered electrons (Figure 8.2(a)) are approximated as Gaussian, with "characteristic widths", σ_f and σ_b , for the forward-scattered and back-scattered electrons, respectively, then the distribution of resist exposure is given by the energy deposition function (EDF),^[100]

$$F(r) = k \left(\exp \left[-\left(\frac{r}{\sigma_f} \right)^2 \right] + \eta \left(\frac{\sigma_f}{\sigma_b} \right)^2 \exp \left[-\left(\frac{r}{\sigma_b} \right)^2 \right] \right). \quad (8.1)$$

Here, r is the radial distance from the exposure center, η is the ratio between the energy dissipation of back-scattered and incident electrons along the beam axis and k is a constant used to normalize $F(r)$ to 1 at $r = 0$. For a 500 nm-thick layer of PMMA resist on doped silicon and using a 25 keV incident beam, σ_f , σ_b and η are 0.06 μm , 2.6 μm and 0.51 respectively.^[100] Figure 8.2(b) is a schematic of a thin SiN_x membrane used in this work. Here, the proximity effect is reduced dramatically, $\sigma_b \sim 0$, and the EBL feature resolution is limited by the much smaller value σ_f and the EDF becomes

$$F(r) \sim \exp \left[-\left(\frac{r}{\sigma_f} \right)^2 \right]. \quad (8.2)$$

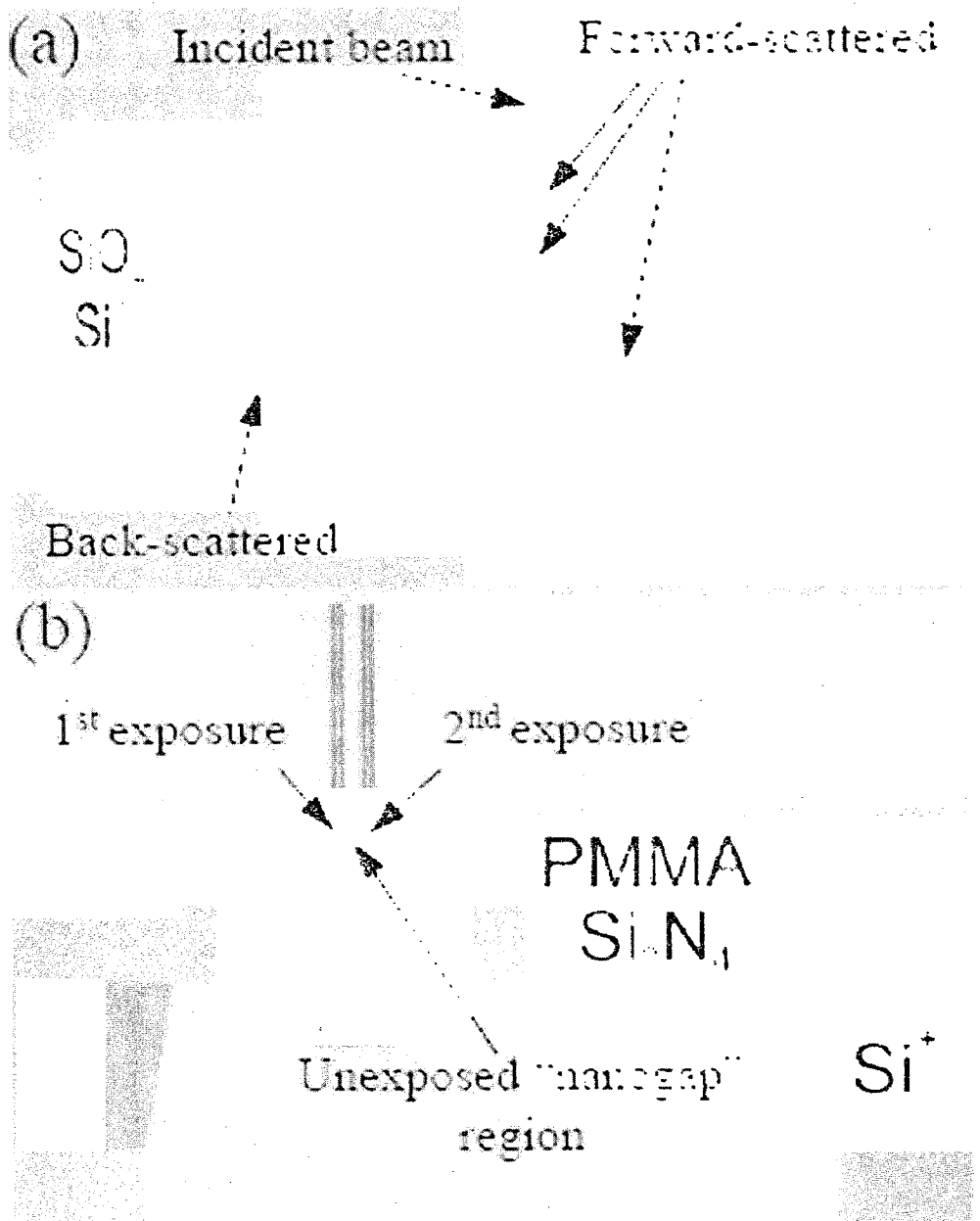


Figure 8.2: (a) Standard PMMA- SiO_2 - Si^+ substrate. An incident electron beam “forward-scatters” slightly in the PMMA and SiO_2 layers. Strong scattering in the Si^+ results in broadly distributed “back-scattered” electrons which expose a wide region of the PMMA. (b) PMMA- SiN_x substrate used to make nanogaps with EBL. Two nearby areas are shown being sequentially exposed to an electron beam while the small “nanogap” region between them is left unexposed.

Conveniently, the distribution of forward-scattered electrons decreases with increasing r even faster than a Gaussian and is better approximated by multiple small-angle scattering events.^[101] Because of the extremely narrow distribution of electrons in the absence of back-scattering, it is possible to expose two nearby regions while leaving a nanometer-scale gap between them unexposed (Figure 8.2(b)). These results thus demonstrate that electron back-scattering can be sufficiently minimized to make nanogaps efficiently and down to < 1 nm. These results are not necessarily limited to thin substrates because electron back-scattering can, in principle, be sufficiently reduced on appropriately processed thick substrates. However, as shown here, the ability to image nanogaps and their content with HRTEM is a valuable tool for the fundamental characterization of nanostructures and this capability is only possible with thin substrates.

In conclusion, an efficient route to fabricating high-quality nanometer-size electrode gaps compatible with atomic resolution imaging has been discovered. The fabrication of these nanogaps is direct and can be achieved by anyone with access to a standard EBL system. In addition to their usefulness, nanogaps represent substantial progress towards bridging the classical and quantum worlds.

Chapter 9

Sub-10nm device fabrication using a transmission electron microscope

9.1 Introduction

The ability to efficiently fabricate high quality nano-structured devices is important because many physical, chemical and biological properties of diverse systems depend on electron motion, fluid motion and/or chemical reactions that occur at nanometer scales. For instance, electrons typically travel a few nanometers at room temperature before scattering inelastically in metals^[102] or flipping their spin in ferromagnetic metals^[103] and their transition into the superconducting phase becomes sensitive to size at ~ 10 nm.^[104-107] Nanometer scale fluid flow deviates from bulk flow^[108] and water confined in a nanometer scale volume crystallizes at room temperature.^[109] Control over molecular motion in nanometer wide channels is important for studies of molecular-scale mass transport and for nanofluidic applications in genomics.^[110] In pursuing nanoscale science many different approaches have been undertaken to fabricate the small structures needed to probe the phenomena. The widely used resist-based scanning electron beam lithography techniques are limited down to 10's of nm's and top-down fabrication of sub-10 nm scale devices with high reproducibility

and yield is generally still challenging.

In this chapter, the use of a transmission electron beam (TEB) to make nanoscale metal devices of arbitrary geometries on insulating platforms is demonstrated. This technique should additionally facilitate a range of nanoscience applications including nanoelectronics and molecular translocation studies. This new top-down TEB-based method works by controllably ablating evaporated metal films, pre-patterned with electron beam lithography (EBL) on silicon nitride membrane substrates, to produce intricate metal (Ni, Cr, Al, Ag and Au) nanoscale devices with near atomic precision. A variety of different device geometries is shown (nanoscale gaps, channels, wires, discs, rings, 3, 4 and 8-terminal electronic devices, etc.) with sub-10 nm features with straight and circular segments and their fabrication, electrical characterization and applications are discussed. These nanostructures are fabricated at precise locations and seamlessly integrated into large-scale circuitry without contact resistance.

This TEB-“ablation lithography” (here referred to as TEBAL) does not require the use of resist or a lift-off step. Furthermore, *in situ* imaging of metal ablation allows for real-time feedback control and Angstrom-resolution visual inspection of the fabricated devices. Together, these benefits allow for low surface roughness ($< 5\text{\AA}$) and high reproducibility of the TEBAL-fabricated nanostructures.

9.2 Example Nanostructures

To illustrate the flexibility of TEBAL Figure 9.1 shows three example structures made from a Ni/Cr alloy: a nanoring (Figure 9.1a) with inner and outer radii of ~ 3 nm and ~ 18.5 nm, a three-terminal single-electron transistor (Figure 9.1b) and a serpentine, U-shaped, wire (Figure 9.1c) with a width of ~ 6 nm, total length of

\sim 40 nm and radius of curvature of \sim 1 nm at the three bends. A corresponding schematic is shown for each structure for clarity. Each structure was intentionally left connected to its “parent leads” to demonstrate the ease of their integration into complete circuits. The feature sizes were measured with the same Gatan Digital Micrograph Image Software that was used to obtain the HRTEM images. The images were not altered or processed in any way after being captured by the CCD camera of the HRTEM (i.e., they are “raw”). The contrast, brightness and sharpness in the images are exactly as they appear to the user during the fabrication.

Post-fabrication, the structures were imaged several times over a period of weeks and displayed no sign of change or “relaxation” into different shapes over time. TEBAL fabrication has the added advantage of maintaining a resistance-free contact between a nanostructure and its leads. This is in contrast to bottom-up (e.g. chemically-synthesized) nanostructures which typically need to be first located on a chip and then contacted to larger circuitry, all after their fabrication.

9.3 Methods

9.3.1 Preparation

The TEBAL process is outlined in Figure 9.2 which illustrates the fabrication of a \sim 18-nm large Ni/Cr metal disc connected to the parent-leads with two short \sim 4.5-nm wide nanowires. The metal to be nanosculpted by the ablating beam was first pre-patterned by electron beam lithography (EBL) into an \sim 80-nm wide metal strip on a SiN_x membrane that is itself essentially transparent to the electron beam.

Using electron beam lithography (EBL) metal films are pre-patterned onto one

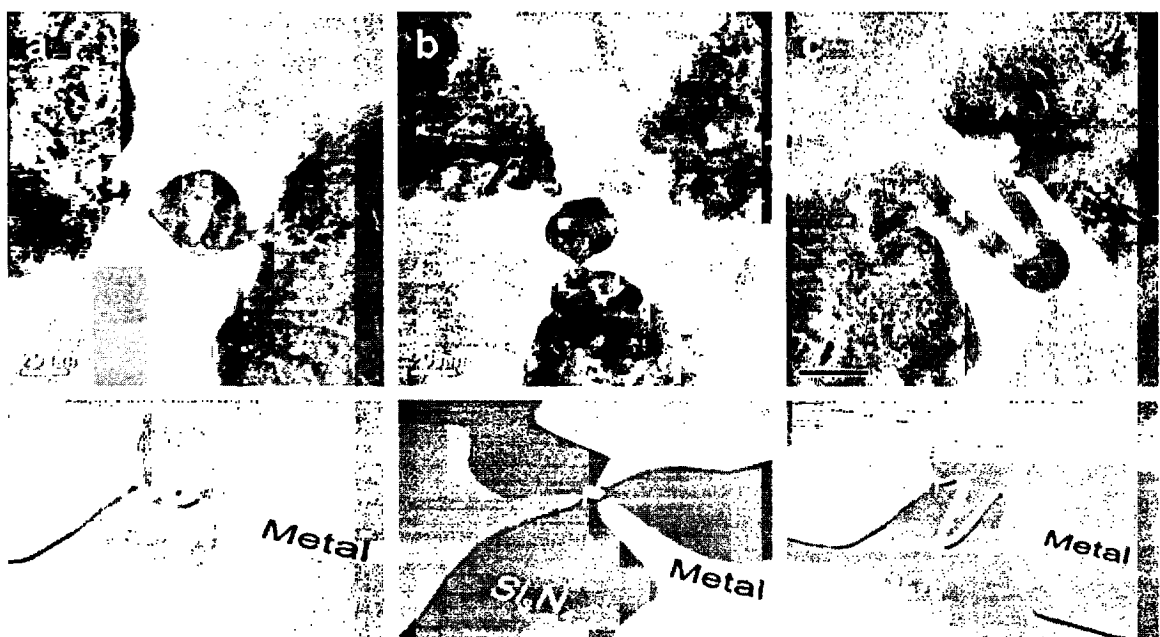


Figure 9.1: Example structures to demonstrate the flexibility of TEBAL. Each of the three structures shown in the TEM images is accompanied by a schematic (below) showing the fabrication by TEBAL. (a) Nanoring with outer radius of ~ 18.5 nm and inner radius of ~ 3 nm (scale = 20 nm). (b) Three-terminal electronic device: source and drain leads are coupled to a ~ 13 nm radius metallic island and a gate electrode ~ 23 nm away from the island (scale = 20 nm). The rate limiting tunneling barrier (upper junction) is a 2.7 nm gap. (c) Serpentine wire with 6 nm width (scale = 20 nm). All lengths were measured with Gatan's Digital Micrograph Image Analysis software.

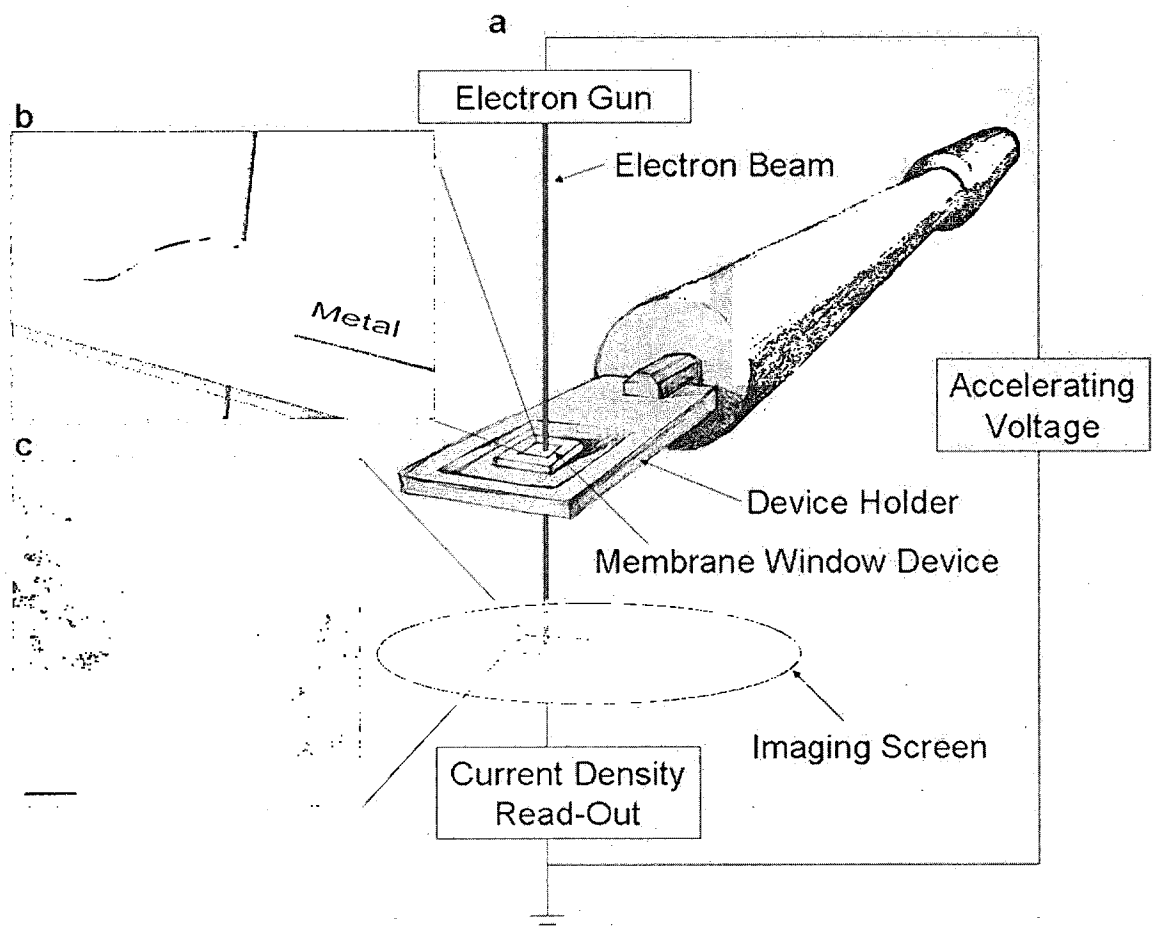


Figure 9.2: (a) A membrane window device with pre-patterned metal lines on its surface is loaded into the TEM environment. The metallized surface of the membrane faces away from the beam source (i.e., towards the imaging screen). A hole (not shown) in the device holder allows the beam to pass completely through the membrane and reach the imaging screen. (b) Schematic of the ablation of a pre-patterned wire to achieve a metal disk that is connected to the initial metal on both sides. (c) TEM image of an actual 18 nm diameter metallic disk that was nanosculpted from Ni/Cr with TEBAL and left connected to the parent-leads with two ~ 4.5 nm wide nanowires (scale = 20 nm). The imaging screen enables real-time visual feedback for a user or real-time current density feedback for computerized control.

side of the membrane surface. The thickness of evaporated metal films ranged from 10 to 50 nm. Metal films were evaporated using standard thermal evaporated procedures at a rate ~ 0.3 nm/s and pressure $< 10^{-6}$ Torr. The feature resolution achieved on SiN_x membranes with EBL is enhanced significantly due to the minimization of electron backscattering and high-quality nanogaps can be directly fabricated with EBL, as discussed in Chapter 8. It is therefore possible to start with metal features that are already small compared to what is usually achieved with EBL on thick $\text{SiO}_2/\text{Si}+$ substrates and then proceed with TEBAL to make structures with more complicated geometries, such as those presented in this paper, which are inaccessible with EBL only (e.g. Figure 9.1).

9.3.2 Nanosculpting

The EBL pre-patterned membrane device is then loaded onto a TEM device holder (Figure 9.2a) and entered into the low-pressure ($< 10^{-8}$ Torr) chamber of a JEOL 2010F HRTEM at room temperature. The device is oriented on the holder such that the metallized side of the membrane faces away from and perpendicular to the beam source (i.e., it is face down). Using the standard imaging mode of the microscope with a $\sim 5 \text{ \AA}$ diameter electron beam, accelerating voltage at 200 kV, minimum convergent beam angle (“ α_3 mode” on a JEOL 2010F), magnification typically below $100,000\times$ and the beam current density below $\sim 10 \text{ pA/cm}^2$, the region of the initial metal to undergo TEBAL is located. Next, the magnification is increased to $\sim 1,000,000\times$, the beam is switched to maximum convergent beam angle (“ α_1 mode”) and is then condensed to its narrowest diameter ($< 1 \text{ nm}$) while situated slightly away ($\sim 10 \text{ nm}$) from the target region for optimizing the beam focus, alignment and stigmation correction. Once optimized, the beam appears on the imaging screen

as a small disk with a bright “caustic spot” at its center. The current density after optimization is ~ 50 pA/cm². Next, the beam is aimed at the desired pixels of the metal to be ablated. The user is actually able to see the ablating effect of the caustic spot on the metal in real time because of the low-intensity illumination of the beam surrounding this high-intensity center region. The time between exposing the metal to the condensed beam and the ablation is on the order of seconds, though the exact time required will depend on the metal being ablated and the microscope conditions. Ablation is initiated more easily at points of high surface energy (e.g., the edge of a wire). Ablation is carried out until the desired pattern is made and is then stopped by reducing the beam current density near the target material back to below ~ 10 pA/cm², either by moving the beam away from the target material or by leaving its position unchanged and reducing the intensity of the beam. The TEB alters both the metal and the silicon nitride substrate. However, the rate at which metal is ablated (~ 10 nm³/s) is much greater than the rate at which the substrate is affected and in most cases the changes in the nitride are negligible and not observable with TEM. While carving out the metal takes only a few seconds, it takes several minutes to drill a hole in a bare SiN_x membrane with a 200 keV beam. In some of the TEM images shown, the brighter (white) areas are regions where the TEB removed possible impurities from the surface, removed some of the nitride, or a combination of both.

9.4 More Examples

Figure 9.3 shows an image gallery of additional metal nanostructures (nanowires, nanochannels and nanogaps) made with TEBAL on SiN_x membranes. A ~ 40 -nm

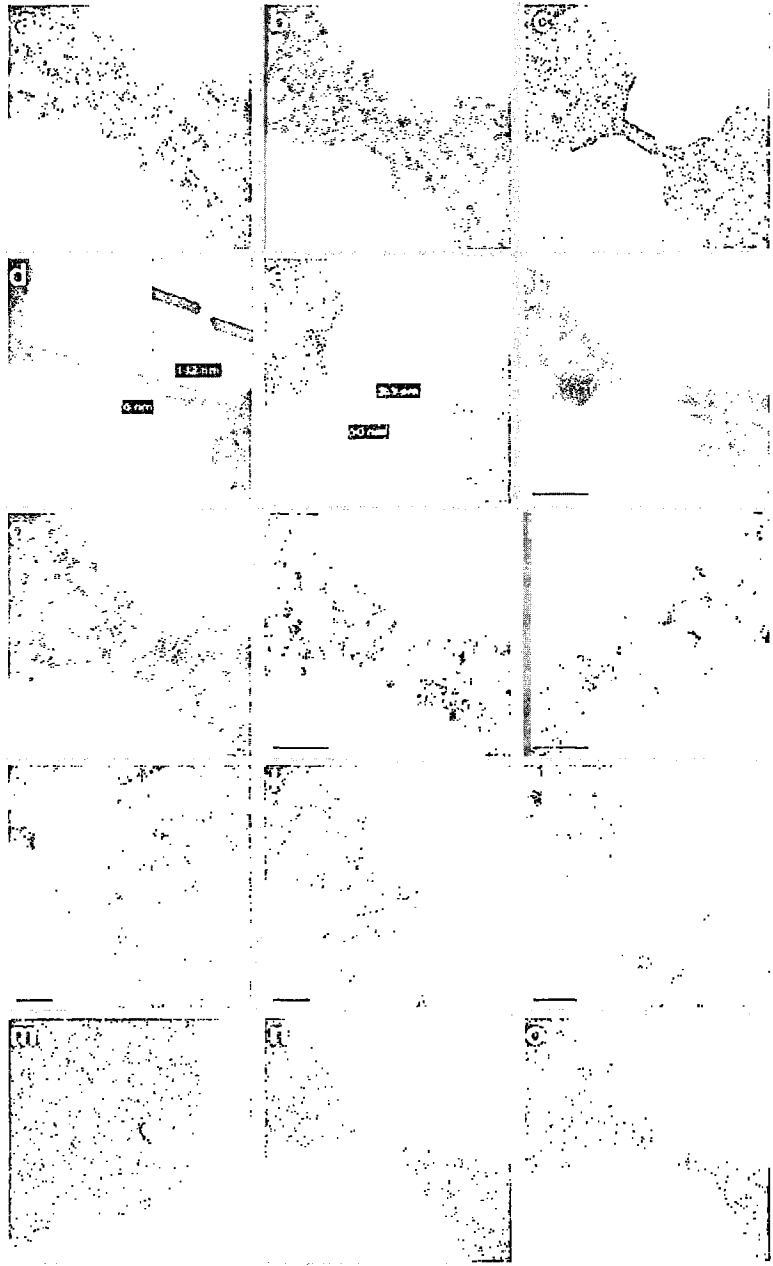


Figure 9.3: TEBAL example gallery. (a)-(c) TEBAL fabrication of a nanowire made of a Ni/Cr alloy (all scale bars = 20 nm). (d)-(f) Additional examples of Ni/Cr alloy nanowires. The width and length (W,L) of the nanowires in nanometers are (6, 132), (3.5, 50) & (13, 61), respectively (scale bars = 20 nm, 20 nm & 50 nm). (g) "Bottleneck" structure (scale bar = 20 nm) (h) Nanochannel \sim 7.8 nm wide. (scale bar = 50 nm) (i) Nanochannel 3.1 nm wide, \sim 85 nm long. (scale bar = 50 nm). (j)-(l) Three stages of "carving out" a Ni nanoparticle (all scale bars = 20 nm). (m) \sim 1.9 nm diameter nanohole drilled into Cr. (scale bar = 10 nm). (n)&(o), Au wire with narrow constriction before and after removing debris and making a clean 5 nm nanogap with TEBAL (scale bars = 20 nm).

long nanowire is shown at three stages of its formation by trimming down the two sides of a metal strip from \sim 60 to 12 nm (Figure 9.3(a-c)). Three additional examples of finished Ni/Cr nanowires with dimensions \sim 3.5 nm \times 50 nm, 6 nm \times 132 nm and 13 nm \times 61 nm are also shown (Figure 9.3(d-f)). Also shown is the fabrication of nanochannels \sim 3.1 to \sim 7.8 nm wide up to \sim 85 nm long (Figure 45g-k), a rod-like Ni nanoparticle, \sim 15 nm by \sim 54 nm, made by carving out two nanochannels (Figure 9.3(j-l)) and a nanohole \sim 1.9 nm in diameter drilled in Cr (Figure 9.3(m)). Figures 9.3(n-o) show two-stages of carving out and “cleaning” from debris a \sim 5.2-nm large nanogap in Au. Specifically, Figure 9.3(n) shows a 13-nm wide constriction in Au and the small Au nanoparticles on both side of the constriction. These nanoparticles were removed as the SiN_x surface was “cleaned” by ablation in Figure 9.3(o) while defining a clean nanogap and removing the nearby debris. This example illustrates a general use of TEBAL to quickly “correct” and “clean” the EBL-made patterns, thus increasing the yield of the standard EBL process.

9.5 Effect on Lattice Structure

For all of the metals that have been explored in this work (Ag, Ni, Cr, Al and Au), the ablation effect seems to stop almost immediately after the current density around the ablated area is reduced. Prior to TEB exposure, the metal is amorphous/polycrystalline. High-resolution imaging of the TEBAL process reveals that high-intensity TEB exposure first anneals an exposed region into a crystalline domain and continued exposure drives the ablation of the newly formed lattice resulting in complete removal of the atoms from the surface. Figure 9.4 shows the final stages of ablating a spot in a Ag film that has been locally annealed by brief exposure

to the high-intensity TEB. Figure 9.4c shows that an ablated spot and the lattice of the locally annealed surrounding region meet at a sharp edge. Additionally, the TEB seems to anneal any grain boundaries in the metal films that it encounters. In practice, the size of the structures that can be made with TEBAL does not appear to be limited by grain size.

9.6 Crystallization of Au

It is important to note that while all other metals demonstrated in this work can be nanosculpted into arbitrary patterns, Au reacts differently to the TEB. Instead of being removed from the substrate during TEBAL, Au atoms crystallize into robust lattice domains. This seems to be a general behavior for Au, at least on the nanoscale. As an example, Figure 9.5 shows the TEB-induced transition of an amorphous Au island, made by evaporating a thin (~ 1 nm) film of Au onto a SiN_x surface, to a single crystal.

This property of Au was exploited to make the nanogap in Figure 9.3(o) (and the nanogaps in Figure 9.11). The fabrication works by encouraging the formation of crystallization sites on either side of the narrow neck of Au (Figure 9.3(n)) so that upon sustained TEB exposure the atoms leave the neck region in favor of being incorporated into the growing crystalline contacts, forming the nanogap in the process. Figure 9.6 shows high resolution images of the formation of a Au nanogap with crystalline contacts. Formation of crystalline Au contacts has more recently been observed during electromigration under TEB exposure^[111].

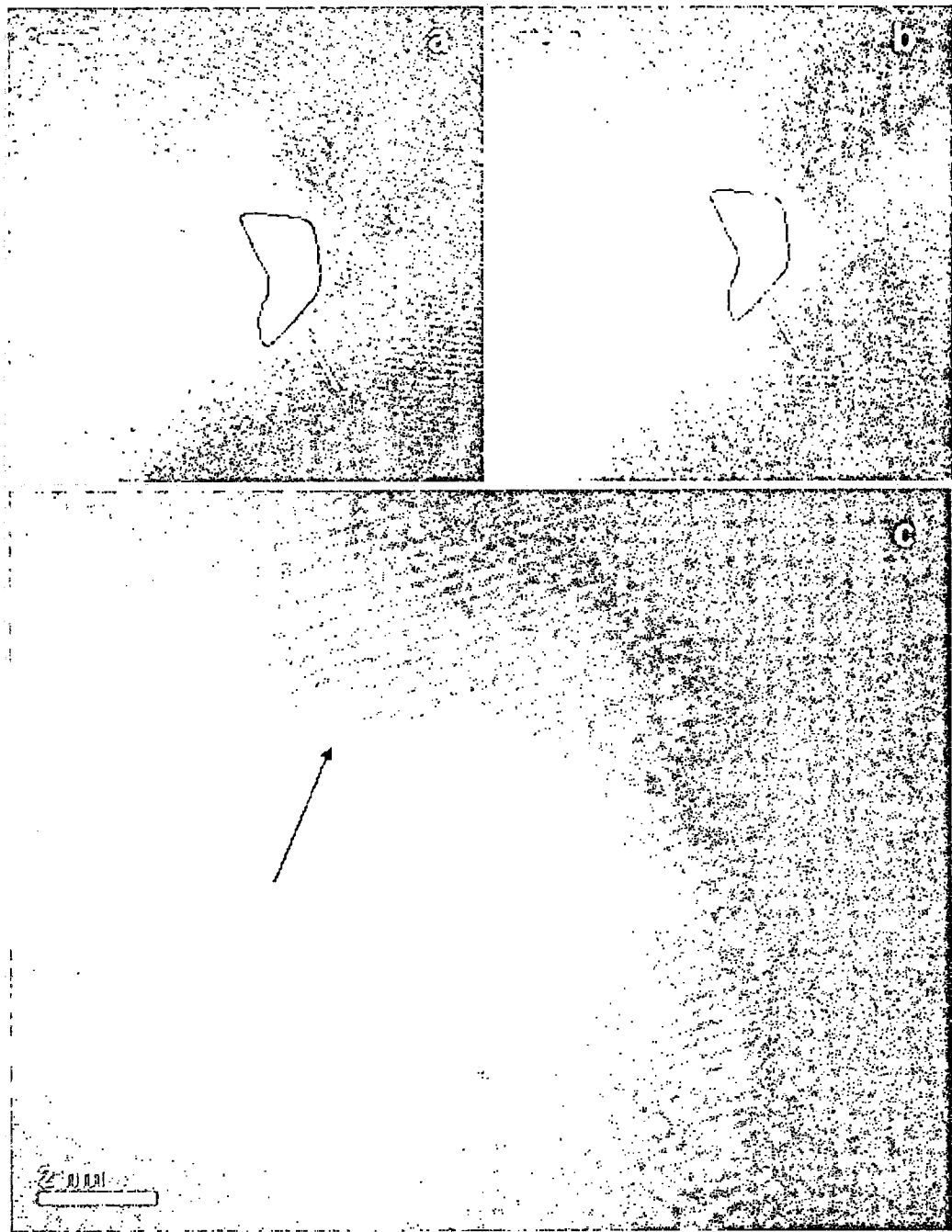


Figure 9.4: TEM images showing the ablation of Ag with TEBAL. (a) The edge of an Ag film after TEBAL was used to begin ablation at a 90 degree angle to the edge. The next “pixel” to be ablated is indicated for clarity. Note that it is crystalline due to having been partially exposed to the high-intensity TEB. (b) The same film after ablating the pixel. The Ag atoms in this region have been completely removed from the surface. (c) TEM image showing the sharp edge of an ablated spot made at a later point in the patterning of the Ag film. Lattice structure in the metal is preserved almost completely to the edge of the ablated spot (marked with arrow).

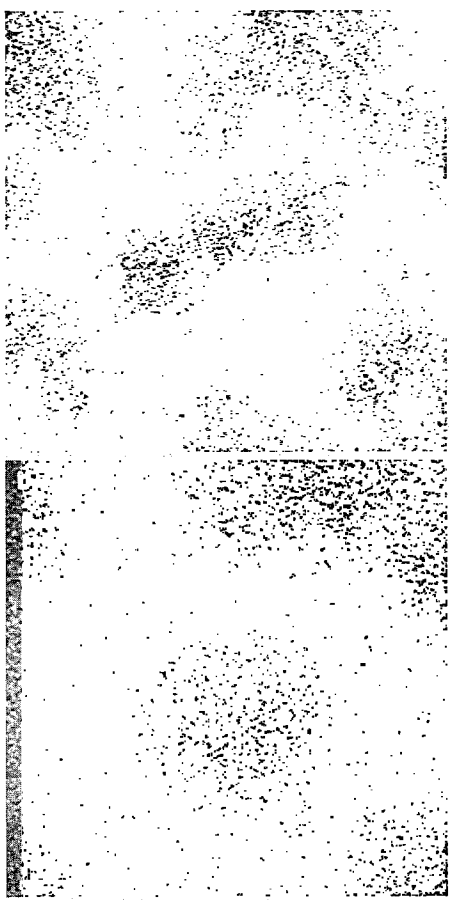


Figure 9.5: TEM images showing TEB-induced transition in Au from (a) amorphous to (c) crystalline due to beam exposure. Scale bars are 5, 5, 2 nm.

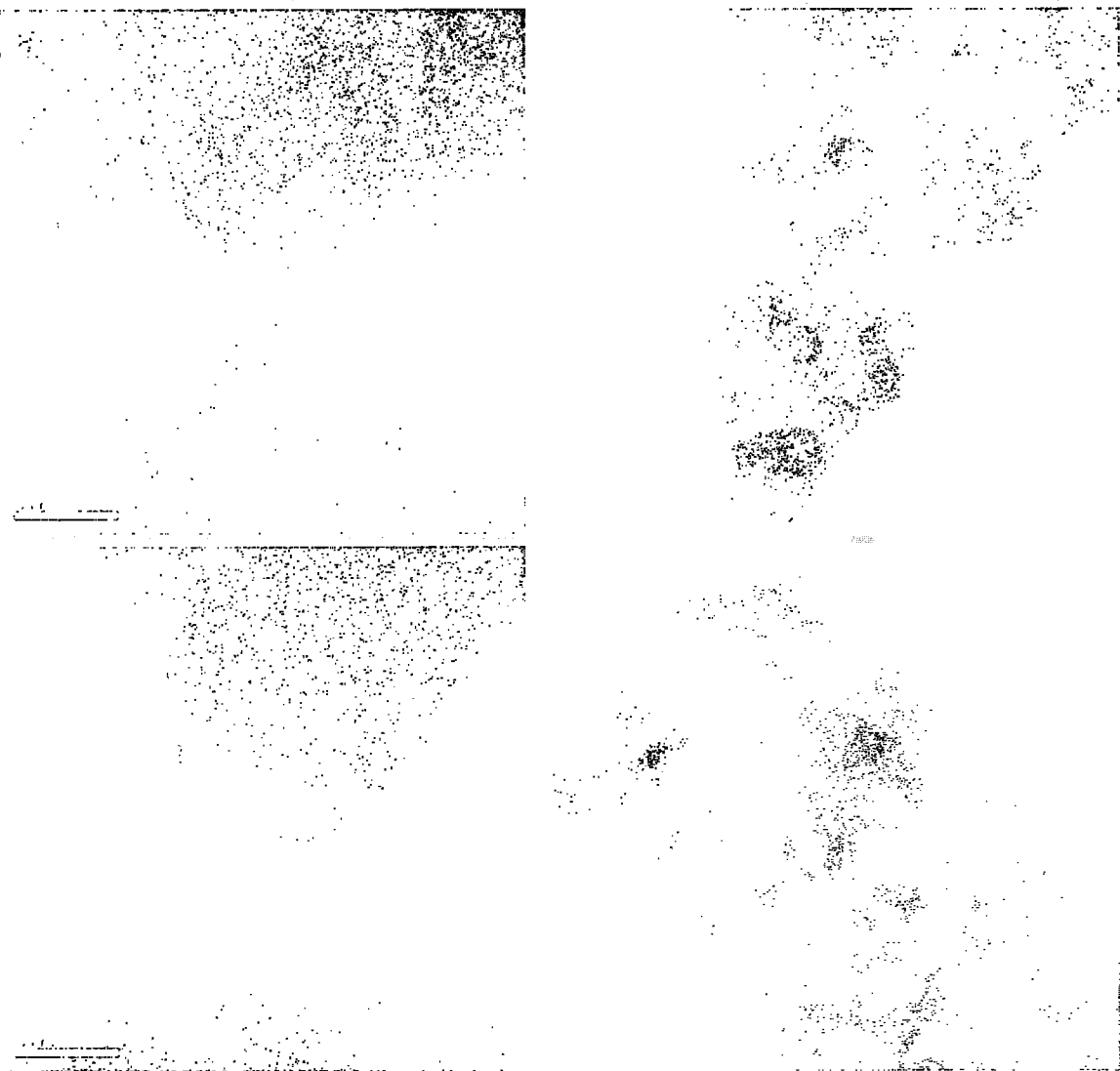


Figure 9.6: TEM images showing formation of Au nanogap. (a) Intermediate stage of Au atoms receding to crystalline contacts and (b) final ~ 5 nm nanogap. Note that the top contact is a faceted crystal with one vertex as the closest point to the opposing contact. (c) Zoom-out of the finished nanogap. This gap has a nanohole drilled into the substrate in the gap region.

9.7 Precision of the Technique

Illustrating the degree of control during the fabrication of an arbitrary pattern with sub-10 nm features, Figure 9.7 shows four steps towards making a pair of nanosculpted squares in a Ag film. These two neighboring squares are made by carving out 7 line segments, \sim 50-nm long and from \sim 3.5-nm to \sim 10-nm wide, and leaving two \sim 12-nm long constrictions, thus defining two square-like metal islands connected to the parent material. Importantly, this example demonstrates that with TEBAL, lines can be formed in one direction and then suddenly redirected at a right angle.

9.8 Device Measurement

For device performance, it is important to ensure that TEBAL itself does not contaminate the fabricated devices. If a silicon nitride membrane surface is contaminated prior to being loaded into the TEM chamber, then the TEB will typically cause the outgassed contaminant to recondense onto the membrane surface along the TEB's perimeter, forming a ring. To avoid this situation, recently EBL-processed devices are allowed to outgass in ambient conditions overnight or are cleaned with O₂ plasma before doing TEBAL. Alternatively, contaminants can be removed after TEBAL with a brief exposure to O₂ plasma.

To demonstrate that TEBAL-fabricated devices are of high quality and contamination-free, Figure 9.8 presents current-voltage (*I-V*) measurements of a circuit that is open due to a TEBAL made nanogap and one that is closed by a TEBAL made nanowire. Figure 9.8(a) shows the result of measurement of the \sim 3.5-nm wide by 50-nm long nanowire shown in the inset (and in Figure 9.3(e)). Two-terminal electrical

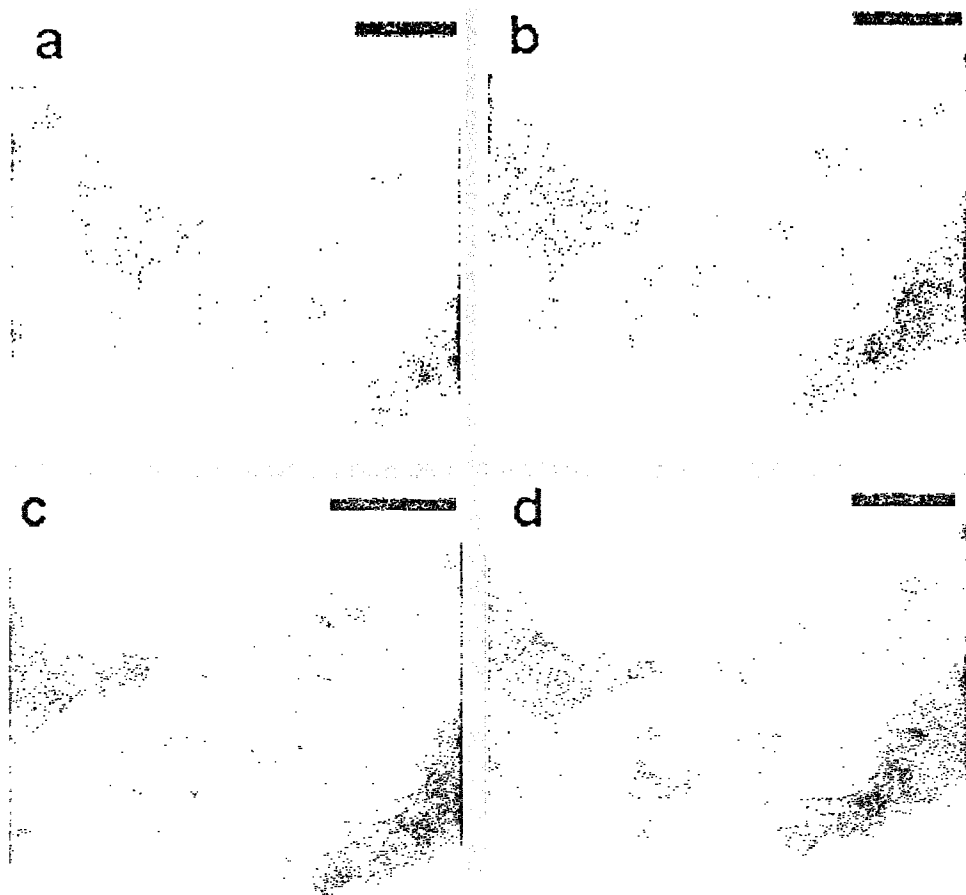


Figure 9.7: Four steps towards making a pair of squares in Ag. (a) First features are composed of four joint line segments, each at right angles to its neighbor. (b) Addition of line segment at 90 degrees to the right most line segment. (c) Right square is defined and left connected to the parent material by a short nanowire. (d) Left square is defined and left connected to the parent material by a short nanowire. All scale bars = 50 nm.

characterization of this nanowire under vacuum (pressure $< 10^{-6}$ Torr) from room temperature down to ~ 4 K displayed Ohmic resistance of ~ 30 k Ω . The resistance was insignificantly dependent on temperature, changing less than 1% over the measured range. Reduced sensitivity to temperature with reduced wire diameter has been reported by Natelson *et al.*^[112] where the smallest wire studied was ~ 5 nm. This wire differs from these previous studies because of the absence of contact resistance to the leads, which may contribute to the role of temperature dependence. Additionally, the short length of this wire (~ 50 nm) makes it unlikely that post-fabrication contacting would have been successful. Figure 9.8(b) shows the result of I - V measurement of the ~ 2.5 nm nanogap shown in the inset (and in Figure 9.11(c)).

The source-drain leakage current, for this device was ~ 20 fA at 100 mV at 77 K. The current sensitivity of this device is therefore high, allowing the study of even highly insulating nanostructures. Considering that only the extremely small nanogap region of the surface need be contaminated in order to short the circuit, and that this region is where contamination is most likely to occur (i.e., where the TEB spends most time during the fabrication), such a low current magnitude suggests that contamination from the TEM environment is negligible.

9.9 Potential Application in Superconductivity Research

The geometrical flexibility and the ease of electrical contacting makes the TEBAL-fabricated wires especially interesting for studying the effects of wire size and shape on conductivity in normal and superconducting wires. In Al nanowires for example,

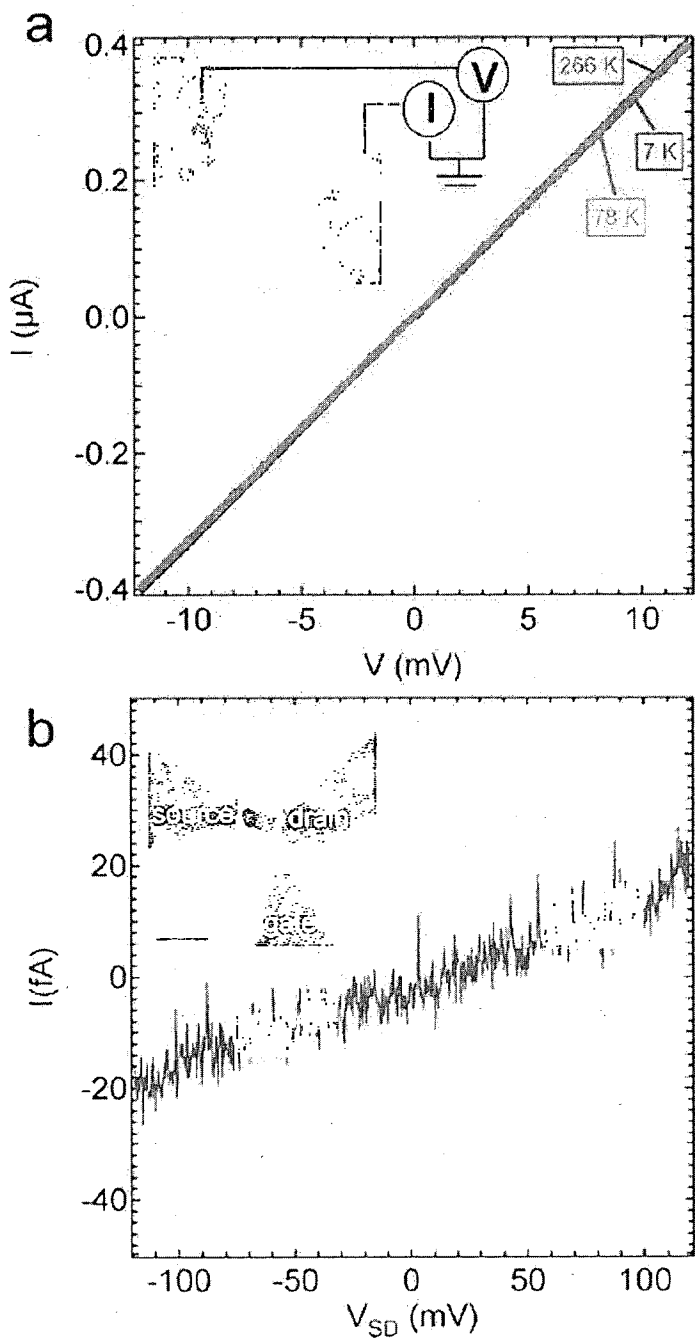


Figure 9.8: Device characterization (a) Current-voltage (I-V) measurements of 3.5 nm wide nanowire shown in the inset. Data shown for measurement temperatures 266, 78 and 7 K. Inset: TEM image of the nanowire (scale = 20 nm). (b) Background source-drain current-voltage signal of the 3-terminal NGFET shown in the inset. Inset: TEM image of the device (scale = 50 nm).

superconductivity breaks down for wire widths below ~ 10 nm.^[106] Tailoring wire shapes would allow the creation of modulated local regions of normal and superconducting behavior, and in turn allow the creation of superconducting - normal (S-N) and superconducting-insulating (S-I) modulated wires for studies of quantum phase transitions.^[103-107]

TEBAL is well suited for the fabrication of multi-terminal electronic devices where small, nm-scale separation between metal electrodes is required. In addition to a simple geometry with source and drain electrodes, more complicated geometries with multiple electrodes or nearby gate electrodes for local control can be easily fabricated with this technique. Fabrication can be also performed on the back side of the silicon nitride membranes to fabricate, for example, a global back gate. Examples of 3, 4 and 8-terminal devices are shown in Figure 9.8, Figure 9.9, and Figure 9.10. Figure 9.9(a-d) shows four steps in making a four-terminal nanogap field effect transistor (NGFET) out of two intersecting Ag lines. The final device consists of two electrodes forming a ~ 2.3 -nm large nanogap and two gate electrodes ~ 19 and ~ 56 nm away from the nanogap region.

Figure 9.10 shows an 8-terminal TEBAL-fabricated device consisting of eight Ni/Cr electrodes defined along a perimeter of a circle with radius ~ 15 nm. The device was formed by cutting lines out of one continuous region. The cutting rate was ~ 1 nm/s (in the direction of the line). The large number of electrodes allows this device to be used to generate a variety of electromagnetic fields for trapping and manipulating particles. Viewed another way, these electrodes form eight neighboring nanogaps, all within a ~ 30 nm diameter region.

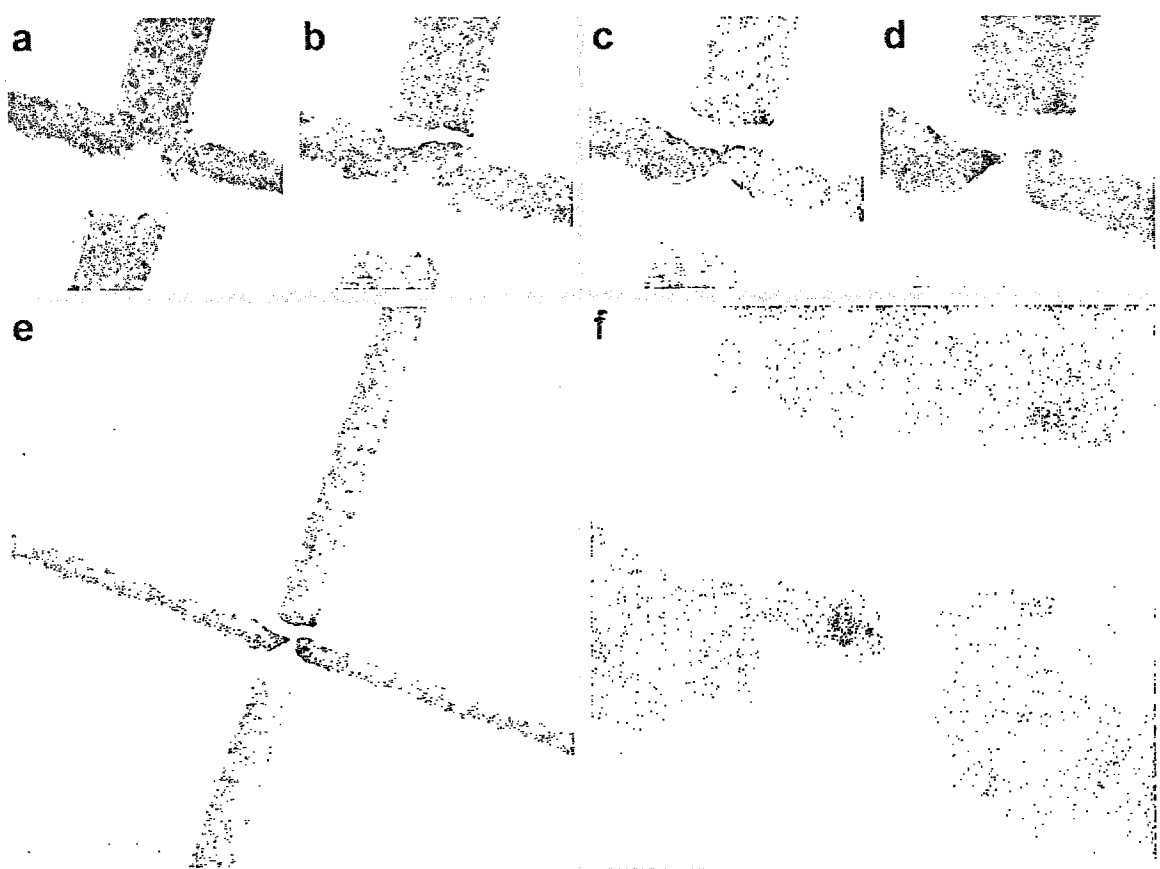


Figure 9.9: Making a 4-terminal nanogap field effect transistor (NGFET) out of two intersecting Ag wires. (a)-(d) Ag is ablated until a nanogap is defined with gate electrodes on both of its sides (scale bars = 50, 50, 50, 20 nm). (e) Large scale view of the completed 4-terminal NGFET (scale bar = 200 nm). (f) Zoomed-in view of nanogap and upper gate electrode (scale bar = 20 nm).

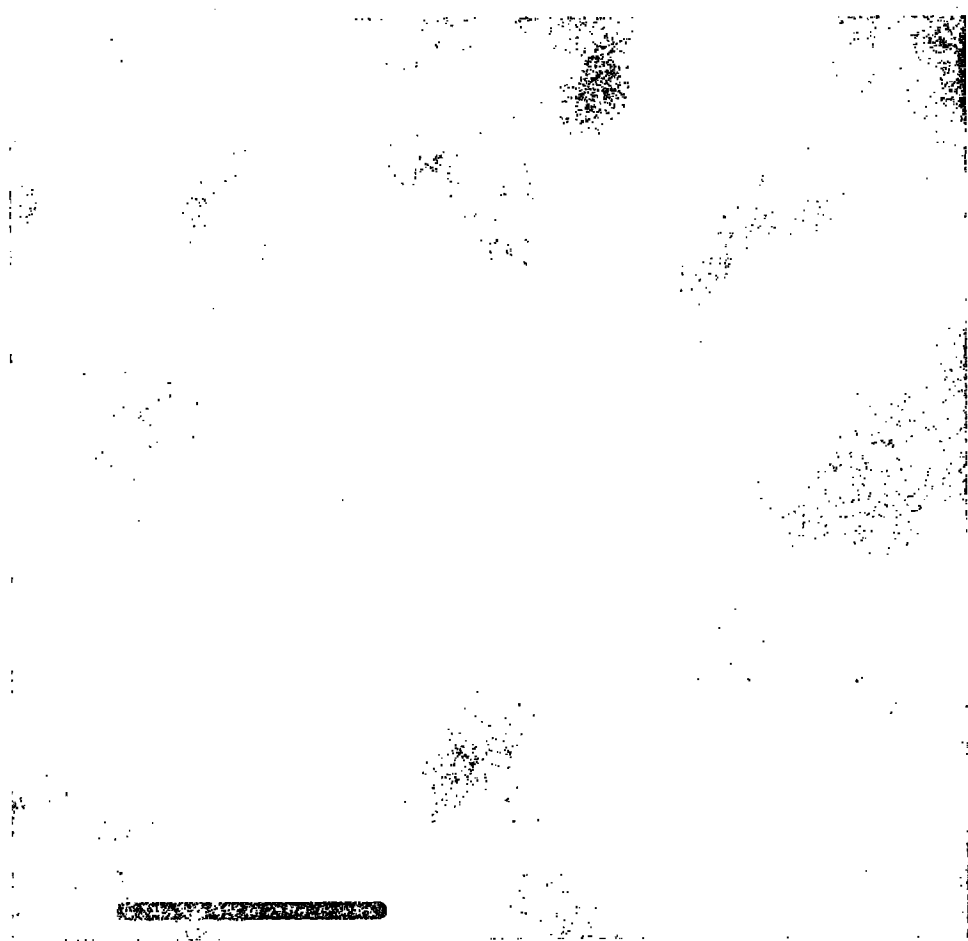


Figure 9.10: 8-terminal device fabricated from Ni/Cr. (scale bar = 20 nm).

9.10 Application to DNA analysis

As yet another application, a nanoscale object as small as ~ 30 nm could be electrically characterized along different directions to investigate potential anisotropies.

Figure 9.11 shows three 3-terminal devices, all fabricated with TEBAL on the same $\sim 50 \times 50 \mu\text{m}^2$ membrane window (Figure 9.11 (e)). Each device consists of a nanogap (~ 1.5 nm, 2 nm and 2.5 nm) and gate electrode (~ 40 nm from each nanogap). Additionally, a nanohole has been drilled into the membrane exactly inside each of the nanogap regions (Figure 9.6). This type of device may be used as a NGFET for a range of molecular electronic applications. Furthermore, this example demonstrates the reproducibility of TEBAL fabrication *by hand*.

Several groups have demonstrated the fabrication of nanoholes in insulating membranes by using TEBs^[113–116] and focused ion beams (FIB).^[117] Nanoholes have been useful for manufacturing single-molecule detectors and have been used to study translocation of DNA molecules^[118–122] and carbon nanotubes^[123] by measuring ionic current between macroscopic electrodes as molecules pass through the nanohole. These and other advancements suggest possible applications of nanoholes, to DNA size determination and sequencing. As mentioned above, the devices shown in Figure 9.11 each have a nanohole spanning their nanogap. Figure 9.12 shows several stages of making a similar nanohole-nanogap geometry in a Ag nanogap. By applying a potential difference across these electrodes, electrical current (or capacitance) could be monitored to characterize a molecule during its translocation through the nanohole (illustrated in Figure 9.11(f)). Lagerqvist *et al*^[124] have recently performed molecular dynamics and quantum-mechanical current calculations for this situation and calculate the difference in electrical current signals of different base pairs to be

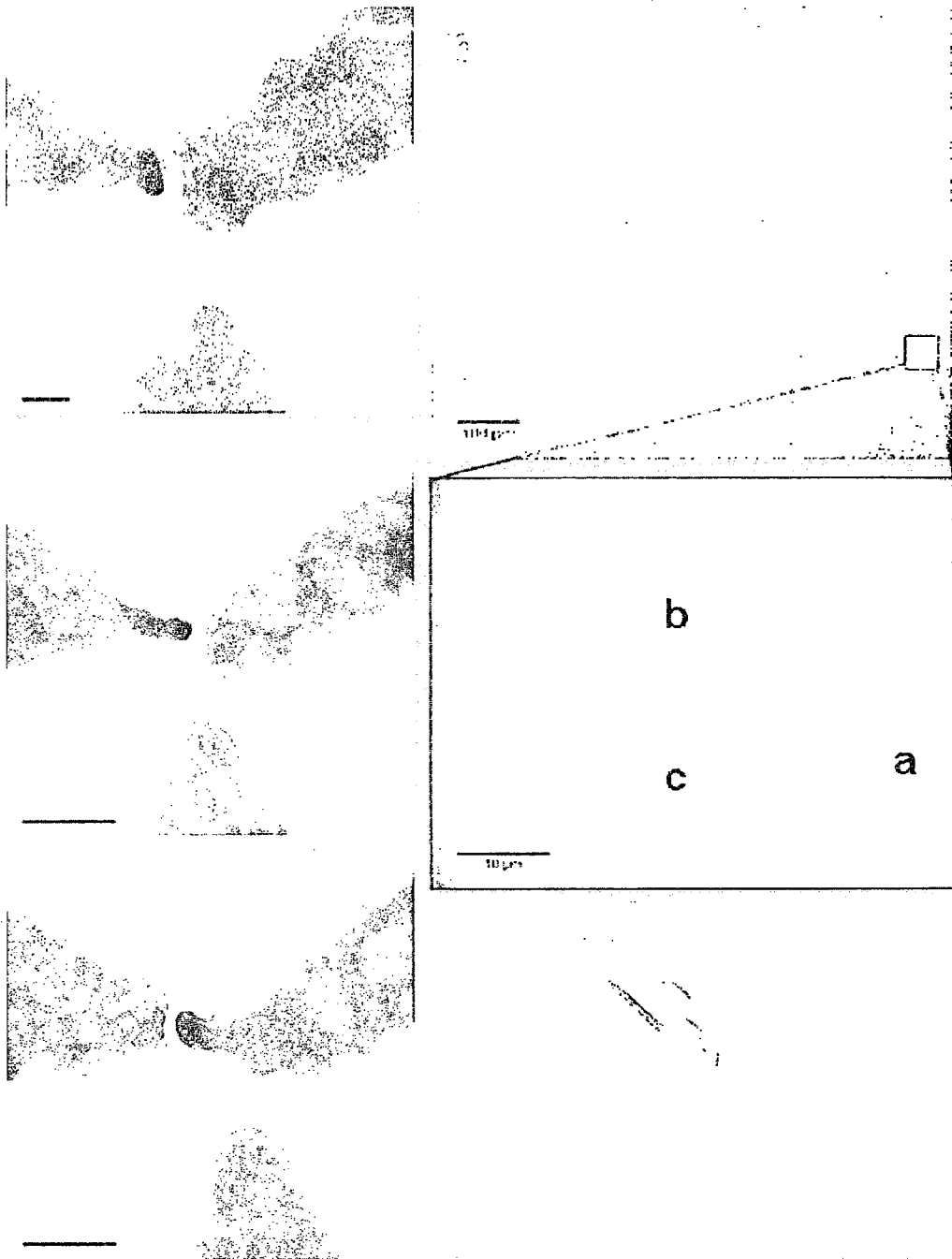


Figure 9.11: Devices for molecular detection and analysis. (a)-(c) Source, drain and gate devices with nanohole for molecular translocation. (scale bars = 20 nm, 50 nm & 50 nm) (d) Optical micrograph of the full device containing the three molecular "analyzers". The membrane window is seen in the lower right corner and has wires running from it out to large contact pads. (scale bar = 100 μ m) (e) Optical micrograph of the membrane

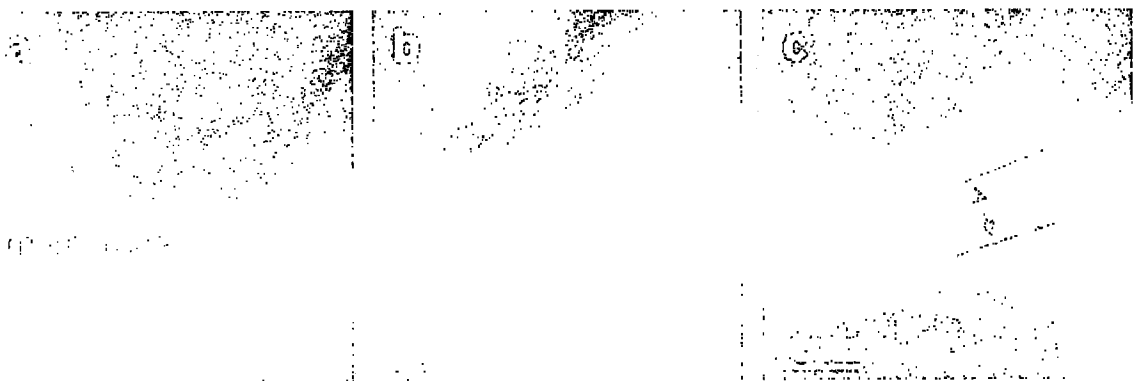


Figure 9.12: A ~ 5 nm nanopore is made in the nanogap region that was formed by removing Ag with the electron beam

rather large, of the order of 0.1 nA. Depending on the electrode thickness, a smaller or larger fraction of a molecule such as DNA could be electrically characterized. The thickness of metal electrodes can be reduced by ablation with sub-nanometer precision. This could further increase the sensitivity and lower the detection limit of these devices. However promising, the feasibility of this approach will be ultimately determined by future biophysics experiments.

9.11 Automation

All of the structures presented in this chapter were prepared “by hand” in the sense that a human user shifted the beam while watching the ablation in real-time. Computer control should offer an even higher degree of precision than what has been demonstrated here and can therefore produce highly intricate patterns over a wide membrane area. Computerized automation is possible by measuring the current density of the beam (Figure 9.2(a)) during TEBAL. Once the current density of the beam is measured on an un-metallized region of the membrane, later comparisons of real-time values to this reference value are used to inform the computer of whether or not the beam is on or off a metal region. This fact can be used to have the automated system find the metal regions on the membrane. By running into the metal several times with slight displacements, the system finds an axis parallel to the metal edge and can carry out ablation with respect to this known axis.

9.12 Conclusions

The results in this chapter demonstrate the precision, versatility and reproducibility of metal nanosculpting by controlled atom ablation via the imaging beam of a

HRTEM for the manufacturing of ultra-small metal devices on insulating silicon nitride membranes. The applications of TEBAL include the areas of nanoelectronics, superconductivity, molecular translocation, nanofluidics and atom/nanoparticle manipulation with highly localized electromagnetic fields. TEBAL is expected to work on a wider class of materials than has been demonstrated here and, as an example, nanosculpting of graphene is demonstrated in the next chapter. Future work involving simultaneous in situ fabrication and measurement of test structures may provide additional insight to the mechanisms at work during TEBAL in addition to revealing fundamental science of the fabricated structures.

Chapter 10

Electron beam nanosculpting of suspended graphene sheets

10.1 Introduction

Graphene, a two-dimensional carbon crystal, has been the focus of intense research since techniques were developed to extract it from graphite in the form of multi-layers^[125] and single layers.^[126] Graphene-based devices measured on substrates have revealed an impressive set of exotic electronic and optical properties with promising applications.^[127–131] Furthermore, suspended graphene has been shown to have exceptionally high electron mobilities^[132] and high strength.^[133,134] Due to its single-atom-thickness and the relatively low atomic number of carbon, suspended graphene is emerging as powerful platform for transmission electron microscopy (TEM).^[134–136] In addition to serving as a near-ideal substrate for TEM analysis,^[137] it has been shown that electron-beam-induced-deposition (EBID) of carbon onto graphene can be achieved with high accuracy in a TEM.^[138]

In this chapter, it is demonstrated that suspended multi-layer graphene sheets can be controllably nanosculpted with few-nanometer precision by ablation via focused electron-beam irradiation in a TEM at room temperature. Examples include

nanopores, nanobridges and nanogaps. These examples and other nanometer-scale patterns of arbitrary design may prove useful in graphene-based electronic and mechanical applications. For instance, fabricating narrow constrictions in graphene layers is of interest for electronic property engineering.^[139–147] Structures made by electron-beam irradiation are stable and do not evolve over time. Furthermore, the extensive removal of carbon does not introduce significant long-range distortions of the graphene sheet. Specifically, the sheets do not begin to fold, wrinkle, curl, or warp out of the focal plane during cutting.

10.2 Methods

Graphene sheets were extracted from graphite by mechanical exfoliation^[126] on \sim 300 nm SiO₂ substrates coated with \sim 100 nm of PMMA and then transferred to a suspended \sim 50 nm-thick suspended SiN_x membrane substrate.^[81] Prior to transfer, arrays of \sim 1 μ m square holes were patterned into the SiN_x membranes by exposing the surface to a SF₆ reactive ion etch through a resist mask made by electron beam lithography. In order to transfer graphene sheets onto the SiN_x membranes, a method was used inspired by the technique developed by Meyer *et al.*^[138] for transferring graphene to TEM-compatible holey carbon grids. After locating graphene sheets on the PMMA surface with an optical microscope, a drop of isopropanol is added to the surface. A SiN_x membrane substrate is then placed onto the drop over a region containing graphene sheets, with its surface facing the PMMA surface. As the isopropanol evaporates, its surface tension brings the two surfaces into a close contact, which is further improved by heating at \sim 200 C for \sim 5 minutes. Finally, the PMMA is dissolved in acetone, which releases the graphene sheets on the PMMA

side and allows them to transfer and stick to the SiN_x membrane substrate.

Graphene sheets suspended over a hole in the SiN_x membrane were identified in a TEM (JEOL 2010F operating at 200 kV). The number of graphene layers in a sheet could often be determined by imaging the edge of a folded region,^[135] in a manner similar to counting the number of tubes in a multi-walled nanotube. Samples in this work ranged in thickness roughly from 1 - 20 graphene layers, though the majority of graphene sheets used in this work were composed of ~ 5 layers. Using a method described previously, arbitrary patterns were created in the graphene sheets by increasing the TEM magnification to $\sim 800,000\times$, condensing the imaging electron beam to its minimum diameter, ~ 1 nm, and moving the beam position with the condenser deflectors (see Ch. 9). To avoid EBID of carbon, likely to occur for a spot-mode beam setting, nanosculpting was performed with the beam at cross-over in a diffusive mode. With the beam at cross-over, the current density measured on the imaging screen was ~ 50 pA/cm² which, after accounting for magnification, corresponds to an estimated ~ 0.3 pA/nm² at the sample position. The exposure of the graphene sheets to the beam was ~ 1 s/nm². All of the structures shown were made at room temperature.

10.3 Results and Discussion

Figures 10.1(a-c) show TEM images of a graphene sheet before and after creating a ~ 3.5 nm diameter nanopore by irradiating this spot with the condensed electron beam for ~ 5 s. It was also observed that very brief (~ 500 ms) exposure of graphene sheets to the condensed electron beam can be used to create a partial nanopore by

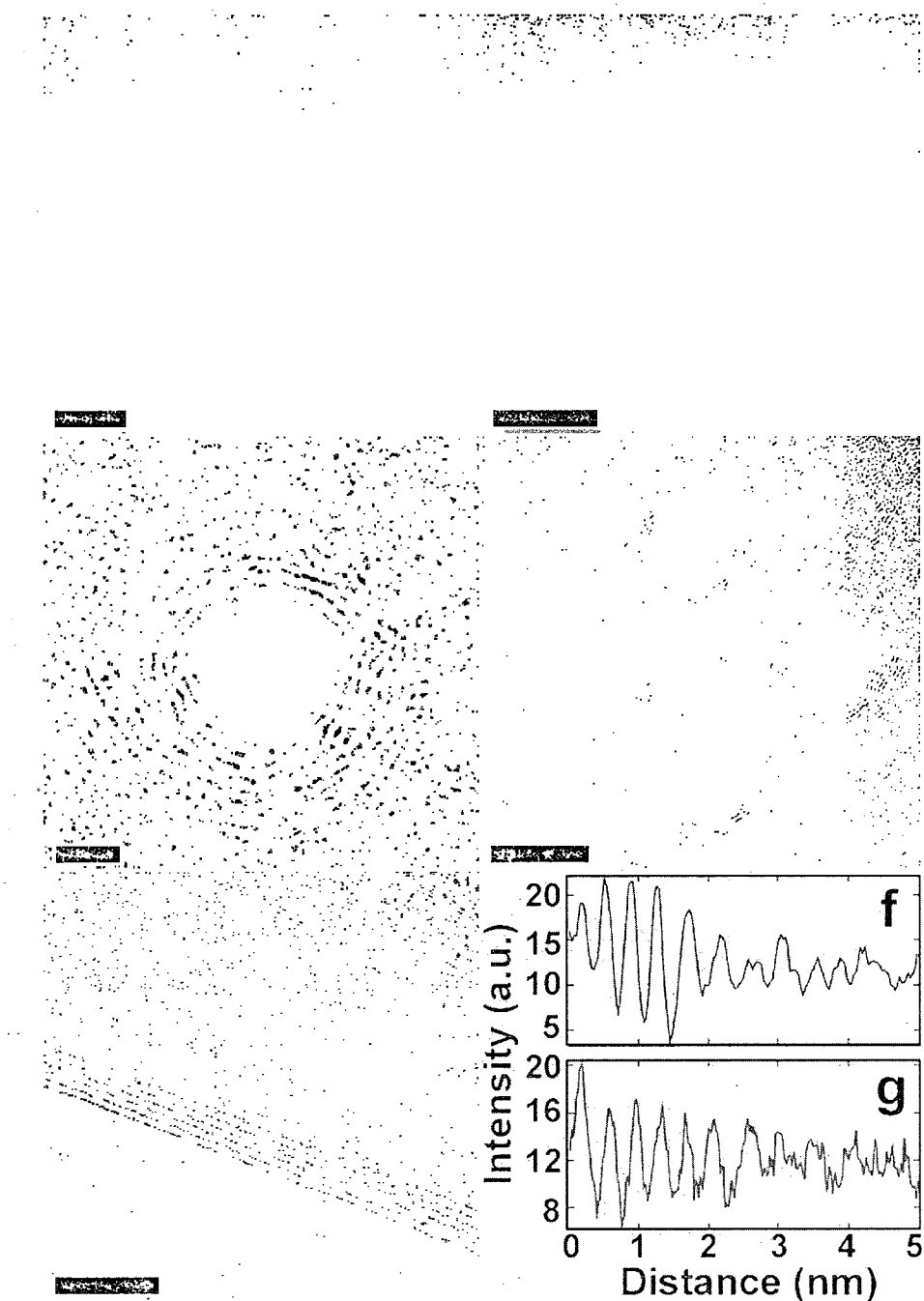


Figure 10.1: TEM images of a suspended graphene sheet is shown (a) before and (b) after a nanopore is made by electron beam ablation. (c) Higher magnification image of the nanopore. (d) Multiple nanopores made in close proximity to each other. (e) Folded edge of a graphene sheet showing lines corresponding to layer number. These lines are similar to those seen around the nanopores (Scale bars are 50, 50, 2, 10, 5 nm). (f) Average of intensity cross-sections taken along 6 different radial directions of the nanopore in (c), each starting at the edge and proceeding radially outward. (g) Average of 6 intensity cross-sections of the graphene sheet in (e), each taken perpendicular to and starting at the sheet edge.

removing a fraction of the graphene layers, while leaving other layers intact. A single nanopore is the simplest structure that can be made by ablation, yet nanopores have proven extremely valuable in studies of molecular translocation, DNA in particular.^[148] Given that graphene is the thinnest possible membrane yet at the same time structurally robust^[133] and impermeable,^[149] nanopores in graphene sheets may be useful for achieving significant resolution enhancement in molecular translocation measurements. As shown in Figure 10.1(d), multiple nanopores can be made in close proximity to each other, indicating that large arrays of closely packed nanopore arrays can be achieved.

Since the average irradiation exposure time per nanopore is on the order of seconds, serial processing is not prohibitively time intensive and large arrays or more complicated geometries can be made quickly. Moreover, parallel fabrication with multiple electron beams would allow for substantial scalability.

All of the nanopores that have been made have a concentric ring-like structure extending several nanometers away from their edges. This ring-like structure, evident in Figure 10.1(c,d), bears a close resemblance to the dark lines often observed at the edge of a folded graphene sheet, an example of which is shown in Figure 10.1(e). The orientation of a folded graphene layer's edge is locally parallel to the TEM beam and consequently each layer in a folded graphene sheet introduces a dark line along the edge of the fold,^[135] similar to what is seen at the radial edges of a multi-walled carbon nanotube. Intensity cross-sections (Figure 10.1(f,g)) obtained from the images of the folded graphene sheet (Figure 10.1(c)) and nanopore (Figure 10.1(d)) reveal an average spacing between dark lines of 0.38 ± 0.02 nm and 0.39 ± 0.02 nm, respectively. These values are equivalent within the error introduced by finite TEM resolution and are close to the inter-layer distance of HOPG (~ 0.34

nm). These observations suggest that irradiation can induce coordinated inter-layer bonding between freshly exposed layer edges, leading in this case to an “inverted-onion”-like structure.^[150] Irradiation of carbon systems has been previously shown to be capable of inducing a variety of structural changes^[151] and these results demonstrate that graphene sheets can provide a valuable initial system for deriving carbon morphologies.

Figure 10.2(a) shows two parallel \sim 6 nm wide lines, i.e., regions where graphene has been removed, separated by \sim 25 nm. Starting with these lines, additional focused irradiation was used to gradually increase the lines’ widths until their separation was reduced to \sim 5 nm, resulting in a “nanobridge” (Figure 10.2(b,c)). Although the final nanobridge is highly crystalline (Figure 10.2(c)), the extensive exposure to irradiation may have induced significant inter-layer rebonding and atomic restructuring within individual layers. Nanobridges can be cut with the TEM beam to create a gap (Figure 10.2(d)) with initial size less than a nanopore diameter but quickly increasing with continued irradiation. In the regions near the cut, irradiation induces morphological changes of the crystalline structure and, in particular, the cut ends close completely, similar to fullerene capping observed for irradiated nanotubes.^[151] Such carbon-based point contacts and nanobridges directly connected to a larger graphene structure may find use in mechanical and electrical applications. Furthermore, nanosculpting of graphene sheets is not limited to straight lines. An example of the geometrical flexibility that is possible with nanosculpting is shown in Figure 10.3.

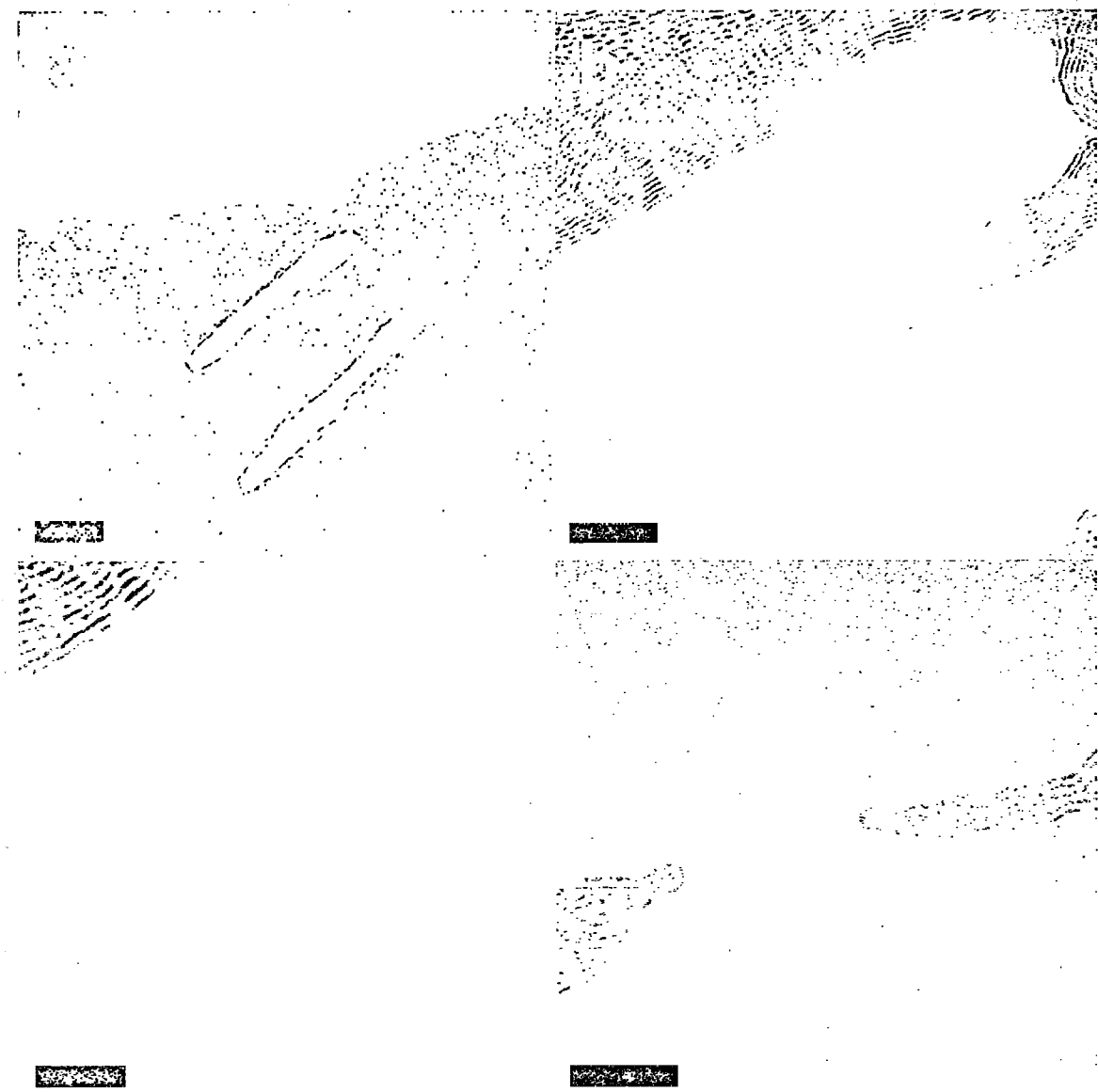


Figure 10.2: (a) Two ~ 6 nm lines cut into a graphene sheet. (b) Electron irradiation is continued to create a ~ 5 nm wide bridge. (c) Higher resolution of the bridge shows clear atomic order. (d) Small gap opened in the nanobridge by additional electron irradiation. The cut ends are closed. (Scale bars are 20, 10, 5, 5 nm).

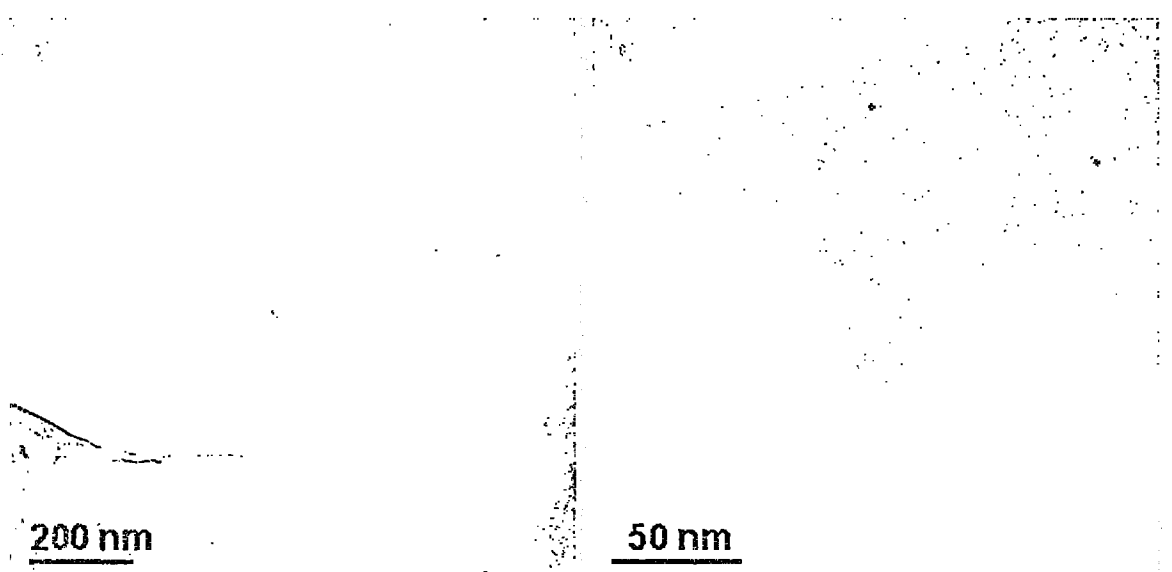


Figure 10.3: Demonstration of the arbitrary patterns that can be made in graphene sheets.

10.4 Conclusion

It has been demonstrated that suspended graphene sheets can be controllably nanosculpted with electron-beam irradiation. The ability to introduce features into suspended graphene sheets by electron-beam-induced cutting and reshaping with high spatial resolution expands their value as TEM compatible platforms and offers a route to fabricating graphitic structures for potential use in electrical, mechanical and molecular translocation studies.

Chapter 11

Conclusions

Electronic properties of semiconducting nanocrystal (NC) arrays have been revealed by current-voltage characterization and charge imaging. Correlation of these results with high-resolution transmission electron microscopy (HRTEM) enabled new insights into the role of NC array structure in transport behavior. CdSe NC arrays display photo-currents at low temperature. The addition of a small percentage of Au NCs into the CdSe NC array increases room temperature photo-conductivity by orders of magnitude. CdSe nanorod (NR) arrays display significantly higher dark-current at room temperature, compared to CdSe NC arrays, even for films just one mono-layer thick. History effects influence transport results in CdSe NC arrays, but this can be controlled for use as reliable memory technology. PbSe NC arrays are very insulating, even when highly ordered between electrodes. Small currents were only detectable through a few-PbSe NC array using a nanogap measurement device. Mild annealing increases the conductivity of PbSe NC arrays to the point where significant charging can be observed using electrostatic force microscopy (EFM). Correlation of these charge images with HRTEM revealed that annealing reduces the spacing significantly for multi-layers but not nearly as much for mono-layers, which explains the low conductivity observed for mono-layers. The HRTEM compatibility

of the devices used for NC transport measurements led to the discovery of two new nanofabrication techniques: one for making HRTEM-compatible nanogaps using a standard electron beam lithography system and the other for making a variety of nanostructures using the imaging beam of a HRTEM.

Bibliography

- [1] A. Alivisatos, "Perspectives on the physical chemistry of semiconductor nanocrystals," *Journal of Physical Chemistry*, vol. 100, no. 31, pp. 13226–13239, 1996.
- [2] A. Alivisatos, "Semiconductor clusters, nanocrystals, and quantum dots," *Science*, vol. 271, no. 5251, p. 933, 1996.
- [3] V. Klimov, *Semiconductor and metal nanocrystals: Synthesis and electronic and optical properties*. CRC Press, 2004.
- [4] W. Wilson, P. Szajowski, and L. Brus, "Quantum confinement in size-selected, surface-oxidized silicon nanocrystals," *Science*, vol. 262, no. 5137, pp. 1242–1244, 1993.
- [5] C. Murray, C. Kagan, and M. Bawendi, "Synthesis and characterization of monodisperse nanocrystals and close-packed nanocrystal assemblies," *Annual Review of Materials Science*, vol. 30, no. 1, pp. 545–610, 2000.
- [6] R. Rossetti, J. Ellison, J. Gibson, and L. Brus, "Size effects in the excited electronic states of small colloidal CdS crystallites," *The Journal of Chemical Physics*, vol. 80, p. 4464, 1984.

- [7] D. Norris, A. Efros, M. Rosen, and M. Bawendi, "Size dependence of exciton fine structure in cdse quantum dots," *Physical Review B*, vol. 53, no. 24, p. 16347, 1996.
- [8] D. Norris, A. Sacra, C. Murray, and M. Bawendi, "Measurement of the size dependent hole spectrum in cdse quantum dots," *Physical Review Letters*, vol. 72, no. 16, pp. 2612–2615, 1994.
- [9] M. Bawendi, W. Wilson, L. Rothberg, P. Carroll, T. Jedju, M. Steigerwald, and L. Brus, "Electronic structure and photoexcited-carrier dynamics in nanometer-size CdSe clusters," *Physical Review Letters*, vol. 65, no. 13, pp. 1623–1626, 1990.
- [10] M. Steigerwald and L. Brus, "Synthesis, stabilization, and electronic structure of quantum semiconductor nanoclusters," *Annual Review of Materials Science*, vol. 19, no. 1, pp. 471–495, 1989.
- [11] S. Coe-Sullivan, W. Woo, J. Steckel, M. Bawendi, and V. Bulovic, "Tuning the performance of hybrid organic/inorganic quantum dot light-emitting devices," *Organic Electronics*, vol. 4, no. 2-3, pp. 123–130, 2003.
- [12] M. Schlamp, X. Peng, and A. Alivisatos, "Improved efficiencies in light emitting diodes made with cdse (cds) core/shell type nanocrystals and a semiconducting polymer," *Journal of Applied Physics*, vol. 82, p. 5837, 1997.
- [13] S. Kim, G. Markovich, S. Rezvani, S. Choi, K. Wang, and J. Heath, "Tunnel diodes fabricated from cdse nanocrystal monolayers," *Applied Physics Letters*, vol. 74, p. 317, 1999.

- [14] W. Huynh, J. Dittmer, and A. Alivisatos, "Hybrid nanorod-polymer solar cells," *Science*, vol. 295, no. 5564, pp. 2425–2427, 2002.
- [15] W. Huynh, X. Peng, and A. Alivisatos, "Cdse nanocrystal rods/poly (3-hexylthiophene) composite photovoltaic devices," *Proceedings of the Electrochemical Society*, pp. 99–11, 1999.
- [16] R. Wang, J. Feser, J. Lee, D. Talapin, R. Segalman, and A. Majumdar, "Enhanced thermopower in pbse nanocrystal quantum dot superlattices," *Nano Letters*, vol. 8, no. 8, pp. 2283–2288, 2008.
- [17] D. Oertel, M. Bawendi, A. Arango, and V. Bulovic, "Photodetectors based on treated cdse quantum-dot films," *Applied Physics Letters*, vol. 87, p. 213505, 2005.
- [18] M. Bruchez Jr, M. Moronne, P. Gin, S. Weiss, and A. Alivisatos, "Semiconductor nanocrystals as fluorescent biological labels," *Science*, vol. 281, no. 5385, p. 2013, 1998.
- [19] P. Alivisatos, "The use of nanocrystals in biological detection," *Nature Biotechnology*, vol. 22, pp. 47–52, 2004.
- [20] M. Fischbein and M. Drndic, "Cdse nanocrystal quantum-dot memory," *Applied Physics Letters*, vol. 86, p. 193106, 2005.
- [21] D. Awschalom, D. Loss, and N. Samarth, *Semiconductor spintronics and quantum computation*. Springer, 2002.
- [22] M. Ouyang and D. Awschalom, "Coherent spin transfer between molecularly bridged quantum dots," *Science*, vol. 301, no. 5636, pp. 1074–1078, 2003.

- [23] M. Bawendi, M. Steigerwald, and L. Brus, "The quantum mechanics of larger semiconductor clusters (" quantum dots")," *Annual Review of Physical Chemistry*, vol. 41, no. 1, pp. 477–496, 1990.
- [24] A. Efros and M. Rosen, "The electronic structure of semiconductor nanocrystals," *Annual Review of Materials Science*, vol. 30, no. 1, pp. 475–521, 2000.
- [25] L. Brus, "Electronic wave functions in semiconductor clusters: experiment and theory," *Journal of Physical Chemistry*, vol. 90, no. 12, pp. 2555–2560, 1986.
- [26] L. Brus, "A simple model for the ionization potential, electron affinity, and aqueous redox potentials of small semiconductor crystallites," *The Journal of Chemical Physics*, vol. 79, p. 5566, 1983.
- [27] L. Brus, "Electron-electron and electron-hole interactions in small semiconductor crystallites: The size dependence of the lowest excited electronic state," *The Journal of Chemical Physics*, vol. 80, p. 4403, 1984.
- [28] F. Wise, "Lead salt quantum dots: the limit of strong quantum confinement," *Accounts of Chemical Research*, vol. 33, no. 11, pp. 773–780, 2000.
- [29] B. Wehrenberg, C. Wang, and P. Guyot-Sionnest, "Interband and intraband optical studies of pbse colloidal quantum dots," *Journal of Physical Chemistry B*, vol. 106, no. 41, pp. 10634–10640, 2002.
- [30] H. Du, C. Chen, R. Krishnan, T. Krauss, J. Harbold, F. Wise, M. Thomas, and J. Silcox, "Optical properties of colloidal pbse nanocrystals," *Nano Letters*, vol. 2, no. 11, pp. 1321–1324, 2002.

- [31] Z. Hens, D. Vanmaekelbergh, E. Kooij, H. Wormeester, G. Allan, and C. Delerue, "Effect of quantum confinement on the dielectric function of pbse," *Physical Review Letters*, vol. 92, no. 2, p. 22, 2004.
- [32] T. Krauss and L. Brus, "Charge, polarizability, and photoionization of single semiconductor nanocrystals," *Physical Review Letters*, vol. 83, no. 23, pp. 4840–4843, 1999.
- [33] C. Ben-Porat, O. Cherniavskaya, L. Brus, K. Cho, and C. Murray, "Electric fields on oxidized silicon surfaces: Static polarization of PbSe nanocrystals," *Journal of Physical Chemistry A*, vol. 108, no. 39, pp. 7814–7819, 2004.
- [34] C. Collier, T. Vossmeyer, and J. Heath, "Nanocrystal superlattices," *Annual Review of Physical Chemistry*, vol. 49, no. 1, pp. 371–404, 1998.
- [35] C. Murray, C. Kagan, and M. Bawendi, "Self-organization of cdse nanocrystallites into three-dimensional quantum dot superlattices," *Science*, vol. 270, no. 5240, p. 1335, 1995.
- [36] J. Urban, D. Talapin, E. Shevchenko, and C. Murray, "Self-assembly of pbte quantum dots into nanocrystal superlattices and glassy films," *J. Am. Chem. Soc*, vol. 128, no. 10, pp. 3248–3255, 2006.
- [37] G. Markovich, C. Collier, and J. Heath, "Reversible metal-insulator transition in ordered metal nanocrystal monolayers observed by impedance spectroscopy," *Physical Review Letters*, vol. 80, no. 17, pp. 3807–3810, 1998.
- [38] S. Henrichs, C. Collier, R. Saykally, Y. Shen, and J. Heath, "The dielectric function of silver nanoparticle langmuir monolayers compressed through

- the metal insulator transition,” *Journal of the American Chemical Society*, vol. 122, no. 17, pp. 4077–4083, 2000.
- [39] C. Collier, R. Saykally, J. Shiang, S. Henrichs, and J. Heath, “Reversible tuning of silver quantum dot monolayers through the metal-insulator transition,” *Science*, vol. 277, no. 5334, p. 1978, 1997.
- [40] C. Whan, J. White, and T. Orlando, “Full capacitance matrix of coupled quantum dot arrays: Static and dynamical effects,” *Applied Physics Letters*, vol. 68, p. 2996, 1996.
- [41] I. Gur, N. Fromer, M. Geier, and A. Alivisatos, “Air-stable all-inorganic nanocrystal solar cells processed from solution,” *Science*, vol. 310, no. 5747, pp. 462–465, 2005.
- [42] R. Schaller and V. Klimov, “High efficiency carrier multiplication in pbse nanocrystals: Implications for solar energy conversion,” *Physical Review Letters*, vol. 92, no. 18, pp. 186601–186601, 2004.
- [43] I. Robel, V. Subramanian, M. Kuno, and P. Kamat, “Quantum dot solar cells. harvesting light energy with cdse nanocrystals molecularly linked to mesoscopic tio₂ films,” *Journal of the American Chemical Society*, vol. 128, no. 7, pp. 2385–2393, 2006.
- [44] S. Gaponenko, *Optical Properties of Semiconductor Nanocrystals (Handbook)*. New York: Wiley, 1998.
- [45] M. Troparevsky, L. Kronik, and J. Chelikowsky, “Optical properties of cdse quantum dots,” *The Journal of Chemical Physics*, vol. 119, p. 2284, 2003.

- [46] U. Banin and O. Millo, "Tunneling and optical spectroscopy of semiconductor nanocrystals," *Annual Review of Physical Chemistry*, vol. 54, no. 1, pp. 465–492, 2003.
- [47] P. Liljeroth, P. van Emmichoven, S. Hickey, H. Weller, B. Grandidier, G. Allan, and D. Vanmaekelbergh, "Density of states measured by scanning-tunneling spectroscopy sheds new light on the optical transitions in pbse nanocrystals," *Physical Review Letters*, vol. 95, no. 8, p. 86801, 2005.
- [48] B. Alperson, I. Rubinstein, G. Hodes, D. Porath, and O. Millo, "Energy level tunneling spectroscopy and single electron charging in individual cdse quantum dots," *Applied Physics Letters*, vol. 75, p. 1751, 1999.
- [49] N. Y. Morgan, C. A. Leatherdale, M. Drndic, M. V. Jarosz, M. A. Kastner, and M. Bawendi, "Electronic transport in films of colloidal cdse nanocrystals," *Physical Review B*, vol. 66, no. 7, p. 9, 2002.
- [50] M. Drndic, M. Jarosz, N. Morgan, M. Kastner, and M. Bawendi, "Transport properties of annealed cdse colloidal nanocrystal solids," *Journal of Applied Physics*, vol. 92, p. 7498, 2002.
- [51] B. Wehrenberg and P. Guyot-Sionnest, "Electron and hole injection in pbse quantum dot films," *Journal of the American Chemical Society*, vol. 125, no. 26, pp. 7806–7807, 2003.
- [52] B. Wehrenberg, D. Yu, J. Ma, and P. Guyot-Sionnest, "Conduction in charged pbse nanocrystal films," *Journal of Physical Chemistry B*, vol. 109, no. 43, pp. 20192–20199, 2005.

- [53] D. Yu, B. Wehrenberg, P. Jha, J. Ma, and P. Guyot-Sionnest, "Electronic transport of n-type cdse quantum dot films: Effect of film treatment," *Journal of Applied Physics*, vol. 99, p. 104315, 2006.
- [54] D. Yu, C. Wang, B. Wehrenberg, P. Guyot-Sionnest, and E. Taking, "Variable range hopping conduction in semiconductor nanocrystal solids," *J. Phys. Chem. B Phys Rev Lett*, vol. 92, p. 216802, 2003.
- [55] D. Yu, C. Wang, and P. Guyot-Sionnest, "n-type conducting cdse nanocrystal solids," *Science*, vol. 300, no. 5623, pp. 1277–1280, 2003.
- [56] C. Black, C. Murray, R. Sandstrom, and S. Sun, "Spin-dependent tunneling in self-assembled cobalt-nanocrystal superlattices," *Science*, vol. 290, no. 5494, pp. 1131–1134, 2000.
- [57] T. S. Mentzel, V. J. Porter, S. Geyer, K. MacLean, M. G. Bawendi, and M. A. Kastner, "Charge transport in pbse nanocrystal arrays," *Physical Review B*, vol. 77, no. 7, p. 8, 2008.
- [58] K. Beverly, J. Sampaio, and J. Heath, "Effects of size dispersion disorder on the charge transport in self-assembled 2-d ag nanoparticle arrays," *Journal of Physical Chemistry B-Condensed Phase*, vol. 106, no. 9, pp. 2131–2135, 2002.
- [59] C. Leatherdale, C. Kagan, N. Morgan, S. Empedocles, M. Kastner, and M. Bawendi, "Photoconductivity in cdse quantum dot solids," *Physical Review B*, vol. 62, no. 4, pp. 2669–2680, 2000.
- [60] D. Talapin and C. Murray, "Pbse nanocrystal solids for n-and p-channel thin film field-effect transistors," *Science*, vol. 310, no. 5745, pp. 86–89, 2005.

- [61] M. V. Jarosz, V. J. Porter, B. R. Fisher, M. A. Kastner, and M. G. Bawendi, "Photoconductivity studies of treated cdse quantum dot films exhibiting increased exciton ionization efficiency," *Physical Review B*, vol. 70, no. 19, p. 12, 2004.
- [62] V. J. Porter, T. Mentzel, S. Charpentier, M. A. Kastner, and M. G. Bawendi, "Temperature-, gate-, and photoinduced conductance of close-packed cdte nanocrystal films," *Physical Review B*, vol. 73, no. 15, p. 9, 2006.
- [63] V. J. Porter, S. Geyer, J. E. Halpert, M. A. Kastner, and M. G. Bawendi, "Photoconduction in annealed and chemically treated cdse/zns inorganic nanocrystal films," *Journal of Physical Chemistry C*, vol. 112, no. 7, pp. 2308–2316, 2008.
- [64] A. Middleton and N. Wingreen, "Collective transport in arrays of small metallic dots," *Physical Review Letters*, vol. 71, no. 19, pp. 3198–3201, 1993.
- [65] R. Parthasarathy, X. M. Lin, and H. M. Jaeger, "Electronic transport in metal nanocrystal arrays: The effect of structural disorder on scaling behavior," *Physical Review Letters*, vol. 87, no. 18, p. 4, 2001.
- [66] A. Rimberg, T. Ho, and J. Clarke, "Scaling behavior in the current-voltage characteristic of one-and two-dimensional arrays of small metallic islands," *Physical Review Letters*, vol. 74, no. 23, pp. 4714–4717, 1995.
- [67] C. Lebreton, C. Vieu, A. Ppin, M. Mejias, F. Carcenac, Y. Jin, and H. Launois, "Coulomb blockade effect through a 2 d ordered array of pd islands obtained by colloidal deposition," *Microelectronic engineering*, vol. 41, pp. 507–510, 1998.

- [68] R. Parthasarathy, X. Lin, K. Elteto, T. Rosenbaum, and H. Jaeger, "Percolating through networks of random thresholds: finite temperature electron tunneling in metal nanocrystal arrays," *Physical Review Letters*, vol. 92, no. 7, p. 62, 2004.
- [69] M. Brust, D. Schiffrin, D. Bethell, and C. Kiely, "Novel gold-dithiol nano-networks with non-metallic electronic properties," *Advanced Materials*, vol. 7, no. 9, 1995.
- [70] R. Andres, J. Bielefeld, J. Henderson, D. Janes, V. Kolagunta, C. Kubiak, W. Mahoney, and R. Osifchin, "Self-assembly of a two-dimensional superlattice of molecularly linked metal clusters," *Science*, vol. 273, no. 5282, p. 1690, 1996.
- [71] C. Neugebauer and M. Webb, "Electrical conduction mechanism in ultrathin, evaporated metal films," *Journal of Applied Physics*, vol. 33, p. 74, 1962.
- [72] N. Mott and E. Davis, "Electronic processes in non-crystalline materials," 1979.
- [73] F. Remacle, K. Beverly, J. Heath, and R. Levine, "Conductivity of 2-d ag quantum dot arrays: Computational study of the role of size and packing disorder at low temperatures," *Journal of Physical Chemistry B-Condensed Phase*, vol. 106, no. 16, pp. 4116–4126, 2002.
- [74] A. Persano, G. Leo, L. Manna, and A. Cola, "Charge carrier transport in thin films of colloidal cdse quantum rods," *Journal of Applied Physics*, vol. 104, p. 074306, 2008.

- [75] A. Goodman and A. Rose, "Double extraction of uniformly generated electron-hole pairs from insulators with noninjecting contacts," *Journal of Applied Physics*, vol. 42, p. 2823, 1971.
- [76] K. Elteto, X. Lin, and H. Jaeger, "Electronic transport in quasi-one-dimensional arrays of gold nanocrystals," *Physical Review B*, vol. 71, p. 205412, 2005.
- [77] D. Klein, R. Roth, A. Lim, A. Alivisatos, and P. McEuen, "A single-electron transistor made from a cadmium selenide nanocrystal," *Nature*, vol. 389, no. 6652, pp. 699–700, 1997.
- [78] R. Sordan, K. Balasubramanian, M. Burghard, and K. Kern, "Coulomb blockade phenomena in electromigration break junctions," *Applied Physics Letters*, vol. 87, p. 013106, 2005.
- [79] A. A. Houck, J. Labaziewicz, E. K. Chan, J. A. Folk, and I. L. Chuang, "Kondo effect in electromigrated gold break junctions," *Nano Letters*, vol. 5, no. 9, pp. 1685–1688, 2005.
- [80] T. Ma, "Making silicon nitride film a viable gate dielectric," *IEEE Transactions on Electron Devices*, vol. 45, no. 3, pp. 680–690, 1998.
- [81] A. Grant, Q. Hu, and B. Kasemo, "Transmission electron microscopy "windows" for nanofabricated structures," *Nanotechnology*, vol. 15, no. 9, pp. 1175–1181, 2004.
- [82] E. Shevchenko, M. Ringler, A. Schwemer, D. Talapin, T. Klar, A. Rogach, J. Feldmann, and A. Alivisatos, "Self-assembled binary superlattices of cdse

- and au nanocrystals and their fluorescence properties," *J. Am. Chem. Soc.*, vol. 130, no. 11, pp. 3274–3275, 2008.
- [83] R. Krishnan, M. Hahn, Z. Yu, J. Silcox, P. Fauchet, and T. Krauss, "Polarization surface-charge density of single semiconductor quantum rods," *Physical Review Letters*, vol. 92, no. 21, p. 216803, 2004.
- [84] D. Ginger and N. Greenham, "Charge injection and transport in films of cdse nanocrystals," *Journal of Applied Physics*, vol. 87, p. 1361, 2000.
- [85] W. Woo, K. Shimizu, M. Jarosz, R. Neuhauser, C. Leatherdale, M. Rubner, and M. Bawendi, "Reversible charging of cdse nanocrystals in a simple solid-state device," *Advanced Materials*, vol. 14, no. 15, p. 1068, 2002.
- [86] D. Novikov, M. Drndic, L. Levitov, M. Kastner, M. Jarosz, and M. Bawendi, "Lévy statistics and anomalous transport in quantum-dot arrays," *Physical review B*, vol. 72, no. 7, pp. 75309–75309, 2005.
- [87] D. Klein, P. McEuen, J. Katari, R. Roth, and A. Alivisatos, "An approach to electrical studies of single nanocrystals," *Applied Physics Letters*, vol. 68, p. 2574, 1996.
- [88] H. Park, A. Lim, A. Alivisatos, J. Park, and P. McEuen, "Fabrication of metallic electrodes with nanometer separation by electromigration," *Applied Physics Letters*, vol. 75, p. 301, 1999.
- [89] Y. V. Kervennic, H. S. J. V. d. Zant, A. F. Morpurgo, L. Gurevich, and L. P. Kouwenhoven, "Nanometer-spaced electrodes with calibrated separation," *Applied Physics Letters*, vol. 80, no. 2, pp. 321–323, 2002.

- [90] D. Strachan, D. Smith, D. Johnston, T. Park, M. Therien, D. Bonnell, and A. Johnson, "Controlled fabrication of nanogaps in ambient environment for molecular electronics," *Applied Physics Letters*, vol. 86, p. 043109, 2005.
- [91] J. Chen, M. Reed, A. Rawlett, and J. Tour, "Large on-off ratios and negative differential resistance in a molecular electronic device," *Science*, vol. 286, no. 5444, p. 1550, 1999.
- [92] J. Park, A. Pasupathy, J. Goldsmith, C. Chang, Y. Yaish, J. Petta, M. Rinkoski, J. Sethna, H. Abrua, and P. McEuen, "Coulomb blockade and the kondo effect in single-atom transistors," *Nature*, vol. 417, no. 6890, pp. 722–725, 2002.
- [93] A. Storm, J. Van Noort, S. De Vries, and C. Dekker, "Insulating behavior for dna molecules between nanoelectrodes at the 100 nm length scale," *Applied Physics Letters*, vol. 79, p. 3881, 2001.
- [94] A. Broers, "Resolution limits for electron-beam lithography," *IBM Journal of Research and Development*, vol. 32, no. 4, pp. 502–513, 1988.
- [95] T. Sedgwick, A. Broers, and B. Agule, "A novel method for fabrication of ultrafine metal lines by electron beams," *Journal of The Electrochemical Society*, vol. 119, p. 1769, 1972.
- [96] C. Umbach, S. Washburn, R. Laibowitz, and R. Webb, "Magnetoresistance of small, quasi-one-dimensional, normal-metal rings and lines," *Physical Review B*, vol. 30, p. 4048, 1981.
- [97] D. Strachan, D. Smith, M. Fischbein, D. Johnston, B. Guiton, M. Drndic, D. Bonnell, and A. Johnson Jr, "Clean electromigrated nanogaps imaged by

- transmission electron microscopy," *Nano Letters*, vol. 6, no. 3, pp. 441–444, 2006.
- [98] H. Zandbergen, R. van Duuren, P. Alkemade, G. Lientschnig, O. Vasquez, C. Dekker, and F. Tichelaar, "Sculpting nanoelectrodes with a transmission electron beam for electrical and geometrical characterization of nanoparticles," *Nano Letters*, vol. 5, no. 3, pp. 549–554, 2005.
- [99] T. Chang, "Proximity effect in electron-beam lithography," *Journal of Vacuum Science and Technology*, vol. 12, p. 1271, 1975.
- [100] M. Parikh and D. Kyser, "Energy deposition functions in electron resist films on substrates," *Journal of Applied Physics*, vol. 50, p. 1104, 1979.
- [101] W. Scott, "The theory of small-angle multiple scattering of fast charged particles," *Reviews of Modern Physics*, vol. 35, no. 2, pp. 231–313, 1963.
- [102] W. Werner, W. Smekal, H. Stri, and C. Eisenmenger-Sittner, "Angular dependence of the surface excitation probability for medium energy electrons backscattered from al and si surfaces," *Journal of Vacuum Science and Technology A*, vol. 19, p. 2388, 2001.
- [103] B. A. Gurney, V. S. Speriosu, J. P. Nozieres, H. Lefakis, D. R. Wilhoit, and O. U. Need, "Direct measurement of spin-dependent conduction-electron mean free paths in ferromagnetic metals," *Physical Review Letters*, vol. 71, no. 24, pp. 4023–4026, 1993.
- [104] A. Bezryadin, C. N. Lau, and M. Tinkham, "Quantum suppression of superconductivity in ultrathin nanowires," *Nature*, vol. 404, no. 6781, pp. 971–974, 2000.

- [105] C. N. Lau, N. Markovic, M. Bockrath, A. Bezryadin, and M. Tinkham, "Quantum phase slips in superconducting nanowires," *Physical Review Letters*, vol. 87, no. 21, p. 4, 2001.
- [106] M. Zgirski, K. P. Riikonen, V. Touboltsev, and K. Arutyunov, "Size dependent breakdown of superconductivity in ultranarrow nanowires," *Nano Letters*, vol. 5, no. 6, pp. 1029–1033, 2005.
- [107] C. Beenakker and H. Houten, "Josephson current through a superconducting quantum point contact shorter than the coherence length," *Physical Review Letters*, vol. 66, pp. 3056–3059, 1991.
- [108] N. Tas, J. Haneveld, H. Jansen, M. Elwenspoek, and A. Van den Berg, "Capillary filling speed of water in nanochannels," *Applied Physics Letters*, vol. 85, p. 3274, 2004.
- [109] H. Tan, I. Piletic, R. Riter, N. Levinger, and M. Fayer, "Dynamics of water confined on a nanometer length scale in reverse micelles: Ultrafast infrared vibrational echo spectroscopy," *Physical Review Letters*, vol. 94, p. 057405, 2004.
- [110] R. Austin, J. Tegenfeldt, H. Cao, S. Chou, and E. Cox, "Scanning the controls: Genomics and nanotechnology," *IEEE Transactions on Nanotechnology*, vol. 1, no. 1, pp. 12–18, 2002.
- [111] D. Strachan, D. Johnston, B. Guiton, S. Datta, P. Davies, D. Bonnell, and A. Johnson, "Real-Time TEM Imaging of the Formation of Crystalline Nanoscale Gaps," *Physical Review Letters*, vol. 100, no. 5, pp. 56805–56805, 2008.

- [112] D. Natelson, R. Willett, K. West, and L. Pfeiffer, "Molecular-scale metal wires," *Solid State Communications*, vol. 115, no. 5, pp. 269–274, 2000.
- [113] A. Storm, J. Chen, X. Ling, H. Zandbergen, and C. Dekker, "Fabrication of solid-state nanopores with single-nanometre precision," *Nature Materials*, vol. 2, no. 8, pp. 537–540, 2003.
- [114] J. Heng, C. Ho, T. Kim, R. Timp, A. Aksimentiev, Y. Grinkova, S. Sligar, K. Schulten, and G. Timp, "Sizing dna using a nanometer-diameter pore," *Biophysical journal*, vol. 87, no. 4, pp. 2905–2911, 2004.
- [115] M. Y. Wu, R. M. M. Smeets, M. Zandbergen, U. Ziese, D. Krapf, P. E. Batson, N. H. Dekker, C. Dekker, and H. W. Zandbergen, "Control of shape and material composition of solid-state nanopores," *Nano Letters*, vol. 9, no. 1, pp. 479–484, 2009.
- [116] M. Y. Wu, D. Krapf, M. Zandbergen, H. Zandbergen, and P. E. Batson, "Formation of nanopores in a sin/sio₂ membrane with an electron beam," *Applied Physics Letters*, vol. 87, no. 11, 2005.
- [117] Y. Li, A. Rizzo, M. Mazzeo, L. Carbone, L. Manna, R. Cingolani, and G. Gigli, "White organic light-emitting devices with cdse/zns quantum dots as a red emitter," *Journal of Applied Physics*, vol. 97, p. 113501, 2005.
- [118] S. Bezrukov, I. Vodyanoy, and V. Parsegian, "Counting polymers moving through a single ion channel," *Nature*, vol. 370, no. 6487, pp. 279–281, 1994.
- [119] A. Meller, L. Nivon, and D. Branton, "Voltage-driven DNA translocations through a nanopore," *Physical Review Letters*, vol. 86, p. 3435, 2001.

- [120] J. Kasianowicz, E. Brandin, D. Branton, and D. Deamer, “Characterization of individual polynucleotide molecules using a membrane channel,” *Proceedings of the National Academy of Sciences*, vol. 93, no. 24, pp. 13770–13773, 1996.
- [121] W. Vercoutere, S. Winters-Hilt, H. Olsen, D. Deamer, D. Haussler, and M. Akeson, “Rapid discrimination among individual DNA hairpin molecules at single-nucleotide resolution using an ion channel,” *Nature Biotechnology*, vol. 19, pp. 248–252, 2001.
- [122] A. Storm, C. Storm, J. Chen, H. Zandbergen, J. Joanny, and C. Dekker, “Fast DNA translocation through a solid-state nanopore,” *Arxiv preprint q-bio/0404041*, 2004.
- [123] G. King and J. Golovchenko, “Probing nanotube-nanopore interactions,” *Physical Review Letters*, vol. 95, no. 21, p. 216103, 2005.
- [124] J. Lagerqvist, M. Zwolak, and M. Di Ventra, “Fast DNA sequencing via transverse electronic transport,” *Nano letters*, vol. 6, no. 4, p. 779, 2006.
- [125] Y. Zhang, J. Small, W. Pontius, and P. Kim, “Fabrication and electric-field-dependent transport measurements of mesoscopic graphite devices,” *Applied Physics Letters*, vol. 86, p. 073104, 2005.
- [126] K. Novoselov, D. Jiang, F. Schedin, T. Booth, V. Khotkevich, S. Morozov, and A. Geim, “Two-dimensional atomic crystals,” *Proceedings of the National Academy of Sciences*, vol. 102, no. 30, pp. 10451–10453, 2005.
- [127] A. Geim and K. Novoselov, “The rise of graphene,” *Nature Materials*, vol. 6, no. 3, pp. 183–191, 2007.

- [128] A. Neto, F. Guinea, N. Peres, K. Novoselov, and A. Geim, "The electronic properties of graphene," *Arxiv preprint arXiv:0709.1163*, 2007.
- [129] R. Nair, P. Blake, A. Grigorenko, K. Novoselov, T. Booth, T. Stauber, N. Peres, and A. Geim, "Fine structure constant defines visual transparency of graphene," *Science*, vol. 320, no. 5881, p. 1308, 2008.
- [130] N. Tombros, C. Jozsa, M. Popinciuc, H. Jonkman, and B. van Wees, "Electronic spin transport and spin precession in single graphene layers at room temperature," *Nature*, vol. 448, no. 7153, pp. 571–574, 2007.
- [131] K. Novoselov, Z. Jiang, Y. Zhang, S. Morozov, H. Stormer, U. Zeitler, J. Maan, G. Boebinger, P. Kim, and A. Geim, "Room-temperature quantum Hall effect in graphene," *Science*, vol. 315, no. 5817, p. 1379, 2007.
- [132] K. Bolotin, K. Sikes, Z. Jiang, M. Klima, G. Fudenberg, J. Hone, P. Kim, and H. Stormer, "Ultrahigh electron mobility in suspended graphene," *Solid State Communications*, vol. 146, no. 9-10, pp. 351–355, 2008.
- [133] J. Lee, J. Lee, T. Tanaka, and H. Mori, "In situ hrem observation of crystalline-to-gas transition in nanometer-sized ag particles," *Physical Review Letters*, vol. 96, p. 075504, 2001.
- [134] T. J. Booth, P. Blake, R. R. Nair, D. Jiang, E. W. Hill, U. Bangert, A. Bleloch, M. Gass, K. S. Novoselov, M. I. Katsnelson, and A. K. Geim, "Macroscopic graphene membranes and their extraordinary stiffness," *Nano Letters*, vol. 8, no. 8, pp. 2442–2446, 2008.
- [135] J. Meyer, A. Geim, M. Katsnelson, K. Novoselov, T. Booth, and S. Roth, "The structure of suspended graphene sheets," *Nature*, vol. 446, pp. 60–63, 2007.

- [136] J. C. Meyer, C. Kisielowski, R. Erni, M. D. Rossell, M. F. Crommie, and A. Zettl, “Direct imaging of lattice atoms and topological defects in graphene membranes,” *Nano Letters*, vol. 8, no. 11, pp. 3582–3586, 2008.
- [137] J. Meyer, C. Girit, M. Crommie, and A. Zettl, “Imaging and dynamics of light atoms and molecules on graphene,” *Nature*, vol. 454, no. 7202, pp. 319–322, 2008.
- [138] J. Meyer, C. Girit, M. Crommie, and A. Zettl, “Hydrocarbon lithography on graphene membranes,” *Applied Physics Letters*, vol. 92, p. 123110, 2008.
- [139] C. Berger, Z. Song, X. Li, X. Wu, N. Brown, C. Naud, D. Mayou, T. Li, J. Hass, A. Marchenkov, *et al.*, “Electronic confinement and coherence in patterned epitaxial graphene,” *Science*, vol. 312, no. 5777, pp. 1191–1196, 2006.
- [140] J. Bunch, Y. Yaish, M. Brink, K. Bolotin, and P. McEuen, “Coulomb oscillations and Hall effect in quasi-2D graphite quantum dots,” *Nano Letters*, vol. 5, no. 2, pp. 287–290, 2005.
- [141] L. Ponomarenko, F. Schedin, M. Katsnelson, R. Yang, E. Hill, K. Novoselov, and A. Geim, “Chaotic Dirac billiard in graphene quantum dots,” *Science*, vol. 320, no. 5874, p. 356, 2008.
- [142] M. Han, B. Ozyilmaz, Y. Zhang, and P. Kim, “Energy band gap engineering of graphene nanoribbons,” *Physical Review Letters*, vol. 98, p. 206805, 2006.
- [143] C. Stampfer, E. Schurtenberger, F. Molitor, J. Guttinger, T. Ihn, and K. Ensslin, “Tunable graphene single electron transistor,” *Nano Letters*, vol. 8, no. 8, p. 2379, 2008.

- [144] Z. Chen, Y. Lin, M. Rooks, and P. Avouris, "Graphene nano-ribbon electronics," *Physica E*, vol. 40, no. 2, pp. 228–232, 2007.
- [145] X. Li, X. Wang, L. Zhang, S. Lee, and H. Dai, "Chemically derived, ultra-smooth graphene nanoribbon semiconductors," *Science*, vol. 319, no. 5867, p. 1229, 2008.
- [146] S. Datta, D. Strachan, S. Khamis, and A. Johnson, "Crystallographic Etching of Few-Layer Graphene," *Nano Letters*, vol. 8, no. 1912, p. 1915, 2008.
- [147] L. Tapasztó, G. Dobrik, P. Lambin, and L. Biró, "Tailoring the atomic structure of graphene nanoribbons by scanning tunnelling microscope lithography," *Nature Nanotechnology*, vol. 3, no. 7, pp. 397–401, 2008.
- [148] K. Healy, B. Schiedt, and A. Morrison, "Solid-state nanopore technologies for nanopore-based DNA analysis," *Nanomedicine*, vol. 2, no. 6, pp. 875–897, 2007.
- [149] J. Bunch, S. Verbridge, J. Alden, A. van der Zande, J. Parpia, H. Craighead, and P. McEuen, "Impermeable atomic membranes from graphene sheets," *Nano Letters*, vol. 8, no. 8, pp. 2458–2462, 2008.
- [150] J. Hiraki, H. Mori, E. Taguchi, H. Yasuda, H. Kinoshita, and N. Ohmae, "Transformation of diamond nanoparticles into onion-like carbon by electron irradiation studied directly inside an ultrahigh-vacuum transmission electron microscope," *Applied Physics Letters*, vol. 86, no. 22, 2005.
- [151] A. Krasheninnikov and F. Banhart, "Engineering of nanostructured carbon materials with electron or ion beams," *Nature Materials*, vol. 6, no. 10, pp. 723–734, 2007.